Laser spectroscopy of nobelium isotopes

Laserspektroskopie an Nobelium-Isotopen
Vom Fachbereich Physik der Technischen Universität Darmstadt zur Erlangung des Grades eines Doktors der Naturwissenschaften (Dr. rer. nat.)
genehmigte Dissertation von Premaditya Chhetri aus Kalimpong
Tag der Einreichung: 25.06.2018, Tag der Prüfung: 16.07.2018
Darmstadt 2018

1. Gutachter: Prof. Dr. Thomas Walther
2. Gutachter: Prof. Dr. Michael Block

TECHNISCHE UNIVERSITÄT DARMSTADT

Fachbereich Physik
Institut für Angewandte Physik
Laser und Quantenoptik

Laser spectroscopy of nobelium isotopes
Laserspektroskopie an Nobelium-Isotopen

genehmigte Dissertation von Premaditya Chhetri aus Kalimpong

1. Gutachter: Prof. Dr. Thomas Walther
2. Gutachter: Prof. Dr. Michael Block

Tag der Einreichung: 25.06.2018
Tag der Prüfung: 16.07.2018

Darmstadt 2018

Institut für Angewandte Physik
Technische Universität Darmstadt

Laser spectroscopy of nobelium isotopes

Vom Fachbereich Physik
der Technischen Universität Darmstadt

zur Erlangung des Grades
eines Doktors der Naturwissenschaften (Dr. rer. nat.)

genehmigte Dissertation von
M.Sc. Premaditya Chhetri
aus Kalimpong

Darmstadt 2018

Abstract

Laser spectroscopy is a versatile tool to unveil fundamental atomic properties of an element and the ground state information of the atomic nucleus. The heaviest elements are of particular interest as the ordering of their shell electrons is strongly influenced by electron-electron correlations, quantum electrodynamics and relativistic effects leading to distinct chemical behaviour. The elements beyond fermium ($Z > 100$) are accessible in fusion evaporation reactions at minute quantities and at high energies, hampering their optical spectroscopy. Recently, the RAdiation Detected Resonance Ionization Spectroscopy (RADRIS) technique was employed to explore the electronic structure of the element nobelium (No, $Z = 102$). The $^1S_0 \rightarrow ^1P_1$ ground state transition of this element was identified.

In this work, the pioneering experiment on laser spectroscopy of nobelium was extended to the isotopes of nobelium ($^{252-254}$No). These were produced in fusion-evaporation reactions by bombarding lead targets ($^{206-208}$Pb) with ^{48}Ca projectiles. After separation from the primary beam by the velocity filter SHIP (Separator for Heavy Ion reaction Products), at GSI, the fusion products were stopped in 95 mbar high-purity argon gas and collected onto a thin tantalum filament. After a sufficient collection time, which depended on the half-life ($T_{1/2}$) of the isotope under consideration, the primary beam was blocked in order to have a background free signal. During the beam-off period, the collected nobelium ions were re-evaporated as neutral atoms from the filament and were probed by two laser beams for ionization. The created photo-ions were detected by their characteristic alpha decay. With this technique the isotope shift of the transition was measured for the isotopes $^{252-254}$No. A hyperfine splitting of the $^1P_1$ level was resolved in ^{253}No. These measurements in combination with state-of-the-art atomic calculations provided a deep insight into the evolution of nuclear deformation of the investigated nobelium isotopes in the vicinity of the deformed shell closure at neutron number $N = 152$ along with an assesment of the magnetic moment, μ, and the spectroscopic quadrupole moment, Q_s, for ^{253}No.

Moreover, several high-lying Rydberg states were measured for the first time in ^{254}No. These Rydberg states, populated in different ways enabled establishing different Rydberg series and the extraction of the first ionization potential of the element plus an additional low-lying atomic state in ^{254}No that is optically inaccessible from the ground state.

Zusammenfassung

Laserspektrosopie ist ein universelles Werzeug für die Bestimmung fundamentaler Eigenschaften der Elektronenstruktur in der Atomhülle aber auch von Eigenschaften des Atomkerns speziell die Laserspektroskopie an den schwersten Elementen ist durch ihre hohe Kernladungszahl von großem Interesse und zusätzlich durch die geringe Verfügbarkeit extrem herausfordernd. Da die Elektronenhülle stark durch Elektron-Elektron-Korrelationen sowie QED- und relativistische Effekte beeinflusst wird, beeinflusst die hohe Ladung und die Vielzahl der Elektronen in den schweren Elementen die Elektronenkonfigurationen und somit auch ihre chemischen Eigenschaften. Die Erzeugung von Elementen schwerer als Fermium ($Z > 100$) ist lediglich in geringsten Mengen durch Schwerionen-Fusions-Reaktionen möglich und stellt daher eine große Herausforderung für laserspektroskopische Verfahren dar. Erst kürzlich wurde die *RADRIS* (von engl. *RAdiation Detected Resonance Ionization Spectroscopy*) Methode erfolgreich verwendet, um die Elektronenstruktur des Elements Nobelium (No, $Z = 102$) zu untersuchen, bei der unter anderem der $^1S_0 \rightarrow {}^1P_1$ Grundzustandsübergang identifiziert werden konnte.

Im Rahmen dieser Arbeit wurde diese Technik auf weitere Nobelium-Isotope ausgeweitet, die über die Fusions Reaktion eines ^{48}Ca-Strahls mit einer Bleifolie ($^{206-208}$Pb) an der GSI Darmstadt erzeugt wurden. Nach ihrer Separation vom Primärstrahl durch das Geschwindigkeitsfilter SHIP (Separator for Heavy Ion reaction Products) werden die Ionen in 95 mbar hochreinem Argongas gestoppt und auf einem Tantal-Filament gesammelt und dadurch neutralisiert. Nach einer geeigneten Akkumulationszeit, die der Halbwertszeit des jeweiligen Isotops angepasst ist, wird der Primärstrahl geblockt, um hintergrundfreie Messungen zu ermöglichen. Während dieser Zeit werden die neutralisierten Nobelium-Atome über ein Aufheizen des Filaments abgedampft, anschließend durch zwei Laserpulse ionisiert und über ihren charakteristischen Alpha-Zerfall nachgewiesen. Mit dieser Methode wurd ein Grundzustandsübergang in den Isotopen $^{252-254}$No detailiert vermessen und die Hyperfeinstruktur von ^{253}No bestimmt. Die experimentellen Befunde in Kombination mit modernsten atomaren Berechnungen ermöglichen den Zugang zu Kerneigenschaften und geben somit Aufschluss über die Entwicklung der Deformation der Nobelium-Isotope in der Region des deformierten Schalenabschlusses bei $N = 152$, dem magnetischen Moment μ und dem spektroskopischen Quadrupolmoment Q_s von ^{253}No.

Zusätzlich konnten verschiedene hochliegende Rydberg-Zustände in ^{254}No vermessen werden, die von zwei verschiedenen angeregten Zuständen angeregt werden. Über die Konvergenz dieser Zustände konnte das Ionisationspotantial von ^{254}No bestimmt werden.

Acknowledgement

These five years of my PhD have really whizzed by at the GSI, through which I have a gained an enormous amount of experience. I have been lucky enough to participate in many different experiments and attend quite a few conferences, all of which I shall never forget.

I would firstly like to express my deepest gratitude towards my supervisors Prof. Dr. Thomas Walther and Prof. Dr. Michael Block for giving me the opportunity to pursue my PhD in their group. Thank you for the guidance and enormous amount of help and support you have given me throughout the whole of my PhD studies.

I am also grateful to Prof. Dr. Joachim Enders and Prof. Dr. Guy Moore for agreeing to be in my examination committee.

Special thanks to my colleagues of the super heavy element group at GSI: Dr. Mustapha Laatiaoui, Dr. Sebastian Raeder, Dr. Christian Droese, Dr. Francesca Giacoppo, Dr. Andrew Mistry, Dr. Fritz-Peter Heßberger, Dr. Felix Lautenschläger, Dr. Enrique Minaya-Ramirez, Oliver Kaleja and Lotte Lens for their incredible support during the last five years. I would also like to thank Prof. Dr. Hartmut and Dr. Werner Lauth for their support and helpful discussion. I also thank the entire RADRIS collaboration. Without them, this thesis would have reached this successful end.

I would also like to thank my friends "Frau" Dr. Tuğba Arıcı, Dr. Sivaji Purushothaman, Elif Şahin, Dr. Stephane Pietri and Daria Kostyleva for making these five years fun with all those gossips, drama and the insane amount of parties.

Lastly I would like to thank my parents, my sister and Tamanna Nembang Subba for their continued support and encouragement throughout my PhD.

Contents

List of Figures

List of Tables

1 Introduction

The determination of the atomic, nuclear and chemical properties of elements beyond fermium (Fm, $Z = 100$) is one of the most interesting and challenging fields of study [1, 2, 3, 4]. Such elements do not exist in nature and can be produced only in minute quantities, sometimes at the rate of one atom per week, via fusion evaporation reactions at accelerator facilities. The liquid drop model predicts these elements to instantaneously undergo spontaneous fission. The repulsive Coulomb force of the positively charged protons is high enough to overcome the attractive short range interaction of the strong nuclear force. However, the existence of heavier elements suggests enhanced stability not covered by this simple model.

Thus, the heaviest elements owe their existence to nuclear shell effects, which can be considered analogous to the electron shells. The proton and neutron shell formation counteracts the repulsive Coulomb interaction between the protons, thus preventing the immediate fissioning of the nuclei. This stabilization effect in very- and super-heavy nuclei allows probing the underlying forces in the nucleus at the extremes of nuclear existence. This general interest in this region of the nuclear chart has triggered investigations of the production of elements up to oganesson (Og, $Z = 118$) [5], decay and in-beam spectroscopy probing the underlying nuclear structure [6, 7], mass measurements determining the binding energy of the nuclear ground state [8, 9, 10, 11] and also investigations to study the atomic and chemical behaviour of the heaviest elements [1, 4].

To date, the most advanced method to study the atomic and chemical properties of these heaviest elements is the chemistry of individual atoms in the gas and liquid phase [12, 13]. Using these techniques, it has already been possible to deduce the chemistry of elements $105-108$, 112 and 114 [14, 15, 16, 17, 18, 19]. These experiments aimed at investigating relativistic effects that can lead to deviations from the periodicity in atomic shells in the heaviest of elements. These relativistic effects are caused by a contraction of the wave functions of the inner $s_{1/2}$ and $p_{1/2}$ shell electrons. This contraction indirectly influences the binding energy of the valence electrons and thus, the chemical properties via the screening of the nuclear Coulomb potential [1]. Figure 1.1 shows how the relativistic effects influence the atomic orbitals for heavy elements.

Theoretical models implemented to calculate the atomic properties of the heaviest elements routinely consider electron-electron correlations, relativistic and quantum electrodynamics (QED) effects. Currently, several state-of-the-art many-body methods such as

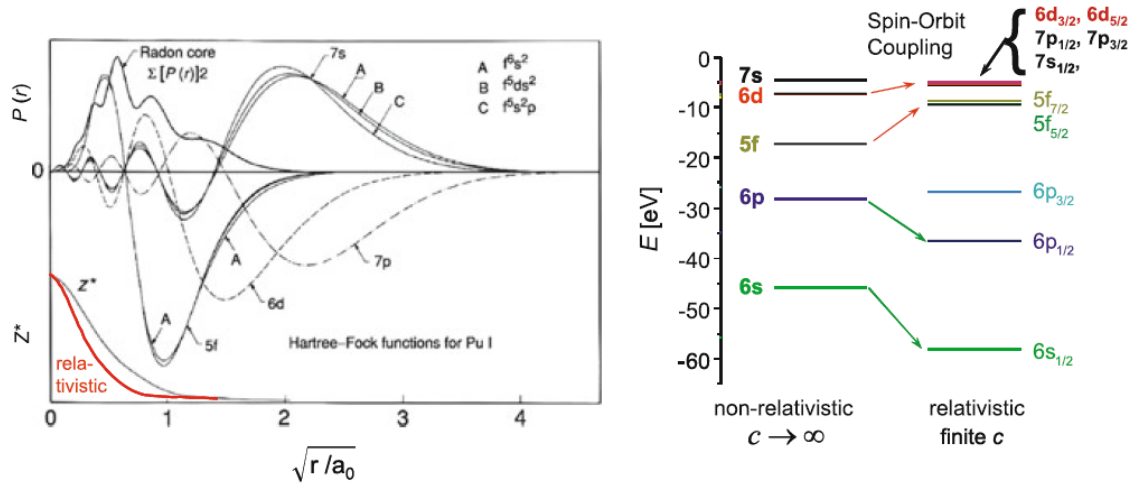

Figure 1.1: Left panel: Radial wave functions for plutonium. In the upper part, the radial probability distribution $P(r)$ of all electrons of the radon core is shown. Lower part, shows how the effective charge Z^* on the outer electron is influenced by relativistic effects. Right panel: Relativistic destabilization of the upper d and f orbitals and stabilization of the lower $s_{1/2}$ and $p_{1/2}$ orbitals for uranium. Adopted from [1].

multi-configuration Dirac-Fock (MCDF), relativistic coupled cluster (RCC), and configuration interaction (CI) are employed to study the atomic properties [20, 21]. However, these complex calculations have limited accuracy. A precise measurement of the atomic energy levels and the ionization potential (IP) by laser spectroscopic techniques may provide valuable benchmarks for the treatment of relativistic, QED and electron correlation effects and aid in the predictions from model calculations. However, the lack of experimental measurements of the atomic spectra for the heaviest elements make it impossible to independently validate these models.

Until recently, fermium was the heaviest element for which laser spectroscopic information was available. The spectroscopy experiments were performed using the IGRIS (Ion Guide Resonance Ionization Spectroscopy) technique, suitable for long-lived isotopes, and a total of seven atomic transitions have been observed. An upper limit of the IP of the element was also reported [22, 23]. In 2015, the $^1S_0 \rightarrow ^1P_1$ ground state transition in atomic nobelium was observed for the first time [24, 25] using the RAdiation Detected Resonance Ionization Spectroscopy (RADRIS) technique [26]. The observation of the $^1S_0 \rightarrow ^1P_1$ transition was a prerequisite for many other experiments that were performed within this work. Several Rydberg series comprising of 29 states were observed and this gave the possibility for the extraction of the IP along with another atomic level in nobelium, which was populated by buffer gas quenching of the $^1P_1$ state.

Laser spectroscopy additionally enabled the extraction of nuclear ground state properties via hyperfine structure (HFS) and isotope shift studies. The isotope ^{253}No features a nuclear spin of $I = 9/2$ which causes a splitting of the ^{1}P$_1$ state. From the splitting of the HFS, nuclear properties such as the magnetic dipole moment μ and spectroscopic quadrupole moment Q_s can be inferred, from which the single-particle $g-$factor and nuclear deformation can be determined. Information on nuclear deformation for even-mass nuclei can be extracted from the isotope shift (IS) measurements as the IS between two isotopes is related to the change in the mean square charge radii $\delta\langle r^2\rangle$.

This thesis is divided into 7 chapters. Firstly, the theoretical framework necessary to understand the results is elaborated in chapter 2. Chapter 3 explains the experimental set-ups in use (off-line and on-line). Additionally, the developed data acquisition system will be presented. Chapter 4 discusses the experimental identification of buffer gas quenching of the ^{1}P$_1$ state in nobelium along with off-line measurements on the chemical homologue ytterbium (Yb, $Z = 70$). These investigations on Yb lead to the development of a rate equation model to understand the experimental observations and enabled the extraction of the Einstein A coefficient of the ^{1}S$_0 \rightarrow ^1$P$_1$ transition in No. Chapter 5 details measurements of the Rydberg states in nobelium and the extraction of the IP and the identification of an additional low-lying atomic state in nobelium. The measured HFS of ^{253}No and the isotope shift of $^{252-254}$No is presented in chapter 6 along with a discussion on the impact of the inferred nuclear observables. In chapter 7, a summary of the results and an outlook for further spectroscopic investigations on heavy elements is given.

Key results of this work have been published in the following articles [24, 27, 28, 29, 30]

2 Theoretical background

This chapter presents the basics for understanding the experiment. In section 2.1 I will discuss the atomic physics aspects of this work and in section 2.2 some aspects related to nuclear physics.

2.1 Theoretical considerations for Atomic Physics

In this section a brief overview on basic atomic physics necessary for the understanding of the experiments is given. Starting from the most basic atomic system with one electron, which can be solved analytically, the approaches to address many-electron systems are discussed. Furthermore, the underlying principles of the interaction of light with single atom is detailed, which is important for the technique of resonant laser ionization used in this thesis. With respect to the extraction of nuclear parameters from the atomic spectra, the influence of the size of the nucleus and from nuclear spin on atomic excitation energy are introduced.

2.1.1 One electron system

The most simple atomic system consists of one electron and a nucleus with one proton, the hydrogen atom. The Hamilton operator for the hydrogen atom, which consists of a proton of mass m_p and charge $+e$ and an electron with mass m_e and charge $-e$, is given by [31]

$$\mathscr{H} = -\frac{\hbar^2}{2m_p}\Delta_p - \frac{\hbar^2}{2m_e}\Delta_e - \frac{e^2}{4\pi\varepsilon_0 r}. \tag{2.1}$$

Here the Laplace operators $\Delta_{p,e}$ act on to the position $r_{1,2}$ of the proton and electron, respectively. The motion can be reduced using the centre of mass formalism and a particle with a reduced mass $\mu = m_e + m_p/(m_e + m_p)$ at a position r relative to the centre of mass at $r_0 = 0$. In a quantum mechanical description, the electron wavefunctions for this system fulfil the Schrödinger equation given by

$$-\frac{\hbar^2}{2\mu}\Delta\psi - \frac{e^2}{4\pi\varepsilon_0 r}\psi = E\psi. \tag{2.2}$$

Due to the spherical symmetry of the Coulomb potential, this equation can be solved by using the separation ansatz in spherical coordinates. The wavefunction

$$\psi(r,\theta,\phi) = R(r)Y_l^m(\theta,\phi). \tag{2.3}$$

is separated in a radial function $R(r)$ and angular spherical harmonics $Y_l^m(\theta,\phi)$, l and m are the angular momentum and magnetic angular momentum quantum numbers, respectively. The energy eigenvalues, which correspond to the excitation energy of the atomic levels, can be determined by solving the Coulomb potential for the radial equation, which depends on r and the quantum number n [31]. The level energies E_n are given by

$$\begin{aligned} E_n &= -\mu \frac{e^4}{8\varepsilon_0^2 h^2} \frac{1}{n^2} \\ &= -\frac{R^*}{n^2} \end{aligned} \tag{2.4}$$

with the Rydberg constant

$$R^* = \frac{\mu e^4}{8\varepsilon_0^2 h^2}. \tag{2.5}$$

h is the Planck constant and n is the principal quantum number.

2.1.2 Multi-electron systems

One electron systems as described in the previous section can be solved analytically. In atomic systems with many electrons, the electron-electron correlations allow only for computational approaches involving the basic equations. This section will give a short introduction on the description of the calculation of level energies in multi-electron systems using different approximation methods.

Hartree-Fock method

A detailed description of a multi-electron system is achieved using the Hartree-Fock method, which is based on the central field approximation and allows calculation of the wave functions and orbital energies of a multi-electron system. In accordance with the independent par-

ticle approximation and the Pauli exclusion principle, the wave function for an $N-$electron system is given by a Slater determinant [32, 33],

$$\Psi(1,2,...,N) = \frac{1}{\sqrt{N!}} \begin{vmatrix} \psi_1(1) & \psi_1(2) & \dots & \psi_1(N) \\ \psi_2(1) & \psi_2(2) & \dots & \psi_2(N) \\ \vdots & \vdots & & \vdots \\ \psi_N(1) & \psi_N(2) & \dots & \psi_N(N) \end{vmatrix}. \tag{2.6}$$

where $\psi_1, ..., \psi_N$ are the one particle states. The total wave function of the system can be separated as $\psi_i(r) = \varphi_i(r)\zeta_i(\eta)$, where $\varphi_i(r)$ is the radial part and $\zeta_i(\eta)$ is the spin dependent part. The Hartree-Fock equation can be written as

$$\begin{aligned} -\frac{1}{2}\nabla^2\varphi_i(r) + V_{\text{ext}}\varphi_i(r) + \left(\sum_{j\neq i}^{N} \int \frac{\varphi_j^*(r')\varphi_j(r')}{|r-r'|} dr'\right)\varphi_i(r) \\ - \sum_{j\neq i}^{N} \left(\int \frac{\varphi_j^*(r')\varphi_i(r')}{|r-r'|} dr'\right)\varphi_j(r) = \varepsilon_i\varphi_i(r). \end{aligned} \tag{2.7}$$

The first term in the equation 2.7 describes the kinetic energy of the $i-$th electron and V_{ext} is the Coulomb potential of the nucleus. The third term is the correction to the Coulomb potential due to the centrally symmetric average of the electrostatic repulsion between the electrons. The forth term is the effective exchange potential due to Pauli principle which influences only electrons with parallel spins. The Hartree-Fock equation can be simplified by writing it as [34]

$$\begin{aligned} -\frac{\hbar^2}{2m}\frac{d^2u_{nl}}{dr^2} + \left(\frac{l(l+1)\hbar^2}{2mr^2} - \frac{e^2}{4\pi\varepsilon_0 r}[Z - Y_{nl}(r)] + \varepsilon_{nl,nl}\right)u_{nl} \\ = \frac{e^2}{4\pi\varepsilon_0 r}X_{nl}(r) + \sum_{n'} \varepsilon_{n'l,nl}u_{nl}. \end{aligned} \tag{2.8}$$

where Z is the atomic number, l the angular momentum quantum number and m the mass. The functions $Y_{nl}(r)$ and $X_{nl}(r)$ are the corrections to the Coulomb potential and the exchange function, respectively and depend on the radial eigenfunction. u_{nl} and $\varepsilon_{n'l,nl}$ are the energy matrix elements. Equation 2.8 can be iteratively solved by choosing a suitable u_{nl}, $Y_{nl}(r)$ and $X_{nl}(r)$ until self-consistency is achieved. A more detailed discussion can be found in references [31, 32, 33, 34].

Multiconfiguration Dirac-Fock (MCDF)

The Multiconfiguration Dirac-Fock method is a relativistic and quantum electrodynamic (QED) extension of the Hartree-Fock method to predict the atomic properties of a multi-electron system. The total wave-function is calculated using the variation principle and the total energy of the atomic system is the eigenvalue of the equation [35, 36]

$$\mathscr{H}^{\text{no pair}}\Psi_{\Pi,J,M}(r_1,r_2,....,r_i,...) = E_{\Pi,J,M}\Psi_{\Pi,J,M}(r_1,r_2,....,r_i,...) \tag{2.9}$$

where Π is the parity, J is the total angular momentum and M is the eigenvalue of J_z which is the projection of J on the z-axis . Here the Hamiltonian $\mathscr{H}^{\text{no pair}}$ can be written as

$$\mathscr{H}^{\text{no pair}} = \sum_{i=1}^{N}\mathscr{H}_D(r_i) + \sum_{i<j}^{N}\frac{1}{r_{ij}} + \sum_{i<j}^{N}B_{ij} \tag{2.10}$$

where the first term is the one electron Dirac operator, the second term is the Coulomb interaction and the third term is the Breit correction. The Breit correction takes into account the electron-electron interactions [36]

$$B_{ij} = \frac{\alpha_i\cdot\alpha_j}{2r_{ij}} - \frac{(\alpha_i\cdot r_{ij})(\alpha_j\cdot r_{ij})}{2r_{ij}^3} \tag{2.11}$$

where α_i are the Dirac matrices. In the MCDF approach the bound state atomic wave-function is described as a linear combination of configuration state function (CSF) as

$$|\Psi_{\Pi,J,M}\rangle = \sum_{\nu=1}^{o} c_\nu\,|\nu,\Pi,J,M\rangle \tag{2.12}$$

where o is the number of configuration functions and c_ν are the mixing coefficients of the respective basis [35, 36]. In the MCDF approach, an initial wave-function is chosen, then the coefficients c_ν are determined by diagonalization of the Hamiltonian matrix. The optimization of the solution takes place by calculating the influence of the atomic nucleus and its N-1 electrons on each individual electron.The improvement of the wave-functions are obtained by self consistency. This process of diagonalization and self-consistency is repeated until complete self-consistency is obtained [35, 36].

Coupled cluster method

A more precise description of a multi-electron system is the consideration of the dynamic electron correlations [37]. One approach that takes these effects into account is the coupled-cluster (CC) method, also known as $\exp(S)$ formalism [39, 40, 38]. The starting point for this method is also the Dirac-Coulomb-Breit Hamiltonian, equation 2.10. In the Fock-space coupled cluster (FSCC) approach, the function space is divided into two parts, a relatively small model space P, which includes all determinants important to the system of interest, and an orthogonal space $Q = 1 - P$. The energy eigenvalues are obtained by diagonalizing the effective Hamiltonian (H_{eff}) in the P space. Even though the FSCC is a very powerful tool for atomic calculations, the accuracy and convergence of this method depends on the partitioning of the function space P and Q.

This can be overcome by using the Intermediate Hamiltonian Fock-space coupled cluster method (IHFSCC) [41], where the P space is partitioned into the main P_m and the intermediate P_i with the corresponding projection operators Q satisfying

$$P_m + P_i = P, \qquad P + Q = 1. \tag{2.13}$$

An intermediate Hamiltonian H_I in P is constructed, the eigenvalues of which give a good approximation to the eigenvalues of the exact Hamiltonian H acting on the entire function space. The intermediate Hamiltonian H_I is of the form $H_I = PHRP$ which gives upon diagonalization the eigenvalues E_m, the orbital energies, of $|\psi_m\rangle$,

$$H_I P |\psi_m\rangle = E_m P |\psi_m\rangle \tag{2.14}$$

where $|\psi_m\rangle$ denotes the eigenstates of H with the largest component in P_m, R is a wave operator operating in P.

2.1.3 Configuration interactions (CI)

The starting point of the configuration interaction linearised single-double coupled cluster (CI+all orders) method is the frozen core Dirac-Fock (DF) V^{N-M} potential [42]. Here, N is the total and M is the number of valence electrons. The effective Hamiltonian ($\hat{H}^{\text{eff}}$) for

the valence electrons is the sum of the single-electron Hamiltonian ($\hat{h}_1(r_i)$) and an operator representing interaction between valence electrons ($\hat{h}_2(r_i, r_j)$) given by [43]

$$\hat{H}^{\text{eff}} = \sum_{i=1}^{M} \hat{h}_1(r_i) + \sum_{i<j} \hat{h}_2(r_i, r_j). \tag{2.15}$$

The single-electron Hamiltonian for a valence electron is of the form

$$\hat{h}_1 = c\alpha\mathbf{p} + (\beta - 1)mc^2 - \frac{Ze^2}{r} + V^{N-M} + \hat{\Sigma}_1 \tag{2.16}$$

where $\hat{\Sigma}_1$ is the single-electron correlation operator responsible for the correlation interaction of a valence electron with the core with the matrix elements [44]

$$\Sigma_{mv} = \rho_{mv}(\tilde{\varepsilon}_v - \varepsilon_m). \tag{2.17}$$

Here, ρ_{mv} is the excitation coefficient of the atomic wave function from the valence state v to another excited state m and ε_m are Dirac-Fock energies of the corresponding single-electron basis states[43]. The $\tilde{\varepsilon}_v$ is taken as the Dirac-Fock energy of the lowest orbital for the particular partial wave. The interactions between the valence electrons is given by

$$\hat{h}_2(r_i, r_j) = \frac{e^2}{|r_i - r_j|} + \hat{\Sigma}_2(r_i, r_j). \tag{2.18}$$

$\hat{\Sigma}_2(r_i, r_j)$ is the screening of the Coulomb interaction between valence electrons by core electrons. The wave function for the valence electrons can be represented as

$$\Psi = \sum_i c_i \Phi_i(r_1, ..., r_M). \tag{2.19}$$

The coefficients c_i and electron energies are extracted by solving the matrix eigen value problem

$$(H_{ij}^{\text{eff}} - E)X = 0 \tag{2.20}$$

where $H_{ij}^{\text{eff}} = \langle \Phi_i | \hat{H}^{\text{eff}} | \Phi_j \rangle$ and $X = c_1, c_2, ..., c_n$. The $\boldsymbol{B}$-spline technique [46] is used to construct the single-electron basis for the calculation of $\hat{\Sigma}_{1,2}$ and for building many-electron basis state Φ_i for CI calculations [43].

Using the above mentioned methods, MCDF, CC and CI, it is possible to obtain the energy of the atomic states, their lifetime and the element-specific ionization potential.

2.1.4 Light matter interaction–two level system

The interaction of an atom with a monochromatic light field can be described in a semiclassical view. In this case, the atom is treated quantum mechanically with a Hamilton operator $\hat{H}_{\text{atom}}$ with eigenstates $|1\rangle$ and $|2\rangle$ while the classical incident monochromatic light field is assumed to be a plane wave with an electric field $\mathbf{E}(z,t) = \mathbf{e}E_0 cos(\omega_L t)$. Here $\mathbf{e}$ represents the unit vector along the polarization of the field and ω_L the frequency of the light. The interaction of a polarizable electric charge distribution with an electric field $\mathbf{E}(t)$ is determined by the electric dipole moment $\mathbf{d} = -e\mathbf{r}$ [47]. The Schrödinger equation for the light-atom interaction can be written as

$$i\hbar \frac{\partial}{\partial t} |\phi\rangle = \hat{H} |\phi\rangle = (\hat{H}_{\text{atom}} + \hat{V}) |\phi\rangle = (\hat{H}_{\text{atom}} - d\mathbf{E}(t)) |\phi\rangle . \tag{2.21}$$

The solution of the Schrödinger equation can be achieved by assuming [47]

$$|\phi(r,t)\rangle = c_1(t) e^{i\omega_1 t} |1\rangle + c_2(t) e^{i\omega_2 t} |2\rangle . \tag{2.22}$$

$\hbar\omega_i$ is the eigenvalue of the eigenstate $|i\rangle$, corresponding to the excitation energy. By inserting 2.22 into the Schrödinger equation 2.21 and taking into account the time propagation of the light wave and the projection of individual eigenstates $|i\rangle$ of the atom, the differential equations for the coefficient $c_1(t)$ and $c_2(t)$ are derived as [48]

$$\begin{aligned} \dot{c}_1(t) &= i\Omega_0 e^{i\omega_{12} t} \frac{1}{2} (e^{i\omega_L t} - e^{-i\omega_L t}) c_2(t) \\ \dot{c}_2(t) &= i\Omega_0 e^{i\omega_{21} t} \frac{1}{2} (e^{i\omega_L t} - e^{-i\omega_L t}) c_1(t). \end{aligned} \tag{2.23}$$

Here $\hbar\omega_{if} = \hbar|\omega_i - \omega_f|$ is the energy difference between the states $|i\rangle$ and $|f\rangle$. $\Omega_0 = \frac{dE_0}{\hbar}$ is the resonant Rabi frequency, with $d = d_{12} = e\varepsilon \langle 1 | \mathbf{d} | 2 \rangle$ is the strength of the transition dipole

moment. The electric dipole operator, **d**, couples atomic states of different parity and with a difference in angular momentum of $\Delta J = 0, \pm 1$. For d the relation [47]

$$d^2 = \frac{3A_{12}\pi\varepsilon_0\hbar c^3}{\omega_{12}^3} \tag{2.24}$$

applies. Here ε_0 is the dielectric field constant, c the speed of light and $A_{12} = \gamma_{12}$ the Einstein coefficient for the transition. Since the frequency of the light field ω_L is close to resonant to the transition frequency ω_{12}, the term $\omega_L + \omega_{12}$ oscillates very fast compared to the difference frequency $\delta = \omega_L - \omega_{12}$ and can be neglected according to the *rotating wave approximation* [47]. With definition of the coefficients $\tilde{c}_1(t) = c_1(t)e^{-i\delta t/2}$ and $\tilde{c}_2(t) = c_2(t)e^{-i\delta t/2}$, equation 2.23 results to [48]

$$\frac{d}{dt}\begin{pmatrix}\tilde{c}_1(t)\\ \tilde{c}_1(t)\end{pmatrix} = \frac{i}{2}\begin{pmatrix}-\delta & \Omega_0\\ \Omega_0 & \delta\end{pmatrix}\begin{pmatrix}\tilde{c}_1(t)\\ \tilde{c}_2(t)\end{pmatrix}. \tag{2.25}$$

The solution is given by [48]

$$\begin{aligned}\tilde{c}_1(t) &= i\frac{\Omega_0}{\Omega}\sin(\Omega t/2)\tilde{c}_2(0) + \left\{\cos(\Omega t/2) - i\frac{\delta}{\Omega}\sin(\Omega t/2)\right\}\tilde{c}_1(0)\\ \tilde{c}_2(t) &= i\frac{\Omega_0}{\Omega}\sin(\Omega t/2)\tilde{c}_1(0) + \left\{\cos(\Omega t/2) + i\frac{\delta}{\Omega}\sin(\Omega t/2)\right\}\tilde{c}_2(0).\end{aligned} \tag{2.26}$$

These equations describe the oscillation between two atomic states $|1\rangle$ and $|2\rangle$ with the Rabi frequency $\Omega = \sqrt{\delta^2 + \Omega_0^2}$ which depends on both, transition properties and laser intensity. This holds for periods (T) shorter than the lifetime of the states $T \ll \tau = 1/\gamma_i$, not taking into account the damping processes like ionization from the upper state or buffer gas-induced population transfer. In order to include the incoherent or dissipative process in the quantum mechanical modelling of the excitation dynamics, it is useful to use the statistical description using the density matrix operator. For pure states the density operator can be written as

$$\hat{\rho} = |\psi\rangle\langle\psi|. \tag{2.27}$$

The diagonal elements $\rho_{mm} = \langle\psi_m|\hat{\rho}|\psi_m\rangle$, correspond to the probability of the residence in the corresponding state ψ_m. They are real numbers and can take values between 0 and 1. The off-diagonal elements are termed as coherences and are generally complex quantities. For a

two-level system the diagonal elements satisfy the relation $\rho_{11}+\rho_{22}=1$. The four elements of the atomic density matrix ρ_{mn} are defined as [47]

$$\begin{aligned}\rho_{11} &= |c_1|^2 \,,\, \rho_{22} = |c_2|^2 \\ \rho_{12} &= c_1 c_2^* \,,\, \rho_{21} = c_2 c_1^*\end{aligned} \tag{2.28}$$

The density matrix elements equation can be derived from equation 2.25 as [47]

$$\frac{d}{dt}\rho_{mn} = \frac{d}{dt}(\tilde{c}_m(t)\tilde{c}_n^*(t)) = \dot{\tilde{c}}_m(t)\tilde{c}_n^*(t) + \tilde{c}_m(t)\dot{\tilde{c}}_n^*(t). \tag{2.29}$$

With $\gamma = \gamma_{21}$ the spontaneous decay from $|2\rangle$ to $|1\rangle$, it results in

$$\begin{aligned}\dot{\rho}_{11} &= i\frac{\Omega_0}{2}(\rho_{21}-\rho_{12}) + \gamma\rho_{22} \\ \dot{\rho}_{22} &= i\frac{\Omega_0}{2}(\rho_{12}-\rho_{21}) - \gamma\rho_{22} \\ \dot{\rho}_{12} &= i\frac{\Omega_0}{2}(\rho_{22}-\rho_{11}) - (i\delta + \frac{1}{2}\gamma)\rho_{12} \\ \dot{\rho}_{21} &= i\frac{\Omega_0}{2}(\rho_{11}-\rho_{22}) + (i\delta - \frac{1}{2}\gamma)\rho_{21}.\end{aligned} \tag{2.30}$$

These are the so-called *optical Bloch equations* for a 2-level system [47, 48]. Apart from the spontaneous decay, stochastic processes such as collisions and ionization, which influence the occupation probabilities and coherences, can be incorporated into the Bloch equations 2.30. In chapter 4 this will be extended to a 5-level rate equation model to describe the properties of the optical transition in nobelium.

2.1.5 Rydberg states and ionization potential

Rydberg atoms are highly excited atoms where one (or more) electron are excited to atomic levels with a very high principal quantum number n [49, 50]. These atoms have several peculiar properties including a strong response to electric and magnetic fields, long decay periods and electron wavefunctions that approximate, under some conditions, classical orbits of electrons about the nuclei [51]. The core electrons shield the electric charge of the nucleus, such that the effective electric potential basically looks like that of a hydrogen atom. As discussed in the section on the hydrogen atom, the level spacing decreases with n^{-3} converging to the ionization potential, being the energy required to remove the electron from the

Table 2.1: Properties of Rydberg atoms.

Property	n dependence
Binding energy	n^{-2}
Energy between adjacent n states	n^{-3}
Orbital radius	n^{2}
Geometric cross-section	n^{4}
Dipole moment	n^{2}
Polarizability	n^{7}
Relative lifetime	n^{3}
Fine-structure interval	n^{-3}

singly charged ion. Therefore, the measurement of such a Rydberg series enables a precise determination of the ionization potential (E_{IP}), which is one of the most fundamental properties of an element. The energy levels, E_n, of the Rydberg states for hydrogen-like atoms can be characterised as [49, 50]

$$E_n = E_{\mathrm{IP}} - \frac{R_M Z^2}{n^2} \tag{2.31}$$

where E_{IP} is the ionization energy, Z the nuclear charge and R_M the reduced Rydberg constant for an atom of mass M. R_M is related to the Rydberg constant $R_\infty = 109737.31568076(96)$ cm^{-1} by

$$R_M = \frac{M}{m_e + M} R_\infty. \tag{2.32}$$

Some important properties of Rydberg atoms and their dependence on the principal quantum number, n, are listed in table 2.1. Equation 2.31 strictly applies only to hydrogen-like atoms and some modifications need to be made for heavier atoms because highly excited Rydberg states have a non-vanishing probability near the nucleus, which decreases with increasing angular momentum l. In addition, the Rydberg electron also causes a polarization in the inner electron shell. This effect can be described by the quantum defect theory [52, 53], which states that the potential near the core differs from a pure Coulomb potential. Thus, for a heavy atom equation 2.31 can be generalised to the Rydberg-Ritz equation as

$$E_n = E_{IP} - \frac{R_M Z^2}{(n - \delta_{nlj})^2} = E_{IP} - \frac{R_M Z^2}{(n^*)^2} \tag{2.33}$$

with the quantum defect, δ_{nlj}, which depends on the angular momentum quantum number l and principal quantum number n. $n^* = n - \delta_{nlj}$ is the effective quantum number. The quantum defect δ_{nlj} of an nlj state can be expressed in Ritz expansion as [53]

$$\delta_{nlj} = \delta_0 + \frac{\delta_2}{(n-\delta_0)^2} + \frac{\delta_4}{(n-\delta_0)^4} + \frac{\delta_6}{(n-\delta_0)^6} + ... \tag{2.34}$$

where $\delta_0, \delta_2, \delta_4, ...$ are constants, where in most cases only an extension to second order is required. Using the combination of equation 2.33 and 2.34 the ionization potential of an element can be extracted [34].

2.1.6 Hyperfine structure

For a nucleus with a non-vanishing nuclear spin I, the I couples to the electronic angular momentum J and results in a total angular momentum F [54, 55, 56, 57, 58]

$$F = J + I. \tag{2.35}$$

If $I \geq J$ then there are $2J+1$ hyperfine components or if $J > I$ then there are $2I+1$ components to the hyperfine splitting. Nuclear properties can be extracted from analysis of the hyperfine splitting of the atomic energy levels.

The electronic levels are influenced by this coupling due to an interaction of the nuclear magnetic dipole moment μ with the magnetic field and of the nuclear electric quadrupole moment Q with the field gradient of the electron wavefuntions. This coupling lifts the degeneracy of the quantum number F and the energy shift for each atomic hyperfine level with respect to the unperturbed fine structure level is given by [56, 58]

$$\Delta E = \frac{A}{2}C + \frac{B}{4}\frac{\frac{3}{2}C(C+1) - 2I(I+1)J(J+1)}{I(2I-1)J(2J-1)} \tag{2.36}$$

where $C = F(F+1) - I(I+1) - J(J+1)$. The hyperfine constants A and B are defined as

$$A = \frac{\mu_I B_e(0)}{IJ} \tag{2.37}$$

and

$$B = eQ_s \left\langle \frac{\partial^2 V_e}{\partial z^2} \right\rangle_{z=0} \tag{2.38}$$

with μ_I denoting the magnetic dipole moment of the nucleus, $B_e(0)$ denoting the magnetic field generated by the electron at the nucleus, Q_s the spectroscopic quadrupole moment and $\langle \partial^2 V_e/\partial z^2 \rangle_{z=0}$ the electric field gradient generated by the electrons at the nucleus [58].

For atomic transitions in which both levels are subject to hyperfine splitting the frequencies, $\bar{\nu}$, at which the resonant excitation between initial $|i\rangle$ and upper states $|f\rangle$ occur is given by [57]

$$\bar{\nu} = \bar{\nu}_{\text{cen}} + \alpha_f A_f + \beta_f B_f - \alpha_i A_i - \beta_i B_i \tag{2.39}$$

where $\bar{\nu}_{\text{cen}}$ is the centroid, and α and β are given by

$$\alpha = \frac{C}{2} \qquad \text{and} \qquad \beta = \frac{1}{4} \frac{\frac{3}{2}C(C+1) - 2I(I+1)J(J+1)}{I(2I-1)J(2J-1)} \tag{2.40}$$

The strength of each transition depends on the nuclear spin I, as well as the F and J values of the upper and lower atomic states. The intensities can be expressed in terms of a Wigner $6-j$ symbol of the coupling of the angular momenta involved in the transition to give [55]

$$\text{Intensity} \propto \frac{(2F_f+1)(2F_i+1)}{2I+1} \begin{Bmatrix} J_f & F_f & I \\ J_i & J_i & 1 \end{Bmatrix}^2 . \tag{2.41}$$

Fitting the hyperfine spectrum with numerical routines such as χ^2-minimisation, the centroid frequency, and the hyperfine constants A and B can be evaluated. Also, the nuclear spin I and the angular momentum J are probed. From a comparison of these values with measurements on reference isotopes where the nuclear properties are known, the properties of exotic, short-lived isotopes can be deduced with high precision. For elements which have no reference isotope, the extraction of the nuclear magnetic moment μ_I and the spectroscopic quadrupole moment Q_s requires knowledge on the atomic properties as the magnetic field, B_e, and the electric field gradient, $\langle \partial^2 V_e/\partial z^2 \rangle_{z=0}$. These can be calculated using atomic theories as discussed in previous sections.

2.1.7 Isotope shift

The isotope shift denotes the change in the centroid frequency of a spectral line between two isotopes and is caused by the change in mass and size of the nucleus. The isotope shift of an isotope with mass number A' compared to an isotope with mass number A, is defined as

$$\delta\bar{\nu}_{\mathrm{IS}}^{AA'} = \bar{\nu}^{A'} - \bar{\nu}^{A} \tag{2.42}$$

where $\bar{\nu}^{A'}$ and $\bar{\nu}^{A}$ are transition frequencies for the isotopes A' and A, respectively. The isotope shift can be approximated as a composition of two independent components, the mass shift $\delta\bar{\nu}_{\mathrm{mass}}^{AA'}$ and the field shift $\delta\bar{\nu}_{\mathrm{field}}^{AA'}$ as [59]

$$\delta\bar{\nu}_{\mathrm{IS}}^{AA'} = \delta\bar{\nu}_{\mathrm{mass}}^{AA'} + \delta\bar{\nu}_{\mathrm{field}}^{AA'} \tag{2.43}$$

which will be discussed separately in the following.

Mass shift

The mass shift, $\delta\bar{\nu}_{\mathrm{mass\ shift}}^{AA'}$, is separated into two components, the normal mass shift and specific mass shift. The normal mass shift arises when taking the finite mass of the nucleus into account. The energy levels of the atom, in this case, will be raised compared to an atom with an infinitely heavy nucleus. The specific mass shift arises due to the influence of the changed reduced mass in the electron-electron correlations within a multi-electron atom. Therefore, the mass shift can be written as

$$\delta\bar{\nu}_{\mathrm{mass\ shift}}^{AA'} = (N+S)\frac{A'-A}{AA'} \tag{2.44}$$

where N and S are constants for normal and specific mass shift, respectively. The normal mass shift constant, N, can be exactly calculated, whereas the specific mass shift constant, S, must either be theoretically evaluated or calibrated [58, 59].

Field shift

In the case of heavy atoms, the isotope shift is dominated by the field shift. This shift is due to the change in the nuclear charge distribution as a result of the change in the neutron number,

which modifies the Coulomb interaction with the electrons. The charge density is assumed to be constant over the nuclear volume, thus the perturbation in the electronic energy levels can be shown to be equal to the mean-square charge radius [57], given by

$$\langle r^2 \rangle = \frac{\int_0^\infty \rho(r) r^2 dV}{\int_0^\infty \rho(r) dV} \tag{2.45}$$

where $\rho(r)$ is the nuclear density. The field shift is sensitive to changes in the mean-square charge radii $\delta\langle r^2\rangle^{AA'}$ and rather insensitive to details of the nuclear charge distribution itself [60]. Thus, the field shift is given by

$$\delta\bar{\nu}^{AA'}_{\text{field shift}} = \frac{\pi a_0^3}{Z} \Delta|\psi(0)|^2 f(Z) \delta\langle r^2\rangle^{AA'} \tag{2.46}$$

where a_0 is the Bohr radius, $\Delta|\psi(0)|^2$ is the change in the electron probability density function at the nucleus and $f(Z)$ is the relativistic correction factor [61].

Total isotope shift

The total isotope shift can therefore be expressed as [57]

$$\delta\bar{\nu}^{AA'}_{\text{IS}} = (N+S)\frac{A'-A}{AA'} + F\delta\langle r^2\rangle^{AA'} \tag{2.47}$$

The atomic factors N, S and F purely depend on the atomic transitions and $(A'-A)/AA'$ and $\delta\langle r^2\rangle^{AA'}$ contain only nuclear properties. For isotopes of the same element, the atomic transition between s and p states produces the largest field shifts and are thus more sensitive to the change in the mean-square charge radius, $\delta\langle r^2\rangle^{AA'}$.

2.2 Theoretical consideration for nuclear physics

2.2.1 Liquid drop model

The liquid drop model (LDM) [62] considers a macroscopic approach to describe the properties of the nucleus. It treats the nucleus as an incompressible fluid to describe properties of a nucleus such as size, binding energy, mass and fission barrier. Von Weizsäcker developed

a semi empirical approach to describe the binding energy of the nucleus as the sum of five energy terms accounting for different interactions:

$$B.E. = a_v A - a_s A^{2/3} - a_c Z(Z-1)A^{-1/3} - a_a (N-Z)^2 A^{-1} \pm \delta \tag{2.48}$$

The volume term accounts for the binding energy per nucleon, the surface term accounts for the surface nucleons interaction, the repulsive Coulomb energy to account for the electrostatic interaction between protons, an asymmetry term to account for the Pauli exclusion principle and the pairing term to account for the pairing of valence protons and neutrons.

An extension of the liquid drop model is the droplet model, which introduces the proton and neutron distributions by minimizing the total energy of the system. This variation in nuclear charge distribution allows for surface diffuseness, in comparison to the sharp cut-off assumed in the liquid drop model and also for a charge redistribution inside the nucleus. In addition to the binding energy, the droplet model can predict the isotope shift and the charge radii of the nucleus [63].

2.2.2 The shell model

The shell model describes the nuclear shell structure, which explains the increased nuclear stability at certain proton and neutron numbers, known as the magic numbers [64]. The basic assumption of the shell model is that a single nucleon's motion is determined by the potential created by all other nucleons in the nucleus. The most realistic potential that describes this potential is the Wood-Saxon potential of the form [65, 66]

$$V(r) = -\frac{V_0}{1+\exp(\frac{r-R}{a})} \tag{2.49}$$

where $R = 1.25\ A^{1/3}$ fm, $a = 0.524$ fm and V_0 is the depth of the potential well, which is around 50 MeV [66]. The energy levels are obtained by solving the Schrödinger equation. This can reproduce only the very low-lying shell closures or magic numbers [65]. The resulting energy levels are shown in figure 2.1 (left). Inclusion of the nuclear spin-orbit interaction in the nuclear potential, $V_{SO}(r)\mathbf{l.s}$, re-orders the energy levels and the experimentally observed magic numbers are reproduced [65, 67]. The inclusion of the spin-orbit coupling lifts the degeneracy of the $l > 0$ levels and splits the energy levels in accordance with the value of l. The resulting energy levels are shown in figure 2.1 (right). The shell model postulates that only a single, unpaired nucleon governs the properties of the nucleus. This results in the

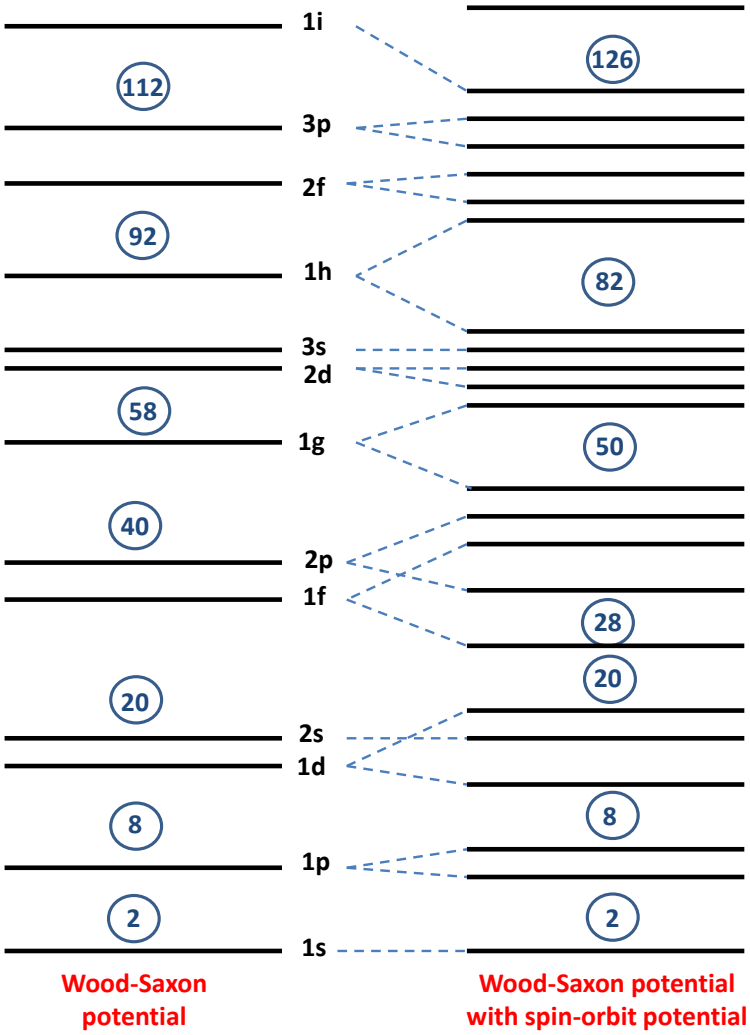

Figure 2.1: The energy levels of the shell model. Left side: Calculated from the Wood-Saxon potential. Right side: Including the spin-orbit coupling. [65]

spin of j and a parity $(-1)^l$ for the nucleus whose valence nucleon occupies the energy level $\mathrm{n}l_j$.

2.2.3 The Nilsson model

Despite the shell model being very versatile in predicting the microscopic behaviour of the nucleons, it is limited only up to nuclei around the lead (Pb) region. For heavier systems there are many valence nucleons and the nucleus may become deformed. This makes calculations challenging and the Nilsson model describes the structure for deformed nuclei [68, 69]. The Nilsson potential is expressed as

$$V_{Nil} = \frac{m}{2}[\omega_x^2(x^2+y^2) + \omega_z^2 z^2] - \kappa\hbar\omega_0[2\mathbf{l}.\mathbf{s} + \mu(\mathbf{l}^2 - \langle\mathbf{l}^2\rangle_N)]. \tag{2.50}$$

$\omega_{x,y,z}$ are related to the deformation by

$$\omega_x^2 = \omega_y^2 = \omega_0^2(1+\frac{2}{3}\delta) \tag{2.51}$$

and

$$\omega_z^2 = \omega_0^2(1-\frac{4}{3}\delta) \tag{2.52}$$

where ω_0 is the spherical oscillator frequency ($\hbar\omega_0$ =41 $A^{1/3}$ MeV) and $\delta \approx \frac{3}{2}\sqrt{\frac{5}{4\pi}}\beta_2$ is the nuclear quadrupole deformation term. Thus, the first term in equation 2.50 gives the deformation in terms of the oscillation frequency (ω_0) along a given deformation axis. For a prolate deformed nucleus δ, β_2>0 whereas for an oblate deformed nucleus δ, β_2<0. The Nilsson model predicts the energy levels and the shell gaps of nuclear orbitals as a function of the deformation. More information on the Nilsson model can be found in *e.g.* ref. [69]. A Nilsson diagram showing the single-particle energy levels for proton with $Z \geq 82$ as a function of deformation parameter ε_2 is shown in figure 2.2. Another Nilsson diagram for single-particle neutron levels with $N \geq 126$ is shown in figure 2.3.

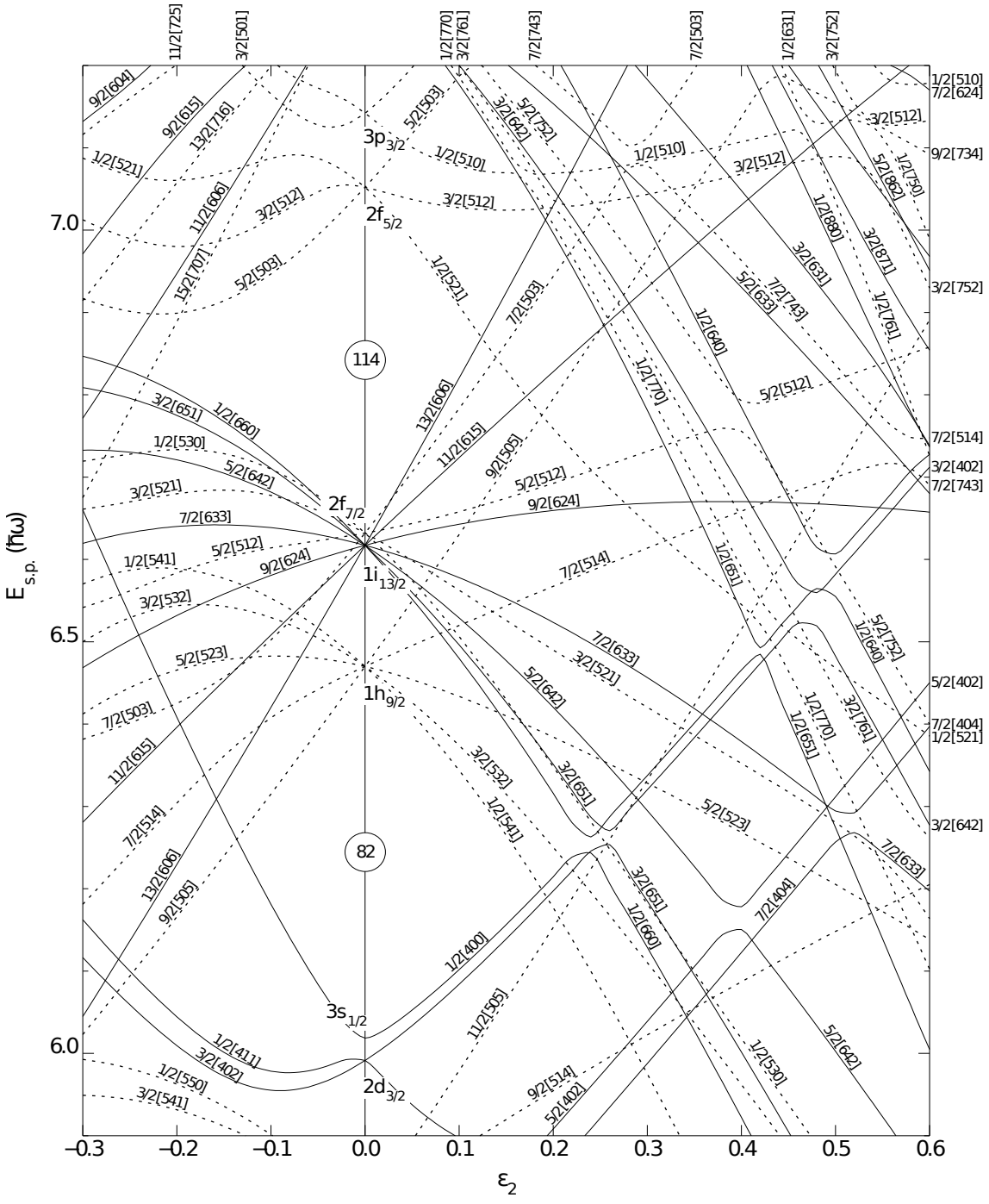

Figure 2.2: Nilsson diagram for protons $Z \geq 82$. Adopted from [70].

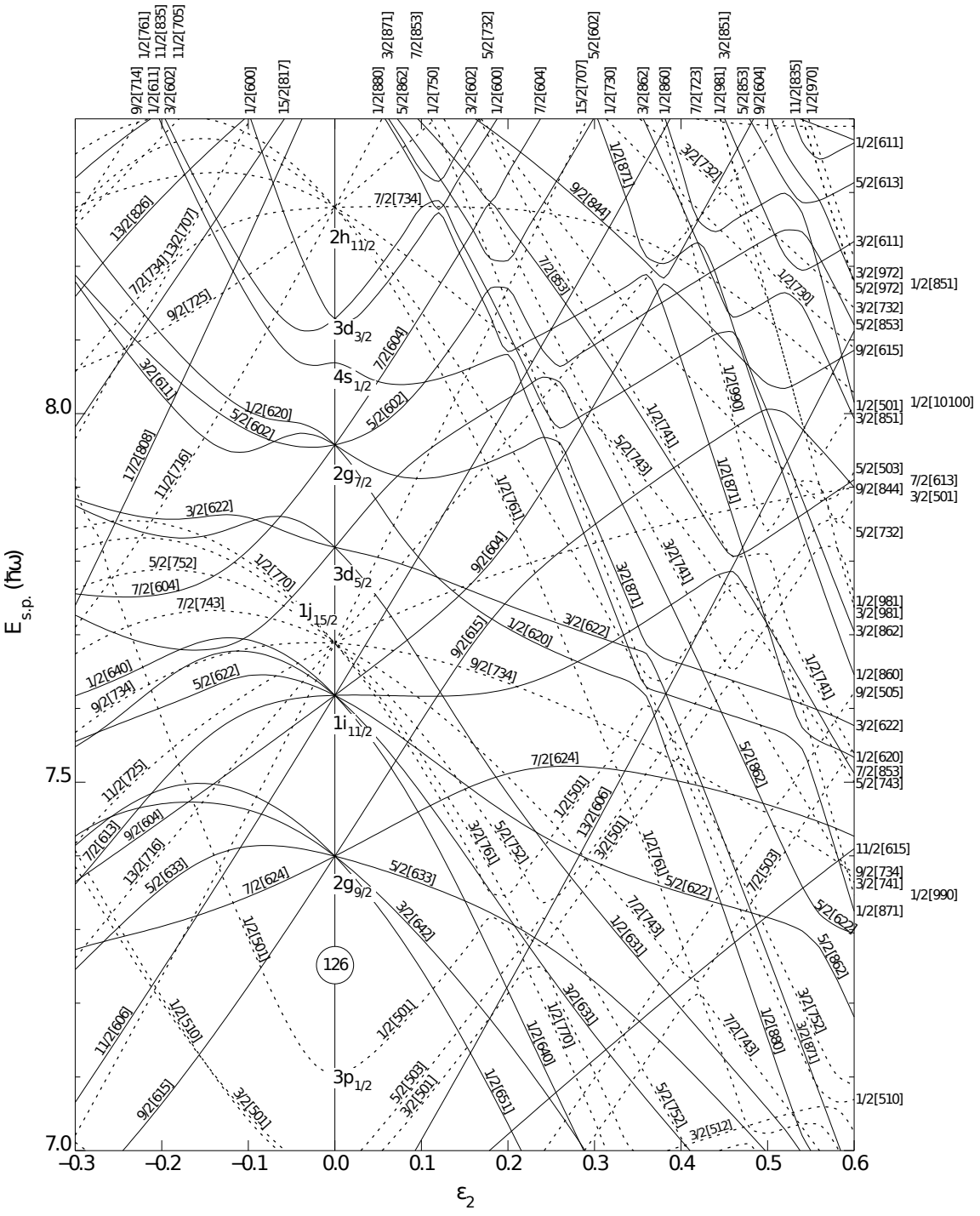

Figure 2.3: Nilsson diagram for neutrons $N \geq 126$. Adopted from [70].

3 Experimental Set-up

Laser spectroscopy on nobelium was performed using the RAdiation Detected Resonance Ionization Spectroscopy (RADRIS) technique. This technique is highly efficient and selective for radionuclides featuring an alpha- or fission-decay branch. This technique was originally developed for laser spectroscopy on americium fission isomers [71, 72] and later on was adopted and optimized for the search of atomic levels in No [27, 73]. The RADRIS method exploits a two-step photoionization technique, whereby one laser excites an electron to an excited state and another laser ionizes the atom. In this chapter, the production and isolation of nobelium isotopes will be discussed before an introduction to the details of the RADRIS set-up and the laser system in use will be given. In addition, the data acquisition and control system developed for the level search including primary-beam control, gas cell operation, laser system, signal measurements as well as a continuous monitoring of all relevant parameters will be discussed in detail. The establishment of this system allowed for a reliable and efficient operation of the set-up crucial for this kind of experiments with minute quantities of sample atoms. The data acquisition system allows different measurement modes and has been tested and used in three different beamtimes.

3.1 On-line set-up

The RADRIS set-up consists of an on-line optical gas cell and multiple laser systems that will be described later on in this chapter. The on-line optical gas cell is placed behind the velocity filter SHIP (Separator for Heavy Ion reaction Products) at the GSI Helmholtzzentrum für Schwerionenforschung in Darmstadt [74, 75, 76]. A schematic diagram of SHIP is shown in figure 3.1 (a). The nobelium isotopes ^{252,253,254}No, are produced in the two-neutron evaporation channel of the complete-fusion of ^{48}Ca with ^{206,207,208}Pb in the reactions ^{206}Pb(^{48}Ca, 2n)^{252}No, ^{207}Pb(^{48}Ca, 2n)^{253}No and ^{208}Pb(^{48}Ca, 2n)^{254}No at ^{48}Ca beam energies of about 217 MeV with cross-sections 515^{+80}_{-47} nb, 1310^{+430}_{-410} nb and 2050^{+460}_{-340} nb respectively [77]. For our experiments, a ^{48}Ca^{10+} beam from the universal linear accelerator (UNILAC) was used, which exhibits a macro-pulse structure of 5 ms beam-on and 15 ms beam-off. The target consists of 8 segments of PbS, with an average thickness of about 500 μg cm^{-2}, mounted on a wheel. Typical beam intensities of 0.7 particle microamperes

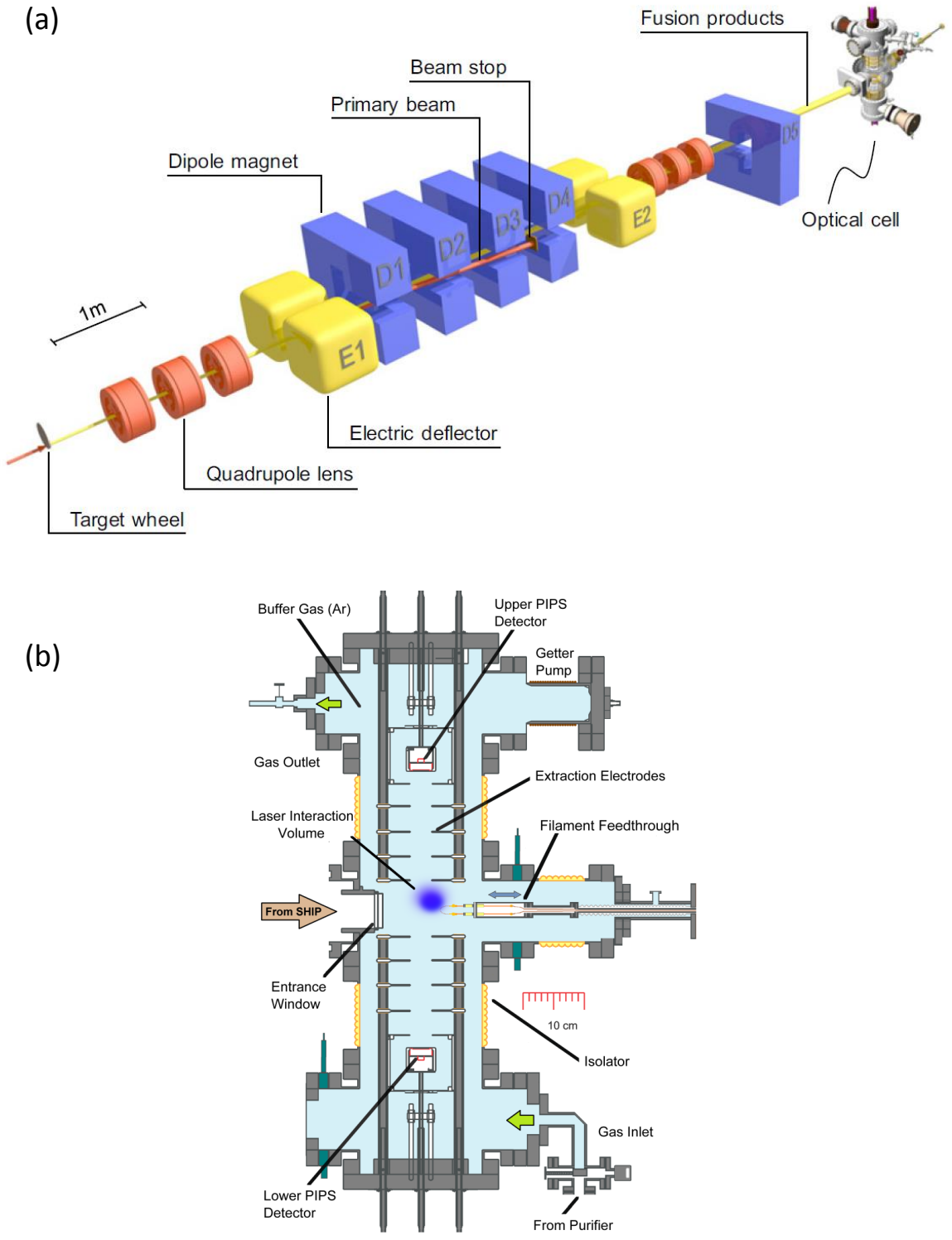

Figure 3.1: Schematic view of the experimental set-up. (a) velocity filter SHIP with production target and the buffer-gas stopping cell. (b) Interior of the buffer gas cell. Figures adopted from [27, 78].

Table 3.1: Electric potentials applied on the individual electrodes for two different configurations for: collection onto the filament and for guiding to the detector.

Configuration	To filament	To detector
Filament	300 V	1015 V
Cross-piece	746 V	1025V
Opposing electrode	746 V	1025 V
Electrode 1	749 V	1000 V
Electrode 2	800 V	
Electrode 3	605 V	
Electrode 4	580 V	
Cage	245 V	
Detector cage	0 V	

(about 4.4×10^{12} particles per second) were provided by the UNILAC. The beam was further chopped in accordance with user defined measurement cycles [73].

The fusion products recoil with a mean kinetic energy of about 41 MeV [27], and are separated from the ^{48}Ca primary beam before they are implanted into a buffer-gas filled stopping cell which is installed at the focal plane of SHIP. The implantation rate of the fusion products was checked by a retractable position-sensitive 16-strip silicon detector placed in front of the cell. The buffer-gas filled stopping cell consists of a catcher filament, eight disk shaped electrodes and two Passivated Implanted Planar Silicon (PIPS) semiconductor detectors. A schematic diagram of the on-line set-up is shown in figure 3.1 (b). The high pressure inside the gas-cell is separated from vacuum of the velocity filter SHIP by a 3.5 μm-thick aluminium-coated mylar foil. The foil is supported by a 1 mm thick stainless steel support grid made out of 0.5 mm thick wires with a spacing of 9 mm, which results in geometrical efficiency of 90%. The entrance window has an inner diameter of 56 mm, matching the incoming recoil beam size of about 50×22 mm^2 (FWHM). The catcher filament is made out of 125 μm thick tantalum (Ta) wire, crimped onto current leads made of silver-plated copper wires. As the detector is placed on ground potential, the electrodes, as well as the central piece of the optical cell and the filament itself have to be biased to high electrical voltages to allow for an efficient guidance of the ions to this detector. Two operation modes were applied: 1. collecting on the filament and 2. guidance to the detector. The power supply for the filament (Elektro-Automatik, EA-PSI 8032-10 DT [79]) is galvanically isolated and can be biased up to 2 kV. The filament is mounted onto a retractable feedthrough, which is at the same electric potential as the central cross-piece. The configuration of electric potentials applied on the electrodes are summarized in table 3.1.

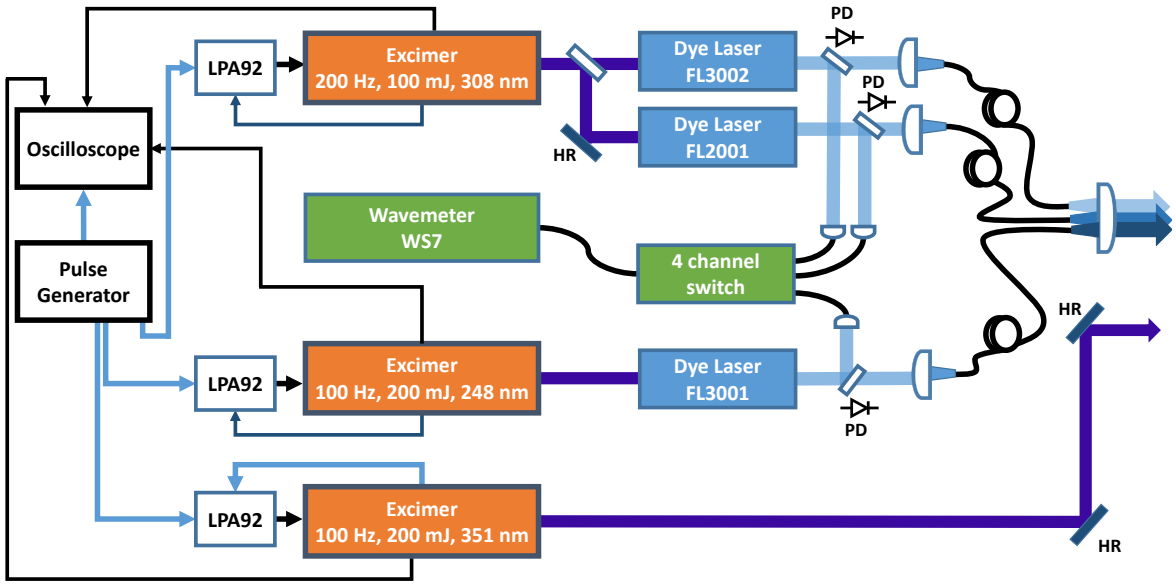

Figure 3.2: Block diagram of the laser systems. PD: fast photodiodes and HR: High reflective mirror.

The gas-cell is filled with about 50-100 mbar of high purity (99.9999%) argon gas to stop the high energetic fusion evaporation products. The high purity of the buffer gas is crucial for the experiment, since impurities in the buffer gas can lead to loss in efficiency due to neutralization from charge exchange processes or due to molecule formation with oxygen and/or hydrogen. Preceding to on-line experiments the gas-cell is heated up to 100 °C at vacuum conditions. Pressures as low as 2×10^{-8} mbar can be reached using a turbo-molecular pump and an ion-getter pump (C-100 MK5, SAES). To reduce the impurities to ppb level during normal operation, the argon gas is passed through a getter-based purifier (MonoTorr: heated getter purifier) before injecting it into the gas-cell. In order to exchange the gas inside the cell, a constant gas flow is maintained, by the use of a needle valve. This helps to maintain the purity of the argon gas inside the cell. The pressure is regulated by a mass-flow controller in conjunction with a capacitor-based pressure gauge. The purity of the gas is monitored by a residual gas analyser (RGA) (Pfeiffer Vacuum Prisma Plus) equipped with a turbo-molecular pump and connected to the gas-cell via a needle valve to limit the pressure inside the RGA to below 10^{-5} mbar. The partial pressure of the residual impurities are monitored during the on-line measurements.

The laser system consists of three tunable dye lasers (Lambda Physik FL and LPD series) which are pumped by two excimer lasers (Lambda Physik, LPX2xxi series). The schematic layout of the laser system is shown in figure 3.2. In order to access a wide range of possible

wavelengths, one excimer laser (LPX210i) is operated with a Kr:F gas mixture resulting in an emission wavelength of 248 nm. This enables a dye laser operation in the ultraviolet (UV) regime between 311-352 nm. The second excimer laser (LPX240i) is operated with a Xe:Cl gas mixture with an emission wavelength of 308 nm. This enables the dye laser light emission starting from 350 nm upwards. Each dye laser can provide pulse energies of at least 200 μJ with a pulse duration of about 18 ns. These dye lasers provide tunable laser radiation for the level search. The third excimer laser (LPX220) is operated with a Xe:F gas mixture with a laser radiation of 351 nm and can deliver pulse energies up to 150 mJ. This laser is used for the second, non-resonant ionization step during level search. All lasers are operated at a repetition rate of 100 Hz [27].

The wavelengths of the dye laser beams are measured in parallel using a wavemeter (High-Finesse WS7) in combination with a four-channel fibre switch. The laser light from the dye lasers is transported to the experimental place using multi-mode quartz fibres with a core diameter of 600 µm (LEONI Fiber Optics GMBH). An overall transmission of 30-50% was achieved for wavelengths in the range 300-430 nm. For maximum spatial overlap of the laser beams, a dedicated multi-fiber coupler was designed and up to 90% geometrical overlap was achieved [25]. Here, the laser beams are collimated using a 2-inch lens with a focal length of 75 mm to obtain parallel beams of 20 mm in diameter. The laser radiation for the ionizing laser was collimated using a 10 m focal length lens and transported to the experimental set-up using high reflective (HR) mirrors. A laser beam transport efficiency of about 45% and a beam profile of 25×35 mm^2 at the cell was obtained [27, 73].

In order to guarantee a proper timing of the individual dye lasers relative to the second, ionizing step, a pulse generator (Model 555, Berkeley Nucleonics Corporation) is used to trigger all excimer lasers individually. The trigger signals for each excimer lasers are fed to an active synchronization unit (LPA92, Lambda Physik), which stabilizes the light output timing to a fixed delay using a feedback signal from a fast photodiode. The timing as well as the laser power of each laser is monitored continuously using dedicated photodiodes. To determine the lifetime of an excited state by delayed ionization, the time difference from the photodiode signal was measured using a multi-channel analyser (MCA) in conjunction with a time-to-analog-converter (TAC). The reader is referred to [25, 27] for more information about the on-line gas cell.

3.2 Off-line set-up

Besides the on-line set-up, a dedicated off-line set-up is used for resonance ionization measurements on ytterbium (Yb, $Z = 70$), the chemical homologue of nobelium. A schematic

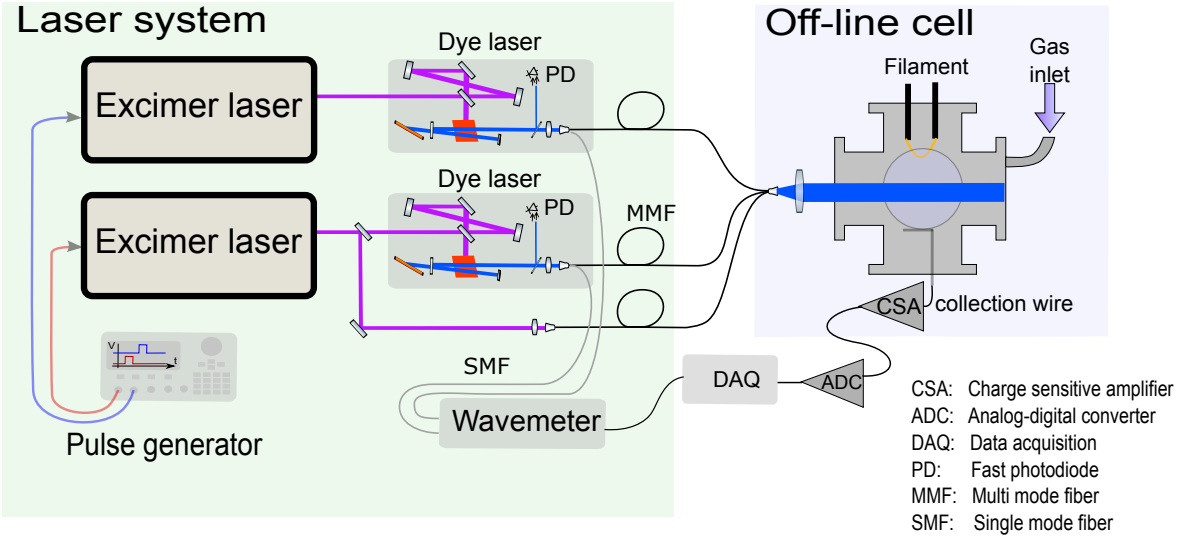

Figure 3.3: Schematic overview of the off-line measurement set-up comprising of the off-line buffer gas cell along with the laser systems and the data acquisition system.

diagram of the off-line set-up is shown in figure 3.3. As a buffer gas cell, a standard CF-63 cross-piece equipped with two quartz windows for laser access is used. The filament is composed of a 12.5 μm thick tantalum foil onto which a 25 μm thick ytterbium foil is clamped. The ytterbium atoms are evaporated by resistive heating of the tantalum foil. The method leads to a long-term stable production of Yb. The gas cell is filled with argon gas of 99.9999% purity. Two tunable dye lasers pumped by an excimer laser operating at 308 nm in combination with an excimer laser at 351 nm, for non-resonant ionization, are typically used for off-line measurements. All the lasers operate at a repetition rate of 100 Hz with a pulse energy of around 1 mJ for the dye lasers and around 10 mJ for the excimer laser. Laser light is transported to the experimental set-up using UV optical fibres and collimated using a 2-inch lens of 75 mm focal length. The created photo-ions are transported by electric fields to a detector, which is a biased wire, connected to a charge-sensitive preamplifier. The accumulated charge is detected in coincidence with the laser pulse. The amplitude of this signal is proportional to the number of collected photo-ions and is recorded in conjunction with the set wavenumber and the time delay [28, 80].

3.3 Data Acquisition and measurement control system

In this section the data acquisition and the measurement control system developed for the laser spectroscopy of the heavy elements will be discussed. During the laser spectroscopy measurements, several digital and analog signals need to be managed and processed simultaneously, thus a listmode data acquisition (DAQ) system is necessary. Also the synchroniza-

Table 3.2: Features of the FPGA-based data acquisition system with reconfigurable I/O's (NI 7833R).

Bus type	PXI
Clock frequency	40 MHz
Digital I/O's	96
Analog inputs	8 ($\pm$10 V)
Analog outputs	8 ($\pm$10 V)
I/O resolution	16 bit
Sampling rate	200 kHz/channel
DAQ software	LabVIEW based

tion of the trigger signals and proper assignment of the time stamps for each registered event has to be considered. In order to accomplish this a field-programmable gate array (FPGA) based multi-function DAQ, NI PXI 7833R [81], controlled by a computer is used. All the analog and digital inputs/outputs (I/O's) of the DAQ system are reconfigurable with the National Instruments Labview FPGA module. This module allows a flexible modification and adjustment in the signal processing structure. The DAQ provides the following features or capabilities:

- Complete control of the synchronization and timing of all signals and operations with a 25 ns time resolution.
- Assignment of proper time stamp for all the registered events.
- Ability to communicate with other I/O devices with user-defined communication protocols.
- Simultaneous analog input up to 200 kHz and simultaneous analog output up to 1 MHz sampling rate.

Features of the DAQ system are tabulated in table 3.2. A NI-VISA server is used for the communication between the remote PXI 7833R and the host computer, which interprets the DAQ system as a locally installed VISA device. The DAQ system is connected to the measurement computer via a PCI-Express interface. The DAQ system is controlled and read out by a LabVIEW-based software.

During the on-line measurement the control and DAQ system needs to handle a multitude of functions. These include the controlling and monitoring of the primary beam current, laser system parameters, filament temperature and electric potentials of the electrodes and the pressure inside the gas cell. These tasks are distributed among several personal computers (PC) communicating with each other via TCP protocols in a local area network as

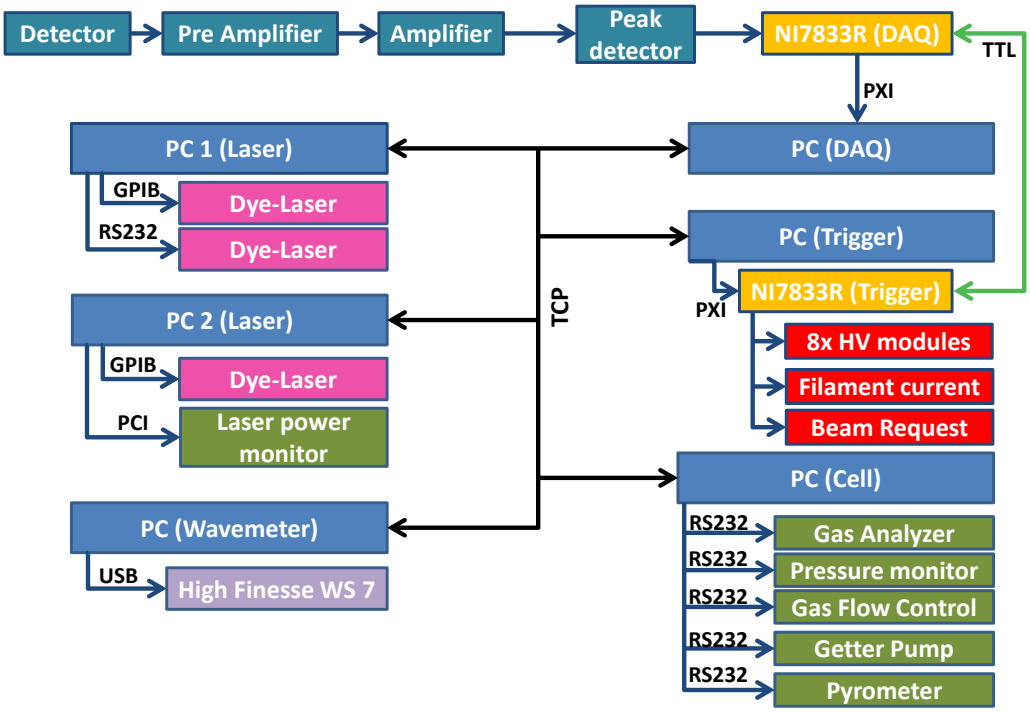

Figure 3.4: Block diagram of the data acquisition the measurement control system.

shown in figure 3.4. After a successful ionization process, the radioactive decays of the ions collected on the thin mylar-foil, placed over the detectors, are registered using the PIPS detector. The energy equivalent charge at the anode of the detector is converted into a voltage signal featuring a steep rise time in the region of 20-30 ns and a longer decay time of about 50 μs with the aid of a charge-sensitive preamplifier (Canberra 20046) [83]. The main amplifier (Ortec model number 471 [84]) generates a bipolar signal with a duration of up to 5 μs. The signal amplitude obtained is proportional to the energy of the emitted $\alpha-$particle or fission products, in the case of on-line experiments, or to the number of the accumulated ions in off-line experiments. This amplified signal is fed into a peak detector and hold unit (built by LMU Munich), which gives a signal of constant voltage of the same amplitude that lasts for a user defined period $< 100\,\mu$s. The peak detector also generates a fast gate signal which is detected on a digital port of the DAQ system (PXI 7833R), determining the time stamp of the signal and triggering the ADC. The information on the registered signal are then transmitted to a PC for storage and analysis. Another DAQ system (PXI 7833R), controlled by another dedicated PC, is used for triggering and controlling the other set-up components. For instance, this is used to trigger the filament current and the HV modules and to chop the primary beam according to a user-defined cycle time.

The pressure inside the gas cell is a crucial parameter which needs to be monitored continuously. It is monitored using a capacitor type pressure gauge connected to a controller (Maxigauge, Pfeiffer Vaccum) [85]. The argon gas inside the cell is continuously evacuated via a needle valve placed near the upper detector (see figure 3.1). In order to keep the pressure inside the cell constant, argon gas needs to be injected at a continuous rate. This is achieved by a regulated mass-flow controller (Pfeiffer Vacuum RVC 300) [86]. Both units are connected to a control PC via serial RS232 interfaces. The pressure is registered every second each time the data acquisition is started and the data is transferred via TCP protocol to the data acquisition PC. The electric potentials of the filament as well as the ion optics electrodes are provided by seven HV modules (HCE 7-3500, up to +3.5 kV, and HCE 7-6500, up to +6.5 kV) [87]. The HV modules work in stand-alone or in external control mode. They also provide analog outputs of 0-10 V for monitoring purposes. Seven analog outputs of the PXI 7833R DAQ system are used to control the voltages of these modules. The monitor outputs of the HV models are fed into a NI PCI 6014 DAQ system [88] which reads the potentials every 5 s and displays them in a graphical representation in a LabVIEW based acquisition software.

To control the wavelength of the laser radiation, each dye laser is equipped with a stepper motor and a motor controller. The motor controllers of two lasers are connected to a PC via GPIB (General Purpose Interface Bus), while for the third dye laser a serial interface (RS-232) is used. The dye laser control software is developed using LabVIEW and can run in a stand alone version or can be externally triggered by the DAQ software during online measurements. The power of the dye lasers is also continuously monitored using fast photodiodes (PD, see figure 3.2) and acquired using the NI PCI 6014 DAQ system.

The developed data acquisition software allows for an efficient readout of the remote PXI 7833R DAQ system. A schematic block diagram of the LabVIEW-based DAQ software is shown in figure 3.5. On starting the LabVIEW DAQ program names log and data files according to the date followed by an integer, in a user-defined directory. The data are saved in ASCII format. Different measurement possibilities are available:

- The default mode (Time): In order to optimize the cell-pressure or any other cell parameter, the user can choose the time measurement mode, which is the default mode of the program. In this mode the user can define a measurement time for the program to run in which the signal is recorded against the elapsed time. This is in particular useful for optimization routines.

- The laser-scan mode: In this mode the user can scan all activated dye lasers simultaneously. Here, a measurement time for each scan step has to be defined, after which the

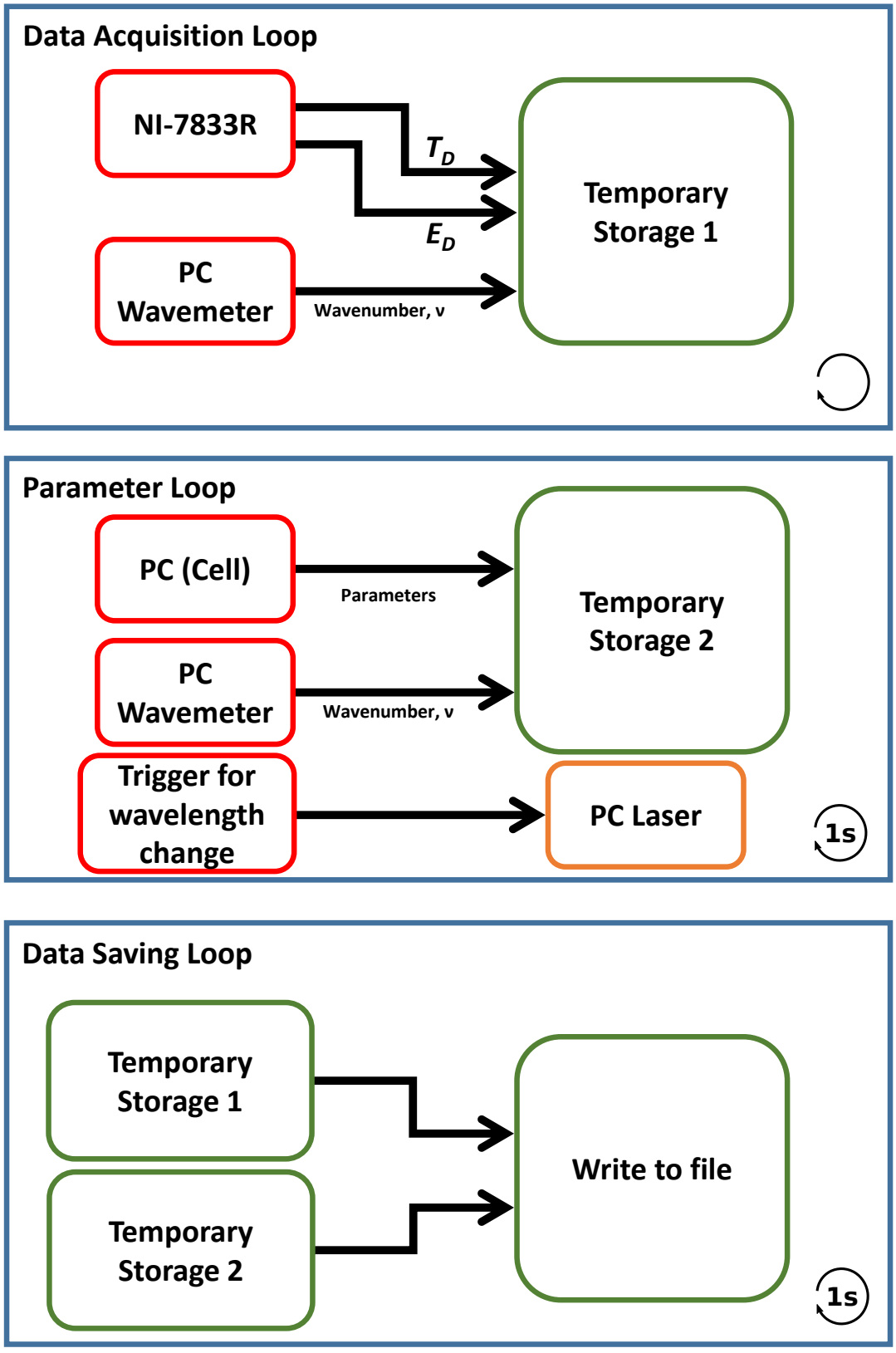

Figure 3.5: Block diagram of the data acquisition (DAQ).

program triggers a wavelength change to the initialized lasers. The size of frequency steps is defined in the respective dye laser control programs independent of the control software. Only one dye laser scan is shown on the user interface for monitoring purposes in this mode.

- The electric potential scan mode: In this mode the user can scan the potentials of the ion optics while keeping all the other cell parameters constant.

The heart of the DAQ software is the data acquisition loop. Each event registered with the PXI 7833R DAQ system is assigned a proper time stamp and stored in a temporary storage (1) along with the recorded wavenumbers. The parameters of the set-up, for example, the cell pressure, the laser wavenumber and the primary beam current, are acquired at different PCs and are communicated via the TCP protocol for saving in a temporary storage (2). Every second the data from the temporary storages (1 and 2) are transferred in a FIFO (first in, first out) logic to the data saving loop where it is written to a file. At present the DAQ system has the possibility to acquire 3 signals from up to three detectors simultaneously and a number of measurements were performed to test the speed and reliability of the DAQ system using signals from a pulse generator. The dead time losses of the detection system were well below 0.5% until the signal rate approached 8 kHz after which the losses started to increase reaching about 2% at a signal rate of about 10 kHz. The results for the dead time loss of the DAQ is shown in the Appendix 8.1.

4 Investigation of buffer-gas quenching of the first excited state in nobelium atoms

During the on-line experiments on nobelium, ^{254}No, the first optical transition of nobelium was observed [24]. A spectral range ranging from $25,000 - 33,000$ cm^{-1} was searched for this atomic transition. In his work, Lautenschläger (ref. [25]) analysed the saturation behaviour of the observed $^1S_0 \rightarrow {}^1P_1$ ground state transition using a simple two-level scheme (see figure 4.1 (a)) with the fit resulting in an Einstein coefficient $A_{ki} \geq 6.3 \times 10^7$ s^{-1}. The delayed ionization measurement, which gives access to the lifetime of the $^1P_1$ state, however showed a long tail indicating the presence of a long-lived state in addition to the short lived $^1P_1$ state. Fits using two exponential curves, one with a large decay-constant for the short-lived state, the other with a small decay-constant in order to compensate for the long decay tail, extracted lifetimes of $\tau_1 = 16$ ns and $\tau_2 = 106$ ns (see figure 4.1(b)). This lifetime value of the $^1P_1$ state is not in agreement with the theoretical calculation of $\tau = 2$ ns [36, 39, 89]. This discrepancy led to a detailed investigation of the effect of gas-induced quenching of atomic states in the chemical homologue, ytterbium ($Z = 70$, Yb), a stable element with a similar atomic level structure as No, and for which the atomic structure is very well studied [90, 91, 92, 93, 94]. Furthermore, a multi-level rate equation model was developed to describe all the experimental data. This chapter presents the off-line measurements on ^{nat}Yb and the validation of the developed rate equation model on Yb after which it was applied to No.

4.1 Quenching in a buffer gas environment

The off-line set-up as discussed in chapter 3.2, was used for performing two-step resonance ionization spectroscopy (RIS) on ^{nat}Yb. The first, resonant step was tuned to excite the $^1S_0 \rightarrow {}^1P_1$ ground state transition at a vacuum wavelength of 398.9 nm. The second non-resonant step was provided by an excimer laser at 351 nm. Figure 4.2 shows a simplified ionization scheme. The lifetime of an excited atomic state can be measured by delaying the second laser pulse relative to the first excitation step. Figure 4.3 (a) shows the delayed ionization

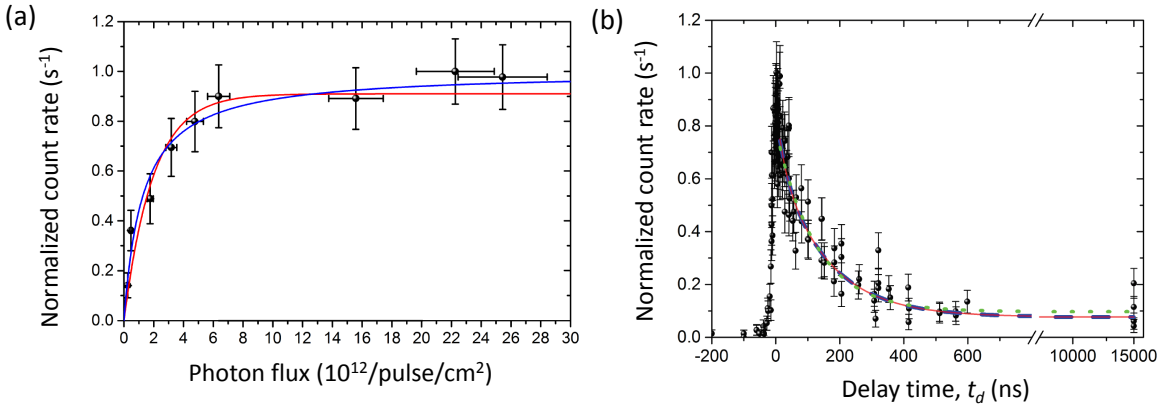

Figure 4.1: (a) Saturation and (b) delayed ionization curve of ^{254}No. The solid lines represent a fit from a two level scheme. The curves have been measured at 95 mbar pressure. Adopted from [25].

signal as a function of the delay time (t_d). At an argon gas pressure of 5 mbar the delayed ionization signal showed a fast decaying trend. The extracted lifetime of 5 ns is in agreement with the reported lifetime of the optically populated ^{1}P$_1$ state [92, 93, 94].

When the buffer gas pressure inside the optical-cell was increased to 100 mbar, as required for the RADRIS experiments, it was observed that the delayed ionization decreases rapidly for about the first 25 ns and then decreases slowly with increasing delay time (t_d). Figure 4.3 (b) shows the observed signal for delayed ionization in this case. The persistence of the RIS signal at delay time as large as 1 μs suggests that the optically excited ^{1}P$_1$ state undergoes a fast quenching, due to collisions with the buffer gas, to low-lying long-lived excited states. This implies that a simple 2-level system cannot fully describe the delayed ionization behaviour and a multi-level system is necessary for accurate determination of the parameters of the optical transition.

Quenching of atomic levels in noble gas environment has also been reported in atomic barium by Burst and Gallagher [95] and for calcium by Pence and Leone [96]. With the laser pulse length of about 18 ns applied in our experiment, a lower limit for the de-excitation rate of the singlet P state in Yb at 100 mbar argon on the order of 10^8 s^{-1} can be estimated. This rate is rather large for collisions with a noble gas compared to the one for barium where the energy difference to lower-lying metastable states are in the order of 1000 cm^{-1} [95]. Since the collisional cross-section is inversely proportional to the energy difference between the atomic levels, as discussed by Krause for the fine-structure levels of alkali elements [97], the optically excited ^{1}P$_1$ state should relax to states which are close in energy such as the ^{3}D$_2$ state in Yb, which is energetically located 316 cm^{-1} below the ^{1}P$_1$ state [90, 91].

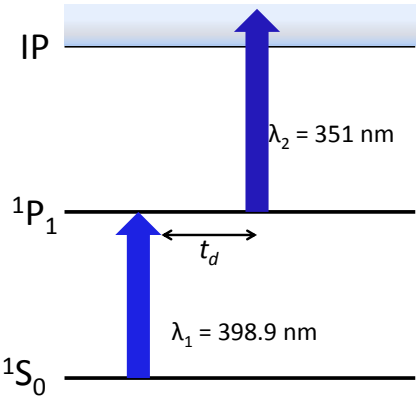

Figure 4.2: Schematic illustration of the two-step ionization scheme for Yb with a non-resonant second step, which can temporally be delayed by the delay time t_d with respect to the first step.

In order to determine the levels which are involved in the quenching process, RIS measurements were performed involving Rydberg states excited from the intermediate states in ^{nat}Yb. A dye laser with excalite-398 dye, was operated at 398.9 nm exciting the $^1P_1$ state. A second tunable dye laser was used to scan for Rydberg states. The measurements were performed at an argon buffer gas pressure of 100 mbar. Figure 4.4 (a) shows the obtained spectrum when both laser pulses are synchronized to arrive simultaneously at the optical gas cell. Members of at least two Rydberg series were observed along with some states, marked in red in figure 4.4 (a), which proceeded from another state populated by gas induced quenching of the $^1P_1$ state. The most prominent series observed agrees with reported Rydberg series belonging to s- and d-series [98], which can be directly excited from the $^1P_1$ level, populated by the first excitation step. When the second step laser pulse was delayed by 60 ns, the first series vanishes as expected from the short lifetime of this state. Nevertheless, another Rydberg series proceeding from an intermediate state becomes prominent as seen in figure 4.4 (b). The convergence of the Rydberg states can be extracted using the Rydberg-Ritz formula (equation 2.33).

The convergence of the two series differ by 316 cm^{-1} which leads to the conclusion that the latter Rydberg series proceed from the $^3D_2$ state. Further Rydberg states proceeding from the lower-lying $^3D_1$ state, which is 579 cm^{-1} below the $^1P_1$ state, were also observed, but were at least a factor 100 lower in intensity. Investigations on the lifetimes of these intermediate states were performed at a gas pressure of 100 mbar. For this the first step was operated at $\bar{\nu}_1 = 25068.22$ cm^{-1}. The second step was set to excite specific Rydberg peaks at $\bar{\nu}_2 = 25188.4$ cm^{-1}, excited from the $^1P_1$ and $\bar{\nu}_2 = 25198.4$ cm^{-1}, which is excited from the $^3D_2$. Figure 4.5a and 4.5b show the observed ion signal from the delayed ionization

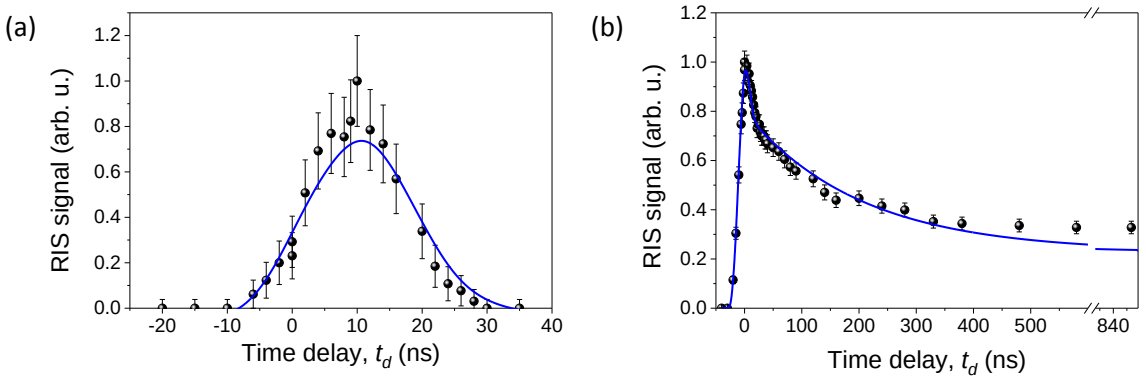

Figure 4.3: Ion signal for a two-step ionization scheme of ^{nat}Yb with a non-resonant second step as a function of different laser pulse delays at (a) 5 mbar and at (b) 100 mbar argon gas pressures. The solid lines represent best fits to the data using the 5-level rate equation model.

of the $^1P_1$ and $^3D_2$, respectively. The lifetime of $\tau = 5.8 \pm 0.7$ ns was extracted from an exponential fit to the data for the $^1P_1$ and is in good agreement with the literature value of 5 ns [92, 93, 94]. However, for the $^3D_2$ level the extracted lifetime of 154 ns is significantly shorter than the reported value of 460 ns [92, 93, 94], indicating that a subsequent quenching of the population of this state to energetically lower states is present. The long tail seen in figure 4.3 (b) for a delayed non-resonant second ionization step is traced back to indirectly (via collisional quenching) populated and long-lived intermediate states that are energetically close to the $^1P_1$ state and thus still contributing to the RIS signal.

4.2 Multi-level rate equation model

In order to extract the optical properties of the observed transition in nobelium, a multi-level rate model was developed. This model was first validated using the ground state transition on the homologue element ytterbium before extending it to nobelium using suitable fit parameters. Besides the short-lived $^1P_1$ state, additional atomic states featuring long lifetimes, such as $^3D_2$, the $^3P_2$ state or the $4f^{13}5d_{3/2}6s^2$ $J = 2-5$ states in Yb, which serves as collecting states for the population from gas induced collisional de-excitation of higher lying levels need to be considered. From the arguments presented in the previous section, an effective 5-level-scheme, consisting of the ground state ($|1\rangle$), three intermediate states($|2\rangle$, $|3\rangle$, $|4\rangle$) and an ionic state ($|5\rangle$), would be sufficient to describe the experimental observations, see figure 4.6.

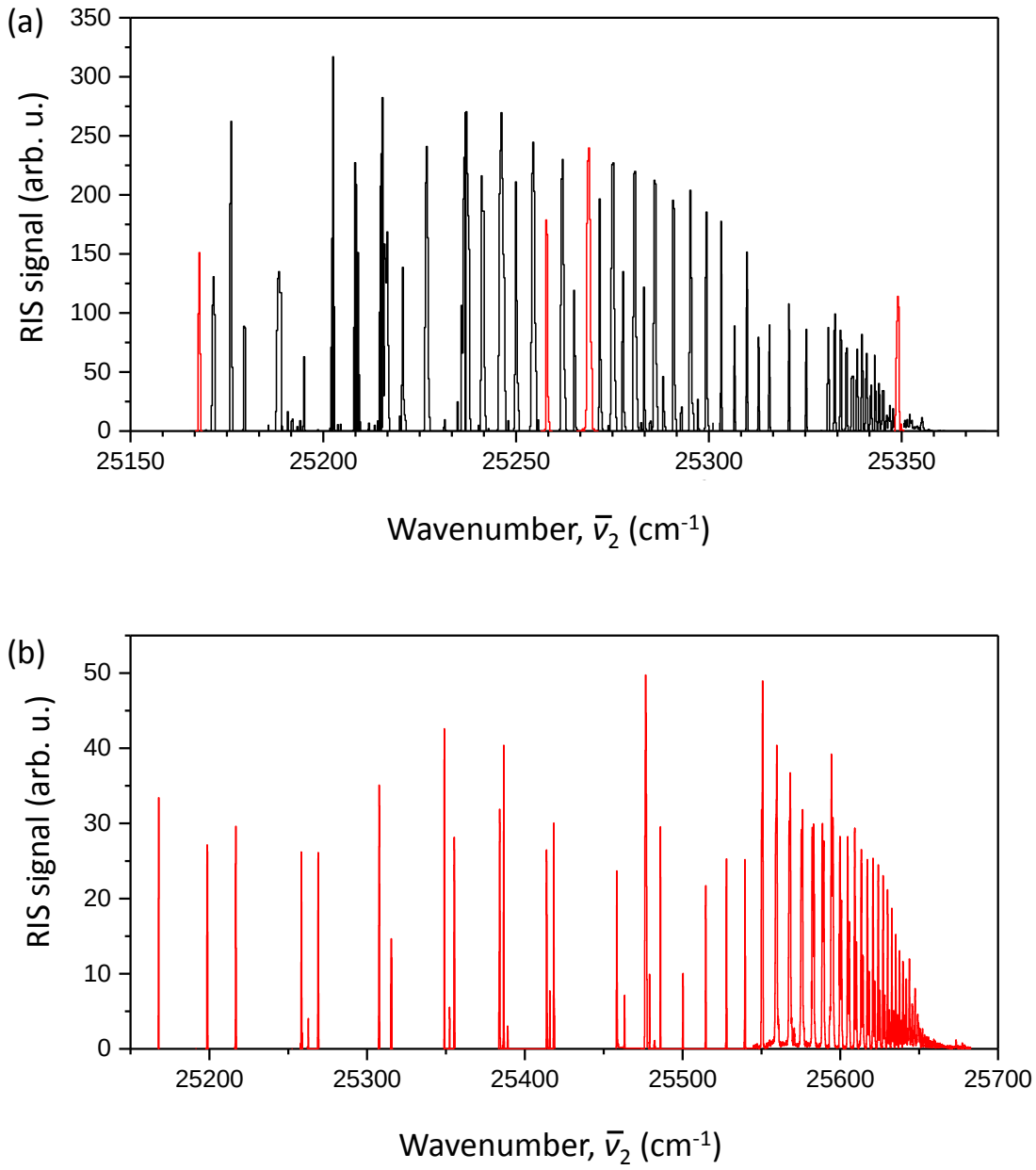

Figure 4.4: Rydberg states in Yb (a) for prompt ionization, i.e. $t_d = 0$ ns (b) with $t_d = 60$ ns delay between the two laser steps. The measurements were performed at 100 mbar argon pressure with the laser power of about 300 μJ for both lasers. For the prompt ionization, members of two Rydberg series were observed (marked in two different colours).

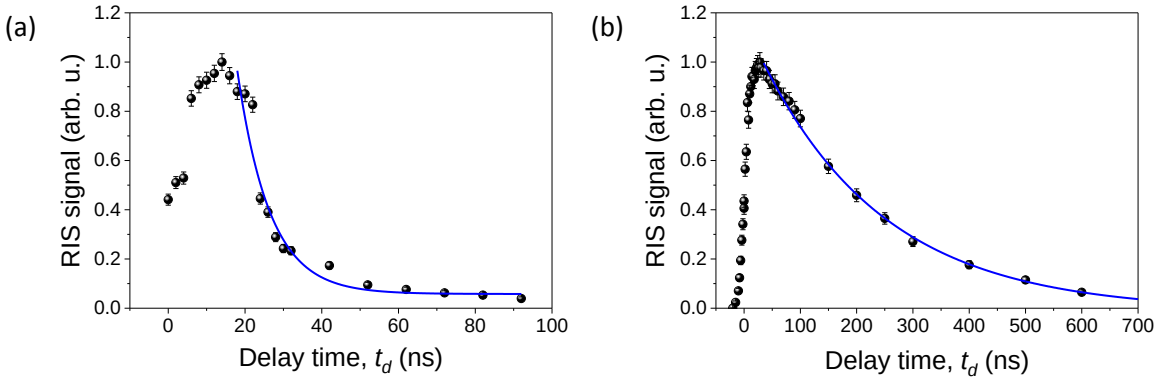

Figure 4.5: Ion signal for a two-step ionization scheme of $^{\mathrm{nat}}$Yb with a resonant second step as a function of different laser pulse delays at (a) 5 mbar and (b) 100 mbar argon pressure. The solid line indicates an exponential fit to the data.

Considering the broadband laser pulse, with a bandwidth of 5.5 GHz (FWHM), and large collisional broadening due to the high buffer gas pressure in our experiment, the off-diagonal elements or coherences, in the optical Bloch equation, equation 2.30, can be neglected [47], and an effective rate equation model can be formulated as

$$\begin{aligned}
&\frac{d\rho_{11}}{dt} + \frac{1}{2}(\rho_{11}-\rho_{22})A_{ki}S(\omega_L,\omega_{12})f_1(t) = A_{ki}\rho_{22} \\
&\frac{d\rho_{22}}{dt} + \left[A_{ki}+R_2+P_2f_2(t-t_d)\right]\rho_{22} = \\
&\qquad\qquad \frac{1}{2}(\rho_{11}-\rho_{22})A_{ki}S(\omega_L,\omega_{12})f_1(t) + R_4\rho_{44} \\
&\frac{d\rho_{33}}{dt} = (P_2\rho_{22}+P_4\rho_{44}+P_5\rho_{55})f_2(t-t_d) \\
&\frac{d\rho_{44}}{dt} + \left[R'+R_4+P_4f_2(t-t_d)\right]\rho_{44} = R_2\rho_{22} \\
&\frac{d\rho_{55}}{dt} + P_5f_2(t-t_d)\rho_{55} = R'\rho_{44}
\end{aligned} \tag{4.1}$$

with the normalization

$$\sum_i \rho_{ii} = 1 \tag{4.2}$$

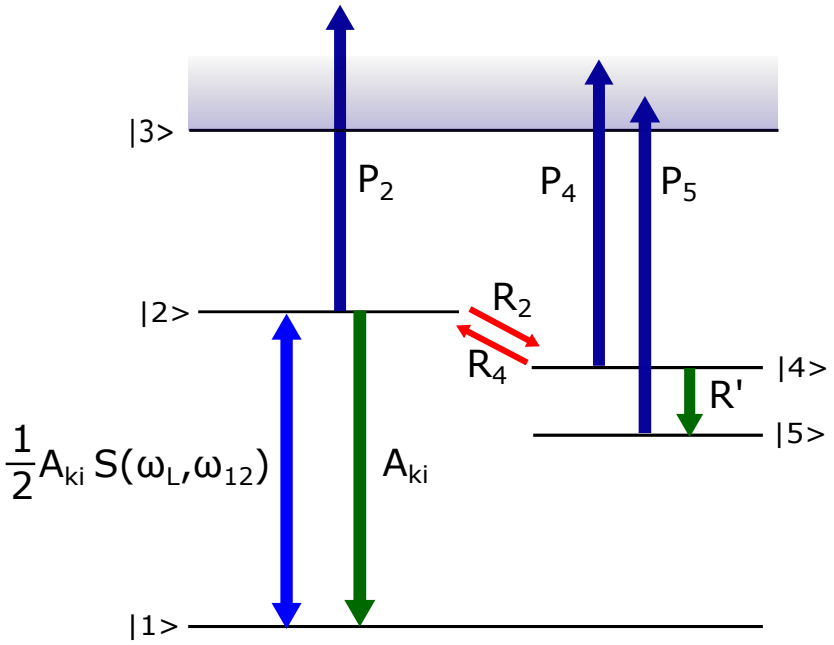

Figure 4.6: A level scheme with radiative and non-radiative processes used in the 5-level rate equation model developed to describe the experimental data.

and the initial conditions

$$\rho_{11}(t=0) = 1 \text{ and } \rho_{ii}(t=0) = 0 \text{ for } 1 < i. \tag{4.3}$$

Here ρ_{ii}, with i=1-5, corresponds to the population of individual states $|i\rangle$, A_{ki} is the Einstein coefficient for spontaneous emission for the $^1P_1 \rightarrow {}^1S_0$ transition. The Einstein coefficient is related to the radiative lifetime τ_{ki} of the excited state by $A_{ki} = \frac{1}{\tau_{ki}}$. $R_{2,4}$ are the gas induced transfer rate from the optically excited state to the lower-lying intermediate state and back to the optically excited state, respectively. R' is the effective transfer rate from state $|4\rangle$ to the long-lived state $|5\rangle$, where the population transfer is composed of optical decay as well as from gas collisions. $f_1(t)$ and $f_2(t-t_d)$ are functions describing laser pulse shapes for the first- and second-excitation step, respectively. t_d is the delay time of the ionizing laser pulse with respect to the first-excitation step. The ionizing rates P_j from the intermediate states to the continuum are defined as [99]

$$P_j = \frac{E_2/A_2}{t_2 \hbar \omega_2} \sigma_j \quad \text{with j = 2,4,5} \tag{4.4}$$

where E_2/A_2 is the laser pulse energy of the second-step per unit area, t_2 the corresponding laser pulse duration, $\hbar$ the reduced Planck constant, ω_2 the angular frequency of the ionizing laser and σ_j the ionization cross-section which is in the order of $10^{-16}\,\mathrm{cm}^2$. The frequency dependent saturation parameter $S(\omega_L, \omega_{12})$ is given by [47]

$$S(\omega_L, \omega_{12}) = \frac{\lambda_1^2}{2}\frac{E_1/A_1}{t_1\hbar\omega_{12}}\int \frac{1}{\sqrt{2\pi}\sigma_\omega}\exp\Big[-\frac{(\omega-\omega_L)^2}{2\sigma_\omega^2}\Big]\frac{\gamma_\omega^{'}/2\pi}{(\omega-\omega_{12})^2+(\gamma_\omega^{'})^2/4}d\omega. \quad (4.5)$$

E_1/A_1 is the first excitation step laser pulse energy per unit area with the corresponding wavelength λ_1. t_1 is the laser pulse duration and ω_{12} is the resonance frequency of the first excitation step. The spectral distribution is described as a convolution of a Gaussian profile with a Lorentz profile. The spectral laser profile (σ_L) and the Doppler broadening (σ_D) contribute to the Gaussian part according to

$$\sigma_w^2 = \sigma_L^2 + \sigma_D^2 \quad (4.6)$$

centred around the laser frequency ω_L. The Einstein coefficient A_{ki} of the optical transition, the dephasing (τ_{coll}) due to collision and the dephasing due to the phase fluctuations of different laser modes (τ_{mode}) contribute to the Lorentz part of the width $\gamma_\omega^{'}$ according to

$$\gamma_\omega^{'} = \frac{1}{2\pi}\Big(A_{ki} + \frac{1}{\tau_{\mathrm{coll}}} + \frac{1}{\tau_{\mathrm{mode}}}\Big). \quad (4.7)$$

These rate equations were solved by integrating over the duration of the laser pulses while varying the first step laser frequency or photon fluxes. The data for the resonance spectrum and the saturation of the ground state optical transition were fitted using a χ^2 minimization algorithm, implemented in the minuit package of the root evaluation software [100].

4.3 Experiments on ytterbium

The model described in the previous section (Eq. 4.1) was tested for validation with $^{\mathrm{nat}}$Yb data. Besides the signal of the delayed ionization, shown in figure 4.3, the resonance of the first excited level was measured as a function of the excitation wavelength. In addition, the signal strength as a function of the photon flux in the first excitation step was tested with this model as well. The excited atom was assumed to undergo nonresonant ionization. The fit parameters were extracted using the delayed ionization measurement of the $^1\mathrm{S}_0 \rightarrow {}^1\mathrm{P}_1$

ground state transition. Figure 4.3 shows the delayed ionization signal with the solid lines representing the best fit of the data according to the rate equation model. The Doppler broadening (σ_D) can be calculated from the gas temperature [101]

$$\sigma_D = c\bar{\nu}\sqrt{\frac{k_B T}{Mc^2}} = 9.118 \times 10^3 \bar{\nu}(\mathrm{cm}^{-1})\sqrt{\frac{T(K)}{A}}\ \mathrm{GHz} \tag{4.8}$$

with $\bar{\nu}_1 = 25068.22\,\mathrm{cm}^{-1}$ and $A = 173$, the Doppler broadening is deduced to be $\sigma_D = 0.297\,\mathrm{GHz}$ at room temperature, and is similar for both, nobelium and ytterbium. The laser bandwidth was measured to be $\sigma_L = 2.5\,\mathrm{GHz}$ resulting in a Gaussian width of $\sigma_\omega = 2.5\,\mathrm{GHz}$. The dephasing due to collisions (τ_{coll}) can be calculated from the collision rate in 100 mbar argon gas by [47]

$$\frac{1}{\tau_{\mathrm{coll}}} = \sigma_{\mathrm{coll}} N \bar{v} = \sigma_{\mathrm{coll}} N c \sqrt{\frac{8kT}{\pi m_{Ar} c^2}}\ \mathrm{GHz} \tag{4.9}$$

The collisional cross-section σ_{coll} is taken as $1 \times 10^{-13}\,\mathrm{cm}^2$, N is the density of gas at 100 mbar, m_{Ar} is the mass of argon atoms, $\bar{v}$ is the mean velocity of the argon atoms and c is the speed of light. N can be calculated using the ideal gas law where at standard temperature and pressure, one mol (6.022×10^{23} atoms) occupies a volume of $22400\,\mathrm{cm}^3$. Thus, N can be scaled to 100 mbar by

$$N = \frac{6.022 \times 10^{23}}{22400\ \mathrm{cm}^3} \times \frac{100\ \mathrm{mbar}}{1014\ \mathrm{mbar}}. \tag{4.10}$$

The time scale for fluctuations of the laser modes ($\tau_{\mathrm{mode}} = \frac{1}{9\times10^9\ \mathrm{GHz}}$) is taken similar to that for fermium [102]. The gas induced quenching rate (R_2) from the optically excited $^1\mathrm{P}_1$ state to the closest $^3\mathrm{D}_2$ state is deduced from the best fit of the rate equation model on the delayed ionization data of Yb shown in figure 4.3b to be $R_2 = 0.08 \times 10^9\,\mathrm{s}^{-1}$. The back pumping rate (R_4) is assumed to be negligibly small. The combined quenching and optical decay rate of the $^3\mathrm{D}_2$ level to the lower lying long-lived state (R') is more than one order of magnitude weaker. This is also reflected in the extended lifetime measurements, observed in the Rydberg level excitation, figure 4.5b. Thus, R' is taken as $R' = 0.006 \times 10^9\,\mathrm{s}^{-1}$. The ionization rates from the $^1\mathrm{P}_1$ and the $^3\mathrm{D}_2$ (P_2 and P_4) state are assumed to be identical as these states are close in energy and since the ionization process is non-resonant. These rates amount to $P_2 = P_4 = 0.05 \times 10^9\,\mathrm{s}^{-1}$. The ionization rate of the longest-lived state (P_5) is assumed to be one order of magnitude smaller $P_5 = 0.003 \times 10^9\,\mathrm{s}^{-1}$. Since the ionizing laser radiation (λ_2) is much closer to the ionization potential, it seems unexpected that P_5 is

Table 4.1: Parameters taken as constants, that were used to fit the data

Parameter	No	Yb	Unit
σ_ω	2.5	2.5	GHz
$\tau_{\text{coll}}{}^{-1}$	11	11	GHz
$\tau_{\text{mode}}{}^{-1}$	9	9	GHz
R'	0.01×10^9	0.006×10^9	s^{-1}
P_2	0.05×10^9	0.05×10^9	s^{-1}
P_4	0.05×10^9	0.05×10^9	s^{-1}
P_5	0.003×10^9	0.003×10^9	s^{-1}
R_2	0.3×10^9	0.08×10^9	s^{-1}
R_4	0	0	s^{-1}

smaller and hints to additional decays into dark, invisible states, from which no ionization with the second step is possible. In addition, small deviation at long delay time as seen in figure 4.3b suggests the influence of additional low-lying states.

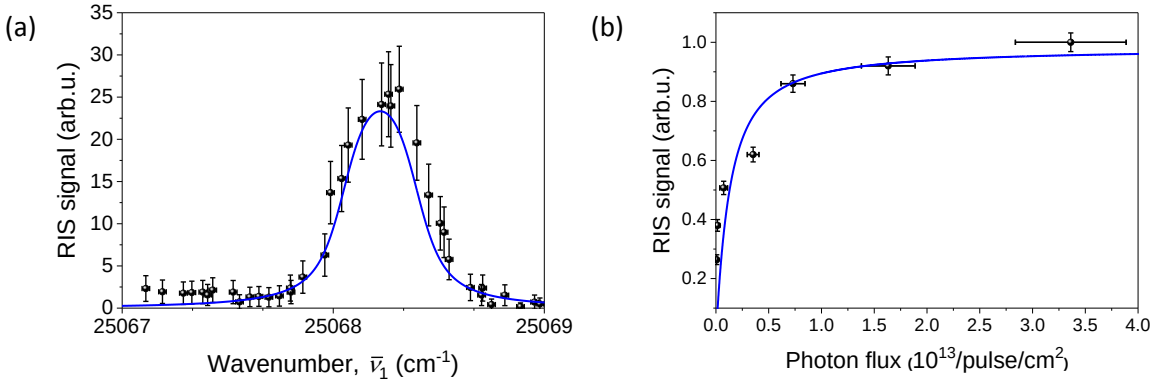

Figure 4.7: Resonance (a) and saturation character (b) of the $^1S_0 \rightarrow {}^1P_1$ transition in Yb. The measurements were performed at 100 mbar argon pressure. See text for more details. The solid lines indicate fits using the rate equation model to the data.

The fit parameters that were taken as constants are summarized in table 4.1. Using these parameters a fit was performed on the resonance and the saturation character of the $^1S_0 \rightarrow {}^1P_1$ transition in Yb in order to deduce the transition strength. Figure 4.7a shows the spectral profile of the resonance located at $\bar{\nu}_1 = 25068.22\,\text{cm}^{-1}$. The resonance was measured at a photon flux of 7×10^{12} photons/pulse/cm^2 for the first excitation step while the photon flux of the ionizing laser was 4.1×10^{14} photons/pulse/cm^2. The solid line is the fit from the rate equation model. For the measurement of the saturation character, the first excitation step was tuned to the resonance and the RIS signal was measured as a function of the laser power

of the excitation step. Figure 4.7b shows the saturation curve along with the best fit using the 5-level rate equation model. The obtained Einstein coefficient, $A_{ki} = 2.6 \pm 0.6 \times 10^8\,\mathrm{s}^{-1}$ is in a good agreement with the literature value of $A_{ki}{}^{\mathrm{lit}} = 1.9 \times 10^8\,\mathrm{s}^{-1}$ [92]. Considering an additional level below the state $|5\rangle$ in figure 4.6 did not have a significant impact on the fit results. Thus, a 5-level model is sufficient to describe all observations and enabled the extraction of relevant parameters for the optical transition of interest in ytterbium and in its heavier homologue nobelium.

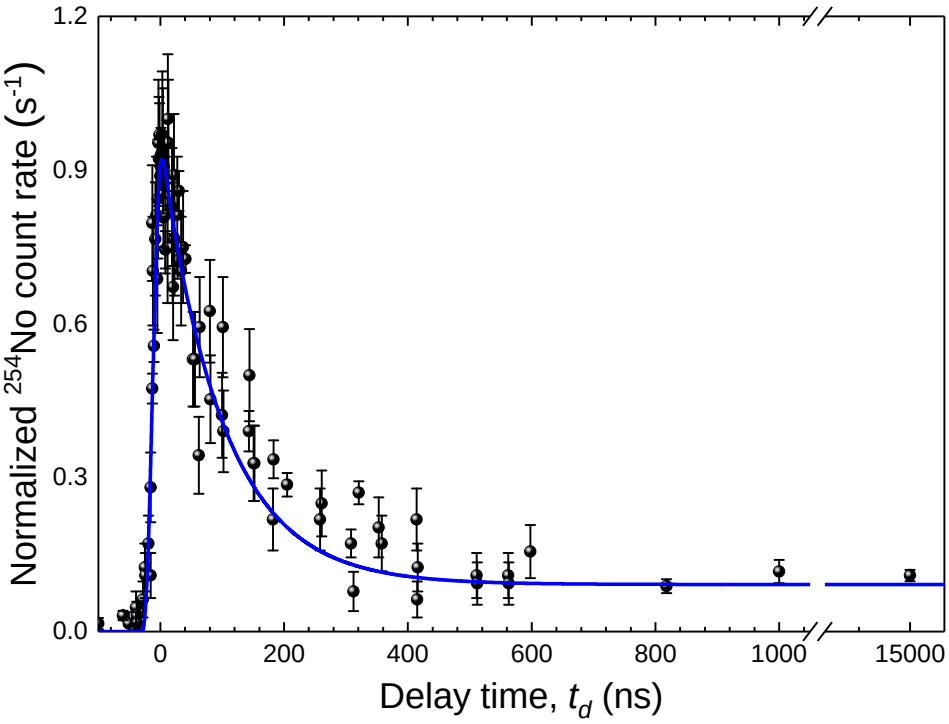

Figure 4.8: Normalized $\alpha-$decay rate as a function of the delay time t_d between the first- and the second-step excitations in ^{254}No. The solid line indicates the best fit to the data from the rate equation model.

4.4 Characterization of the ground-state atomic transition in ^{254}No

During the 2015 beamtime campaign, the $^1S_0 \rightarrow {}^1P_1$ ground state transition in ^{254}No was observed for the first time at GSI Helmholtzzentrum für Schwerionenforschung and has been reported in [24] and [25]. The production mechanism and the on-line experiment has been described in detail in chapter 3.1. The influence of the buffer gas quenching of the optically excited state became clear while measuring the RIS signal for a delayed non-resonant ionization as shown in figure 4.8. In this experiment the first excitation laser was tuned to the

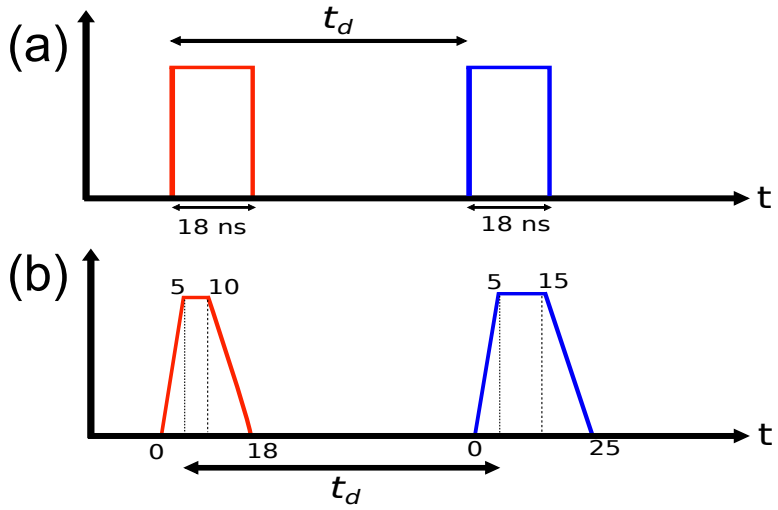

Figure 4.9: Laser pulse shapes considered for evaluation of the data.

resonance at $\bar{\nu}_1 = 29961.5\,\mathrm{cm}^{-1}$ while the ionizing step was provided by the excimer laser at 351 nm. The ^{254}No count rate was recorded as a function of the ionizing laser delay time (t_d), while keeping the laser power of both the excitation step as well as the ionizing step constant. A RIS signal component that exponentially decreases with a lifetime on the order of 100 ns is visible, which was much larger than the predicted lifetime of 2-3 ns [35, 39, 89] for the ^{1}P$_1$ state and is in disagreement with the saturation characteristics discussed in [25]. Similar to the case of Yb, there are also contributions from levels with much longer lifetimes. The absence of a component with a short decay time indicates a much stronger quenching compared to Yb, and one may infer that the corresponding level where the population is transferred is closer in energy. This is supported by atomic calculations predicting a ^{3}D$_3$ state to be energetically slightly below the ^{1}P$_1$ state in No [39, 43]. In order to mimic the temporal laser pulse shape in our experiment, various shapes like rectangular as well as trapezoidal as seen in figure 4.9, were used to get a best fit of the delayed ionization signal. While both shapes give similar results for the Einstein coefficient, the trapezoidal shape mimicked the delayed ionization signal better. The solid line in figure 4.8 represents the best fit of the rate equation model to the data with the parameters listed in table 4.1.

The observed resonance for the first excited step centred at $\bar{\nu}_1 = 29961.457^{+01041}_{-0.007}\,\mathrm{cm}^{-1}$ can be seen in figure 4.10a. The number of resonant ions per second detected by the $\alpha-$detector is given as a function of laser frequency. The count rate has been normalized to a beam current of one particle microampere, equivalent to 6.2×10^{12} ^{48}Ca projectiles per second. The best fit to the data is indicated by the solid line. The measurements were performed with an intra cavity etalon inserted into the resonator of the dye laser in order to reduce the bandwidth of the laser light to 1.2 GHz (FWHM). This gives the laser bandwidth

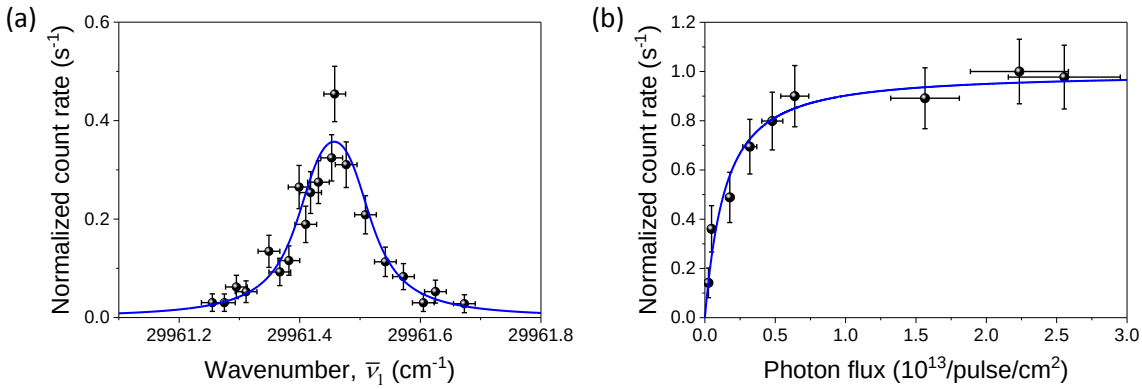

Figure 4.10: (a) Spectral profile of the $^1P_1$ state in ^{254}No. The full-width at half-maximum (FWHM) of the fitted profile is about 0.13 cm^{-1}, photon flux, 5.2×10^{12} photons per pulse per square centimetre; laser bandwidth, 0.04 cm^{-1}. (b) Saturation character of the $^1S_0 \rightarrow ^1P_1$ transition in ^{254}No with the best fit from the rate equation model. In this case the laser bandwidth was about 0.18 cm^{-1}. The solid lines indicate the best fit of the rate equation model to the data. In both cases the measurements were performed at 95 mbar argon pressure.

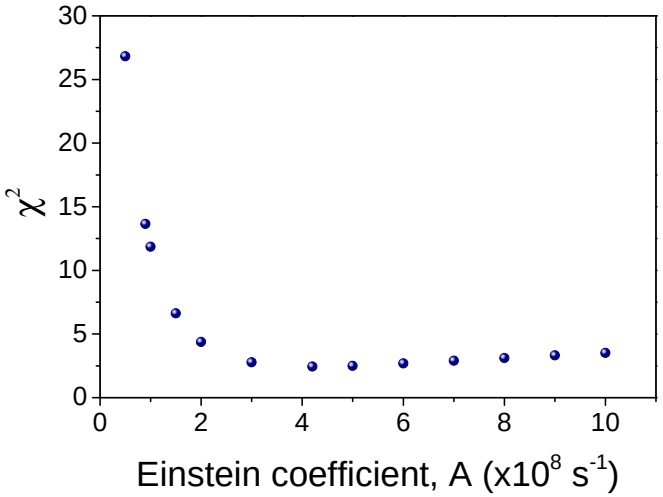

Figure 4.11: χ^2 values obtained by solving Eq. 4.1 for different values of the Einstein coefficient, A_{ki}, while fitting the saturation curve.

contribution to the linewidth of, σ_L =1.2 GHz/2.355=0.51 GHz. With a Doppler broadening of $\sigma_D = 0.297$ GHz from table 4.1, the Gaussian width amounts to

$$\sigma_\omega = \sqrt{\sigma_D^2 + \sigma_L^2} = \sqrt{0.51^2 + 0.297^2} = 0.6\,\text{GHz}.$$

The contribution to the Lorentz width due to the dephasing of the different laser modes is taken as $\tau_{\text{mode}} = 0$ as we assume the laser to be single mode during a narrow band operation. According to the best fit to the data the Einstein coefficient (A_{ki}) and the collisional dephasing (τ_{coll}) result in a Lorentz width of

$$\gamma_{\omega}^{'} = \frac{1}{2\pi}(A_{ki} + \frac{1}{\tau_{\text{coll}}}) = 1.8\,\text{GHz}.$$

For the saturation curve measurement, the first excitation step was kept at resonance at $\bar{\nu}_1 = 29961.5\,\text{cm}^{-1}$ and the $\alpha-$decay count rate was measured as a function of the laser power of this step. During all the measurements, the photon flux of the ionizing step was around 7.3×10^{15} photons/pulse/cm^2, which was well above the saturation for the ionizing step [25]. Since the measurements of the laser power and the laser spot size determination are prone to errors, so in order to account for systematic uncertainties, the saturation behaviour data was also evaluated with a conservative estimate of a 20% increase/decrease in the photon flux. Different laser temporal pulse shapes as shown in figure 4.9 were also considered. The fit was performed for the Einstein coefficient, A_{ki} leading to an $A_{ki} = 4.2^{+2.6}_{-2.8} \times 10^8\,\text{s}^{-1}$. The rate equation model, equation 4.1, was fitted with different values of A_{ki}, and the resulting χ^2 values shows an asymmetric confidence band for the fit. Figure 4.11 shows the χ^2 values plotted against the Einstein coefficient, A_{ki}. This leads to the conclusion that the large uncertainty results from a lower sensitivity of the model for values $A_{ki} > 2 \times 10^8\,\text{s}^{-1}$ expressed in a moderate increase of the χ^2 value for larger Einstein coefficients. Nevertheless the steep increase of the χ^2 value for $A_{ki} \leq 1 \times 10^8\,\text{s}^{-1}$ clearly shows that the observed transition in nobelium is strong, which supports the assignment of the observed transition as $^1\text{S}_0 \rightarrow {}^1\text{P}_1$ ground state transition in nobelium.

5 Rydberg states and the first ionization potential of nobelium

The first ionization potential (IP) of a chemical element, defined as the energy required to remove the most weakly bound electron from the valence shell, is a fundamental quantity that determines the chemical properties of an element. An accurate determination of the IP therefore provides a crucial test for our understanding of the electron configuration and the chemical properties of an element. In the region of the actinide elements [103], different methods such as resonance ionization mass spectroscopy, Rydberg convergence and surface ionization techniques have been used to determine the IP [104, 105, 106, 107, 108, 109, 110, 22]. For the actinides from actinium (Ac, $Z = 89$) to einsteinium (Es, $Z = 99$) the IP was measured with laser spectroscopic techniques with a precision in the μeV-regime. In the case of fermium (Fm, $Z = 100$), only an upper limit of the IP has been reported [22]. The IP of the heaviest actinide lawrencium (Lr, $Z = 103$) was measured with a surface ionization technique. An uncertainty of about 100 meV, which is susceptible to unknown systematic effects was reported in [104]. In contrast, laser spectroscopy provides the most accurate method of determining the IP of an element with a precision in the μeV-regime. However, any atomic spectroscopy of the heaviest elements is hampered by a lack of known atomic transitions and drastically decreasing production rates from nuclear fusion reactions. During a beamtime in 2015, the $^1S_0 \rightarrow ^1P_1$ optical transition in nobelium was observed and has been reported in references [24, 25]. This enabled the search for Rydberg states near the ionization threshold and the extraction of the first ionization potential of nobelium via the Rydberg series convergence. This chapter presents the measurements on the Rydberg states and the precise extraction of the IP of nobelium.

5.1 The search for Rydberg states

A two-step photoionization technique was used to search for Rydberg states in ^{254}No. The first step was fixed to excite the $^1P_1$ state at $\bar{\nu}_1 = 29961.457\,\mathrm{cm}^{-1}$ in nobelium [24]. A second synchronised tunable dye laser was used to search for Rydberg states proceeding from the $^1P_1$ state. A simple excitation scheme is presented in figure 5.1. The atoms that were successfully excited to a Rydberg state were subsequently ionized either by residual

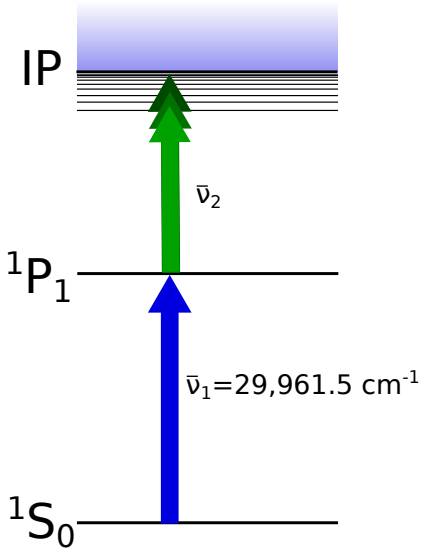

Figure 5.1: Two-step excitation scheme for the search for Rydberg states in nobelium.

laser light, infrared radiation or collisional processes. The second step was scanned in a spectral range of $23,000 - 23,700$ cm^{-1} using the laser dyes Coumarin 120 and Stilbene 3 pumped by excimer laser light at 308 nm wavelength. These dyes provide a conversion efficiency of about 15% [112, 113]. The dye lasers had an average pulse intensity of 50 μJ and 300 μJ for the first and second excitation step, respectively. The scans for Rydberg states were performed with a spectral step size of 0.2 cm^{-1}, with a measurement time of 600 s per scan step and a waiting time of 120 s (2 half-lives) between every step. At a buffer gas pressure of 95 mbar argon 22 levels were observed, which were assigned to two different Rydberg series (series 1 and 2). See figure 5.2 top panel. Some of these states have been reported in [24] together with a first evaluation for the first ionization potential. Nevertheless some indications on buffer gas-induced population transfer limited the precision for the IP value [24]. In order to reduce the buffer gas quenching of the optically excited $^1P_1$ state, the buffer gas pressure inside the gas cell was reduced to 65 mbar. With these settings an additional series (series 3) was observed with a substantially reduced count-rate (figure 5.2 lower panel). This reduction in the count-rate is attributed to competing processes such as quenching and optical de-excitation of the population of the $^1P_1$ state in addition to signal losses due to temporal mismatch between laser pulses of 18 ns duration and 11 ns jitter, as the lifetime of the $^1P_1$ state is only about 2 ns. The low-lying Rydberg states of this series showed a resolved multiplet structure (figure 5.3b). This splitting is attributed to different fine structure components. The splitting of the multiplets decreased with increasing principal quantum number (n).

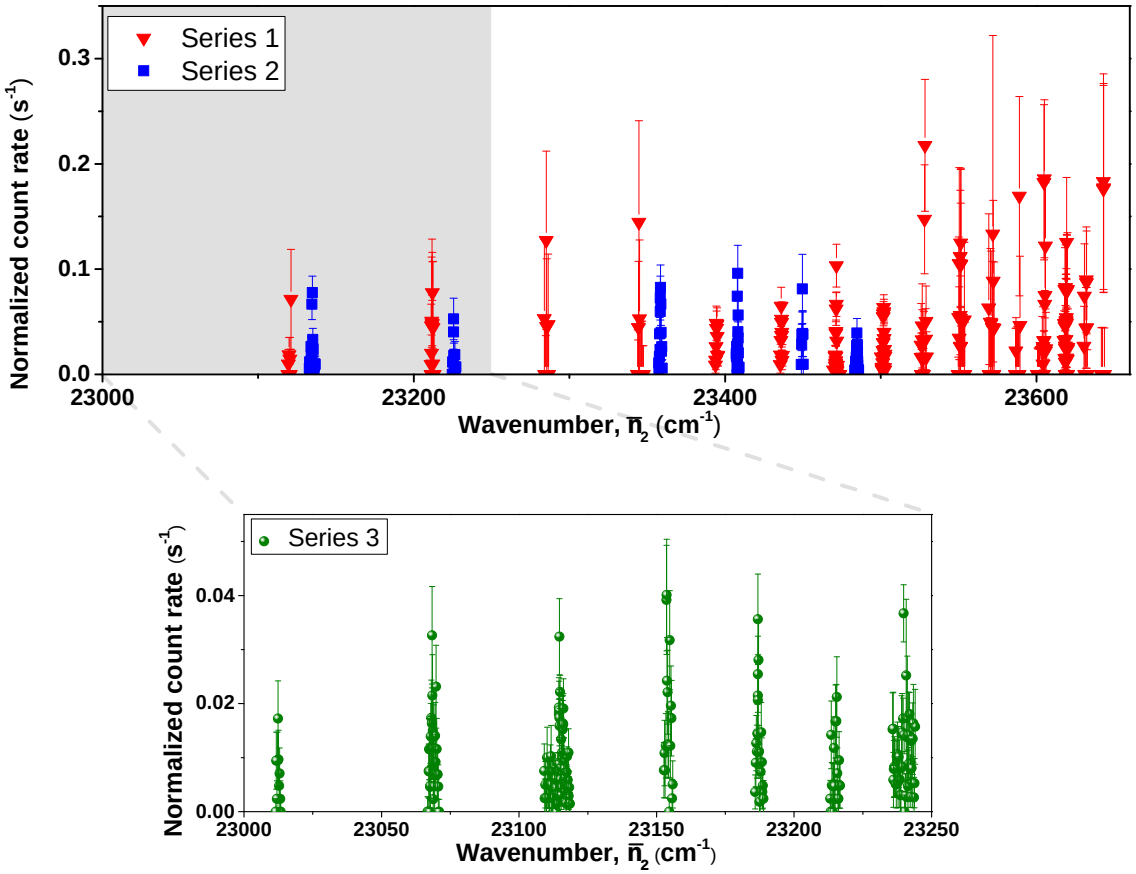

Figure 5.2: Observed Rydberg states of ^{254}No. Series 1 and 2 were measured at an argon gas pressure of 95 mbar while series 3 at a reduced pressure of 65 mbar, in order to reduce the buffer gas induced quenching. The first excitation step was fixed at $\bar{\nu}_1 = 29961.5$ cm^{-1} to excite the ^{1}P$_1$ state in No [24]. Adapted form [30].

5.1.1 Lifetime of the intermediate states

In order to characterize the intermediate states, measurements with a delayed ionization were performed. The measurements allow probing the lifetimes of individual intermediate states. For this purpose, one laser excitation step was set to the resonance frequency of the ^{1}P$_1$ state at $\bar{\nu}_1 = 29961.5\,\mathrm{cm}^{-1}$. The second laser step was tuned to excite a specific Rydberg state with a user-defined delay with respect to the first step. The delay time between the laser pulses was measured with a precision of 1 ns using signals from fast photodiodes in conjunction with a multi-channel analyser (MCA) and a time-to-amplitude converter (TAC). Figure 5.4 shows the observed RIS signal as a function of the delay time. To measure the lifetime of the intermediate state from which series 1 proceeded, the Rydberg level with an excitation energy of $\bar{\nu}_2 = 23472\,\mathrm{cm}^{-1}$ was selected. This measurement revealed a lifetime

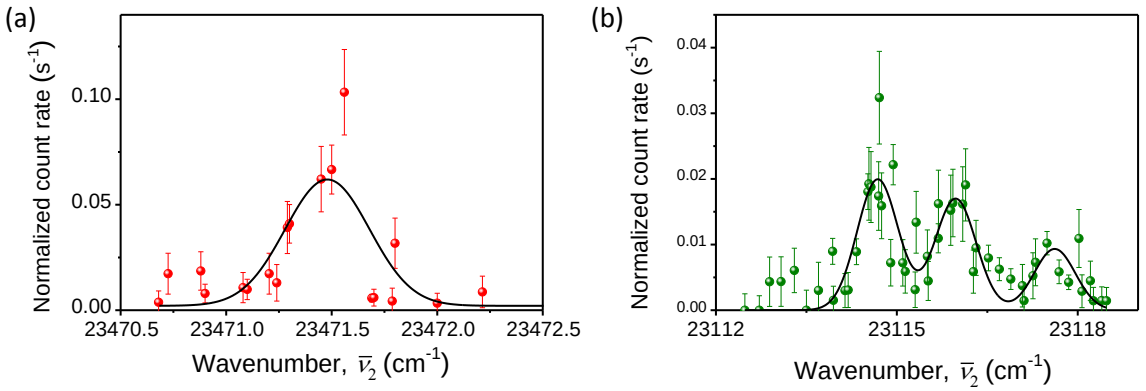

Figure 5.3: Two selected Rydberg states in ^{254}No proceeding from different intermediate states. The measurements were performed at 95 mbar argon pressure for (a) and at 65 mbar for (b). The solid lines are Gaussian fits to the peaks. The laser power was about 50 μJ per pulse for the first step and around 750 μJ per pulse for the second step.

of about (117 ± 18) ns (figure 5.4a) substantially longer than the expected life time of the $^1P_1$ state [36, 39, 89, 24]. In order to extract the lifetime of the state, a fit was performed using the rate equation model, described in chapter 4. The parameters used in the fit are given in table 4.1. The parameters P_2 and P_5 were used only for a non-resonant ionization scheme, and can be taken to be 0 as the ionization proceeds only from a Rydberg state. A similar measurement performed with series 2 also showed a comparable long lifetime for the intermediate state. This implies that both series 1 and 2, proceeded from intermediate state/states with similar lifetime.

For series 3, a Rydberg state located at $\bar{\nu}_2 = 23114.5\,\mathrm{cm}^{-1}$ was selected for the delayed ionization measurements. The intermediate state features a short life time of about (8.5 ± 2.2) ns (figure 5.4b). Here, the fit was performed using an exponential decay function as the rate equation model did not give a good fit due to the large laser jitter of more than 20 ns. This was caused by the malfunction of the thyratron of the pump excimer laser. This jitter of the laser also causes the RIS signal to be reduced as the population of the state can decay down to the ground state via spontaneous emission or can be transferred to a nearby excited state via collisions with the buffer gas. The intermediate level with such a short lifetime is assigned to the $^1P_1$ state for which a lifetime of (2 ± 1) ns was extracted from the saturation characteristics of this transition [24, 28]. The fact that a slightly longer lifetime of 8.5 ns was extracted is attributed to the pulse width of the laser pulses of 18 ns and a large jitter of the laser pulses. This supports that two series (1 and 2) proceed from an intermediate state,

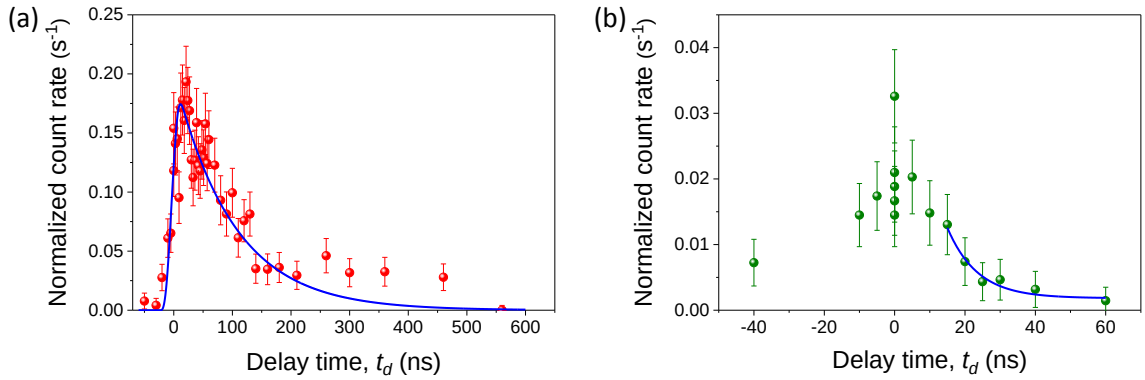

Figure 5.4: Measured RIS signal for delayed Rydberg excitation proceeding via the (a) $^3D_3$ and (b) $^1P_1$ intermediate state. The decay rate has been normalized to a beam current of 1 particle microampere. The measurements were performed at 95 mbar Ag for (a) and at 65 mbar for (b). The solid lines indicate fits using the rate equation model for (a) and an exponential decay function for(b) to the data. Considering the laser pulse width and the laser jitter, the exponential fit was only performed in the region where the count rate starts falling.

populated by buffer gas induced quenching from the $^1P_1$ state while the series 3 proceed from the $^1P_1$ state.

5.2 Pressure shift of the Rydberg states

The buffer gas environment influences the measured energy of the Rydberg states leading to a systematic error in the extracted IP. To quantify this shift detailed spectroscopic studies on the Rydberg states have been performed on ytterbium with natural isotopic composition (^{nat}Yb). Rydberg states with similar quantum numbers as those for No were excited at different pressures. The off-line set-up used for this purpose is described in detail in chapter 3.2. One dye laser was used to excite the $^1P_1$ state at $\bar{\nu}_1 = 25{,}068.22\,\mathrm{cm}^{-1}$ while a second laser scanned for the Rydberg states in a spectral range of 25,000-25,205 cm^{-1}. The measurements were performed at 6 different pressures ranging from 5 to 200 mbar. Figure 5.5 shows the observed Rydberg states as a function of the second-step wavenumber ($\bar{\nu}_2$) for two different pressures. The Rydberg states broaden and shift to lower energies with increasing gas pressure. The IPs were extracted for each pressure using the Rydberg-Ritz formula, equation 2.33. Plotting the extracted IP values as a of different pressure reveals a systematic shift to lower values of the ionization potential at higher gas pressures (see figure 5.6). The shift can be quantified by applying a linear fit to the data. The slope of the fit gives a pressure

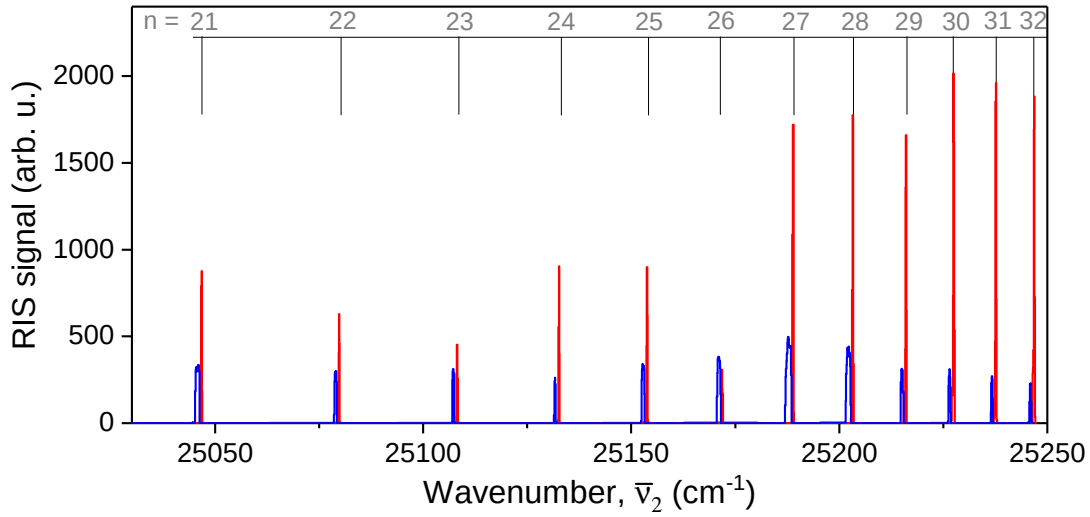

Figure 5.5: The measured Rydberg states in ^{nat}Yb at 5 mbar (red line) and 200 mbar (blue line). The laser power was 30 μJ per pulse for the first step and 300 μJ per pulse for the second step. Adapted form [80].

shift of the IP of -0.0060(7) cm^{-1} per mbar. The linear fit also allows the determination of the IP in vacuum (0 mbar) to be $E_{\mathrm{IP_{vac}}} = 50,443.35(10)$ cm^{-1}. This value agrees well with the literature value of 50,443.2(1) cm^{-1} [90]. These findings have been published in [80].

This result was used to estimate the systematic uncertainty for the on-line measurements for No where the measurements were performed at 95 mbar (series 1 and 3) and 65 mbar (series 3).

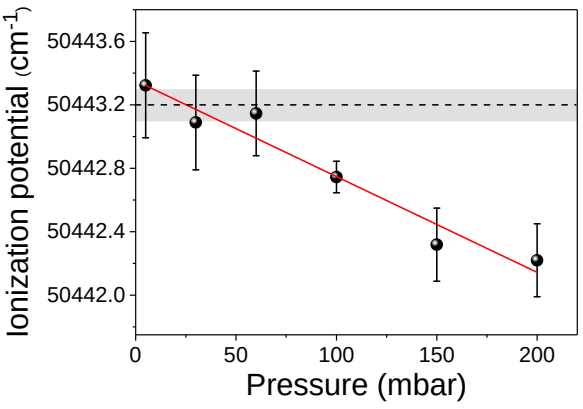

Figure 5.6: Extracted IP of Yb plotted as a function of argon pressure along with a linear fit to the data (solid line). Dotted line represents the literature value [90] for the IP with the error (shaded area). Adapted form [80].

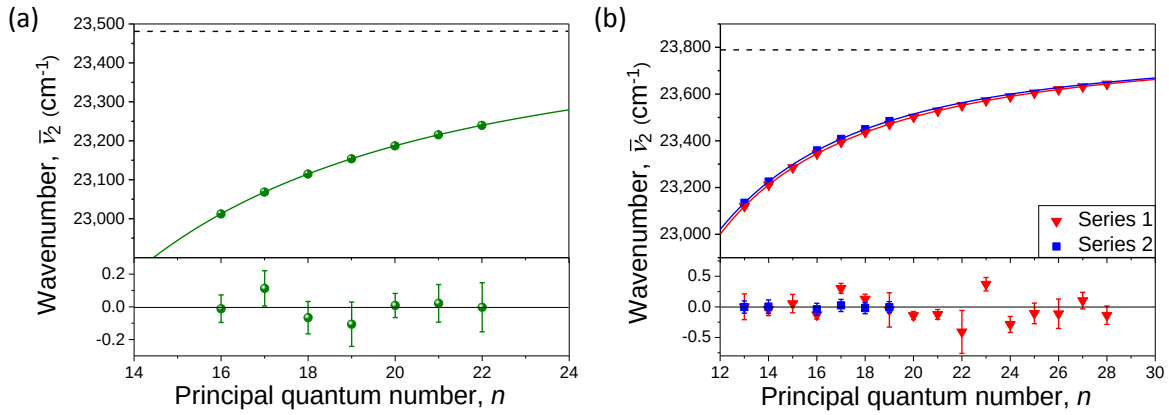

Figure 5.7: (a) Top panel: the position of Rydberg states proceeding from the $^1P_1$ state as a function of the principal quantum number n and a corresponding best fit (solid line) of the Rydberg-Ritz formula, equation 2.33. Lower panel: residuals of the fit. (b) Same, but for Rydberg states proceeding from the $^3D_3$ state.

5.3 Extraction of ionization potential of nobelium

It has been established in the previous section that the Rydberg states constituting of series 3 proceed from the $^1P_1$ state. The energetic position of these states can now be used to determine the ionization potential of nobelium. Single or multiple Gaussian fits were performed on every resolved and unresolved multiplet of this series to determine the excitation energies of the Rydberg states. Since in our experiment the band-head of the Rydberg series could be assigned, the principle quantum number n was assigned to each Rydberg state such that the quantum defect $\delta(n)$ ranges between 0 and 1. However, this choice of $\delta(n)$ does not affect the resulting convergence limits. Figure 5.3a shows the data as well as a best fit of the Rydberg-Ritz formula, equation 2.33, to the data resulting in a convergence limit

$$\bar{\nu}_2^{\lim} = (23482.14 \pm 0.27)\,\mathrm{cm}^{-1}.$$

This energy added to the excitation energy of the $^1P_1$ state, $\bar{\nu}_1 = 29961.457\,\mathrm{cm}^{-1}$, and correcting for the pressure shift, a value of the first ionization potential of $\mathrm{IP_{No}} = (53444.0 \pm 0.4)\,\mathrm{cm}^{-1}$ is derived, which corresponds to (6.62621 ± 0.00005) eV. The predicted value of the IP of nobelium using different theoretical models [39, 43, 114, 89, 115] along with the experimental value obtained in this work is given in table 5.1.

Table 5.1: Experimental and calculated values of the first IP of nobelium.

Method	IP (cm^{-1})	$^3D_3$ (cm^{-1})
Experiment (this work) [30]	53444.0 ± 0.4	29652^{+8}_{-1}
IHFSCC[39]	53489±800	29897±800
CI + all orders[114]	53738±500	30183±1100
MCDF[89]	53701±1100	
Extrapolation[115]	53600±600	

5.4 The $^3D_3$ state

The energy of the Rydberg states from series 1 and 2 were determined by fitting Gaussian profiles to the peaks. The series convergence was extracted using the Rydberg-Ritz fit, equation 2.33. The quantum defect, $\delta(n)$, can be characterized by the Ritz expansion, equation 2.34. In general, an expansion in first order is sufficient to describe the behaviour, the higher order corrections are only used to describe the polarization effects close to the core. Nevertheless, only for series 1 an expansion up to 3rd order had to be considered to obtain a reasonable fit to the data. In a combined fit of series 1 and 2 using equation 2.33 with a shared convergence limit, this limits amounts to:

$$\bar{\nu}_2^{\lim} = 23792.21^{+1}_{-8}\,\mathrm{cm}^{-1}.$$

The large uncertainty of -8 cm^{-1} reflects the change in the convergence limit depending on the number of higher order corrections of equation 2.34. The convergence limit of these series is about 310 cm^{-1} higher compared to the result obtained for the series 3. This leads to the conclusion that the series 1 and 2 proceed from an atomic state which is 310 cm^{-1} below the $^1P_1$ state. Theoretical calculations predict a $^3D_3$ state 159 cm^{-1} [39] or 20 cm^{-1} [114] below the $^1P_1$ state. Thus, this newly identified level at an energy of 29651.5^{+8}_{-1} cm^{-1} is assigned a $^3D_3$ term as this is the only level predicted to be close in energy to the $^1P_1$ state. Other low-lying states are expected to be more than 1000 cm^{-1} below the $^1P_1$ state. This state is inaccessible by laser spectroscopy as the optical transition from the $^1S_0$ ground state to the $^3D_3$ state is forbidden. A comparison of the experimental value with the theoretical predictions is presented in table 5.1.

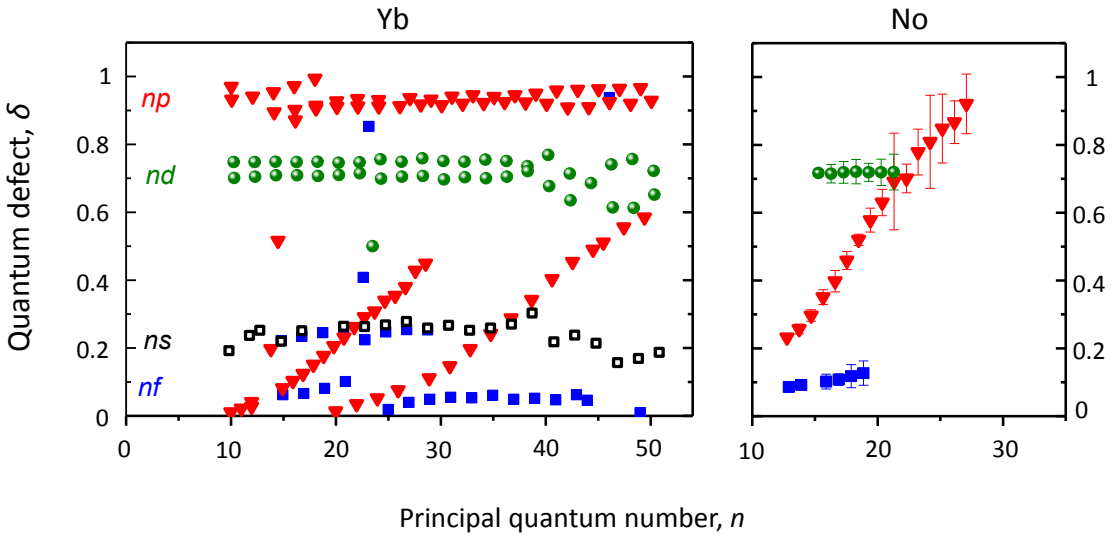

Figure 5.8: Left panel: Quantum defect ($\delta(n)$) for the Rydberg states in ytterbium as a function of the principal quantum number n. Right panel shows the $\delta(n)$ of the Rydberg states in No as a function of n. Adapted from [30].

5.4.1 Quantum defect analysis

To further characterize the individual Rydberg series, the quantum defect [116] of individual series was investigated. Figure 5.8 shows the values of the measured quantum defect ($\delta(n)$) in Yb and No as a function of their principal quantum number (n). The quantum defect values for Yb were extracted from the position of the Rydberg levels cited in [98, 117]. Series 1 and 2 in No have been assigned to a np and nf series as they have a similar $l-$dependent quantum defect constant δ_0 of 0.9 and 0.1 as in Yb, respectively. The quantum defect of series 1 shows a unique trend. This is probably due to the presence of high-lying perturbing orbitals which interfere with the Rydberg series. A similar behaviour was observed for the np series in Yb [117]. This trend can be treated perturbatively by using higher order corrections to the Ritz expansion, equation 2.34. Series 3 has a quantum defect $\delta_0 \approx 0.7$ similar to the nd series in Yb. Based on these values of δ_0, an assignment of nd is proposed for the series 3. These conclusions are in agreement with the findings from the lifetime measurements. Series 1 and 2 proceed via the long-lived D-state, which agrees with the selection rule for the angular momentum $\Delta L = \pm 1$, substantiating the assignment of the intermediate state.

In a more comprehensive picture, the optically excited $^1P_1$ state undergoes a gas-induced quenching to a lower intermediate state, $^3D_3$ state, located 310 cm^{-1} below the $^1P_1$ state at

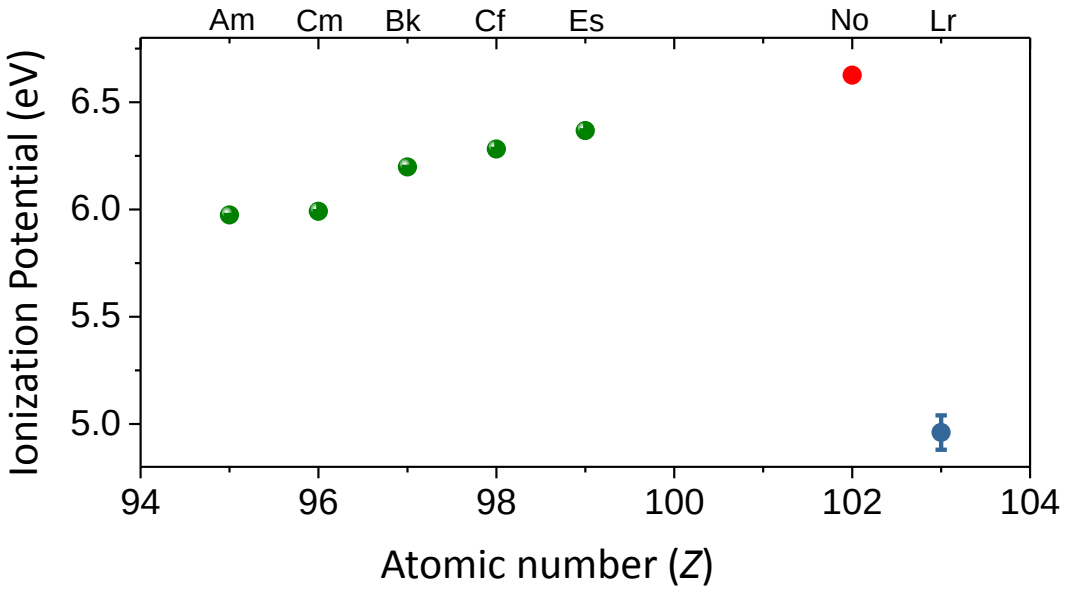

Figure 5.9: Experimental value of the ionization potential (IP) of actinides starting from americium (Am, $Z = 95$) up to lawrencium (Lr, $Z = 103$). The IP of nobelium measured in this work (red circle) is the highest for all the elements in the actinide series. All measurements were performed using laser spectroscopic techniques, except for lawrencium, hence the larger uncertainty.

$29652^{+8}_{-1}\,\mathrm{cm}^{-1}$. Rydberg excitation from both $^1\mathrm{P}_1$ as well as $^3\mathrm{D}_3$ state are possible, as was seen for the case of Yb, see chapter 4. The series 1 and 2 originate from the $^3\mathrm{D}_3$ state while the series 3 originates from the $^1\mathrm{P}_1$ state.

Figure 5.9 shows the measured ionization potentials of few actinides. The measured value of the IP of nobelium continues the trend of increasing IP for the heaviest actinides. This value is significantly larger than the measured IP value of lawrencium. Thus, it validates the hypothesis of a closed $5f$ and $7s$ atomic shell in nobelium. The uncertainty in the case of lawrencium is significantly larger as a consequence of a different measurement technique. The uncertainty in the IP value of Lr could be reduced by using laser spectroscopic techniques which in turn will provide the precision required for unambiguous determination of its electronic configuration.

In general, a good agreement was found between predictions and the experimental values. Predicted IP values from the intermediate Hamiltonian Fock-space coupled-cluster (IHFSCC) and the configuration interaction method combined with linearized single-double coupled-cluster (CI + all order) calculations deviate by less than 1% from the experimental value. For the $^3\mathrm{D}_3$-level energy, theory predictions deviate relatively larger (2%) from the

experimental value compared to other levels (the IP and the $^1P_1$). This is potentially caused by underestimation of the electron-electron correlation effects, the QED effects or both.

6 Hyperfine structure and isotope shift of nobelium isotopes

As described in the second chapter, nuclear ground state properties are accessible through laser spectroscopy, independent of nuclear models. Therefore, laser spectroscopy was extended to different nobelium isotopes. The hyperfine splitting (HFS) of ^{253}No and the isotope shift (IS) measurements for $^{252-254}$No were performed. This chapter describes the analysis of the atomic spectra obtained for the three isotopes of nobelium, which in combination with results from state-of-the-art atomic and nuclear-model calculations, give a unique insight on the nuclear structure in the region of deformed nuclide around neutron number $N = 152$.

6.1 Hyperfine structure of ^{253}No

The isotope ^{253}No ($T_{1/2} = 97$ s) was produced in the two-neutron evaporation channels of the complete-fusion reaction ^{207}Pb(^{48}Ca, 2n)^{253}No with a cross section of 1.3 μb [77], which is about a factor of two lower compared to the production of ^{254}No. Using the RADRIS technique the $^1S_1 \rightarrow {}^1P_1$ ground state transition at an excitation energy of $\bar{\nu}_1 = 29,961.457$ cm^{-1} was investigated in more detail employing the highest possible resolution. The dye laser used for scanning the first excitation step was equipped with an intra-cavity etalon, to reduce the laser bandwidth to about 1.2 GHz. The isotope ^{253}No has a tentative nuclear spin of $I(^{253}\text{No}) = (9/2)$ [118]. Taking this spin in conjunction with the angular momentum $J = 0$ for the ($^1S_0$) atomic ground state results in a total angular momentum of $F = 9/2$ according to Eq. 2.35. The excited atomic state ($^1P_1$) has an angular momentum $J' = 1$, which results in a hyperfine splitting with three total angular momentum quantum numbers $F' = 7/2, 9/2, 11/2$ (see figure 6.1) which can all be optically excited from the atomic ground state. Figure 6.2 shows the observed hyperfine spectrum for ^{253}No. From a total of three hyperfine components only two were resolved, limited by the pressure broadening in the gas cell and by the laser bandwidth.

In order to extract the hyperfine parameters of ^{253}No, figure 6.2, the rate equation model, developed in chapter 4 was adopted, in analogy to the model used in the case of fermium [23]. The resulting set of equations is

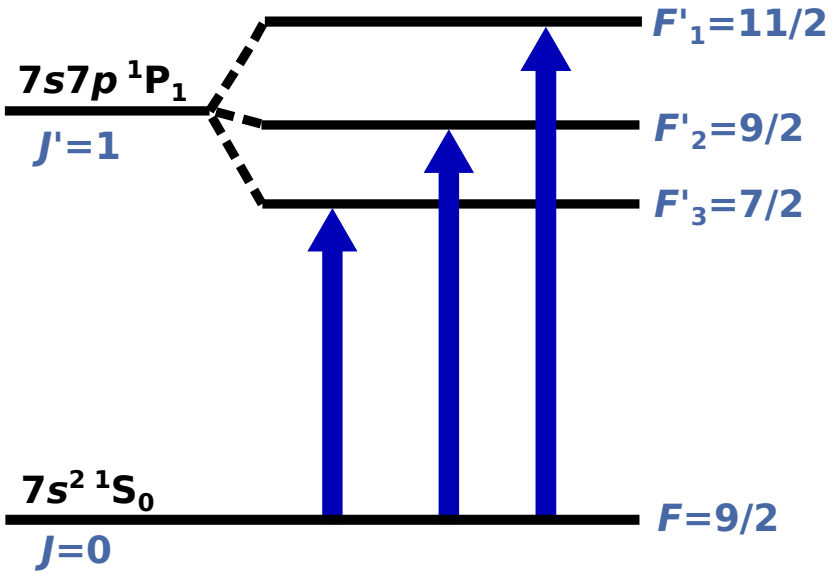

Figure 6.1: Schematic illustration of the hyperfine structure in ^{253}No which shows a hyperfine splitting of the upper energy level.

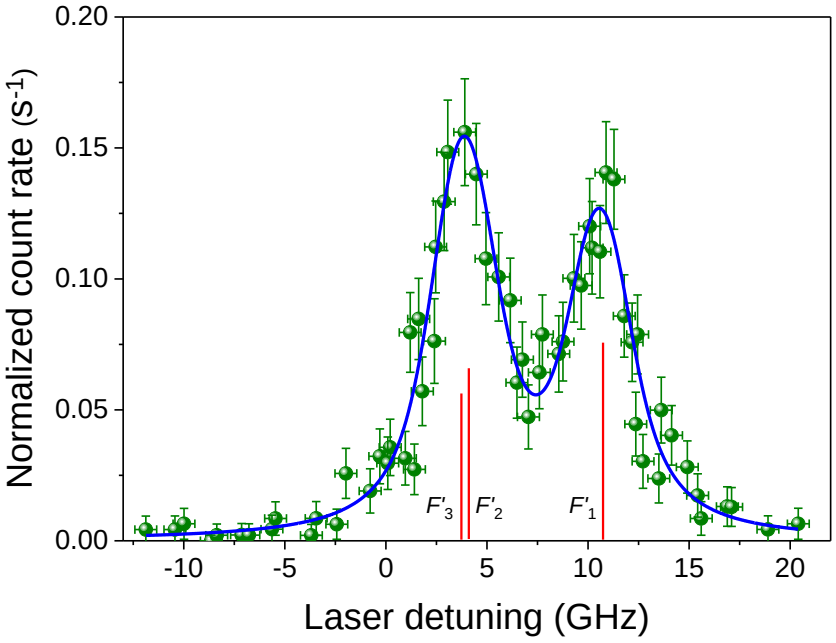

Figure 6.2: Measured spectrum of ^{253}No relative to the resonance of ^{254}No (shown as 0 GHz in the X-axis). The energetic positions of the HFS components are shown by the vertical lines, marked as F_1', F_2' and F_3', where the lengths of the lines indicate the expected Raccah intensities. The measurements were taken performed at 95 mbar Ag with a laser bandwidth of 1.2 GHz. The laser power was about 10 μJ per pulse for the first step and about 35 mJ per pulse for the second step.

$$
\begin{aligned}
\frac{d\rho_{33}}{dt} &= R_{\text{const.}} \sum_{F'} w^{F'} \rho_{22}^{F'} \\
\frac{d\rho_{22}}{dt} &= \frac{1}{2} \sum_{F'} (\rho_{11} - \rho_{22}^{F'}) A_{ki} S^{FF'}(t, \omega_L, \omega_{12}^{F'}) - A_{ki} \sum_{F'} \rho_{22}^{F'} - R_{\text{const.}} \sum_{F'} w^{F'} \rho_{22}^{F'} \\
\frac{d\rho_{11}}{dt} &= \frac{1}{2} \sum_{F'} (\rho_{22}^{F'} - \rho_{11}) A_{ki} S^{FF'}(t, \omega_L, \omega_{12}^{F'}) + A_{ki} \sum_{F'} \rho_{22}^{F'}
\end{aligned}
\tag{6.1}
$$

where the saturation parameter $S^{FF'}$ is given by [23]

$$
\begin{aligned}
S^{FF'}(t, \omega_L, \omega_{12}^{F'}) = \frac{\lambda_1^2}{2} \frac{E_1(t)/A_1}{t_1 \hbar \omega_{12}^{F'}} \frac{(2F+1)(2F'+1)}{2J+1} \begin{Bmatrix} J' & F' & I \\ J & F & 1 \end{Bmatrix}^2 \\
\int \frac{1}{\sqrt{2\pi}\sigma_\omega} exp\Big[- \frac{(\omega - \omega_L)^2}{2\sigma_\omega^2} \Big] \frac{\gamma_\omega'/2\pi}{(\omega - \omega_{12}^{F'})^2 + (\gamma_\omega')^2/4} d\omega.
\end{aligned}
\tag{6.2}
$$

$A_{ki} = 4.2^{+2.6}_{-2.8} \times 10^8$ s^{-1} is the Einstein coefficient for spontaneous emission for the ^{1}S$_0 \rightarrow ^1$P$_1$ transition reported in [24, 28]. $\omega_{12}^{F'}$ is the excitation energy of the HFS level with total angular momentum F'. $A_1 = 3.1$ cm^2 is the area illuminated, t_1 is the pulse length of the first step laser pulse and $E_1(t)/A_1$ is the energy flux of the scanning laser pulse and E_1 is the pulse energy. ω_L is the angular frequency of the first step laser. $\sigma_\omega = \sqrt{\sigma_D^2 + \sigma_L^2}$ is the Gaussian linewidth, comprising of the Doppler width $\sigma_D = 0.3$ GHz and the laser bandwidth $\sigma_L = 1.2$ GHz. $\gamma_\omega' = 1.8$ GHz is the Lorentzian linewidth arising from the gas collisions and phase fluctuations. $R_{\text{const.}}$ is the ionizing rate induced by the second laser [47]

$$
R_{\text{const.}} = \frac{E_2(t)/A_2}{t_2 \hbar \omega_2} \sigma_2 \ .
$$

Here, $E_2(t)/A_2 = 2$ mJ/cm^2 is the energy flux of the second step laser pulse with a pulse duration $t_2 = 25$ ns and an angular frequency ω_2, $\hbar$ is the Planck constant and σ_2 is the photoionization cross-section for the second step, which is in the order of 10^{-16} cm^2. The photoionization cross-section was assumed to be independent from the total angular momentum F and thus, the statistical weights $w^{F'}$ for the different transitions into the continuum were assumed to be equal to 1/3. The MINUIT package of the root evaluation software [100] was used as a χ^2minimization tool.

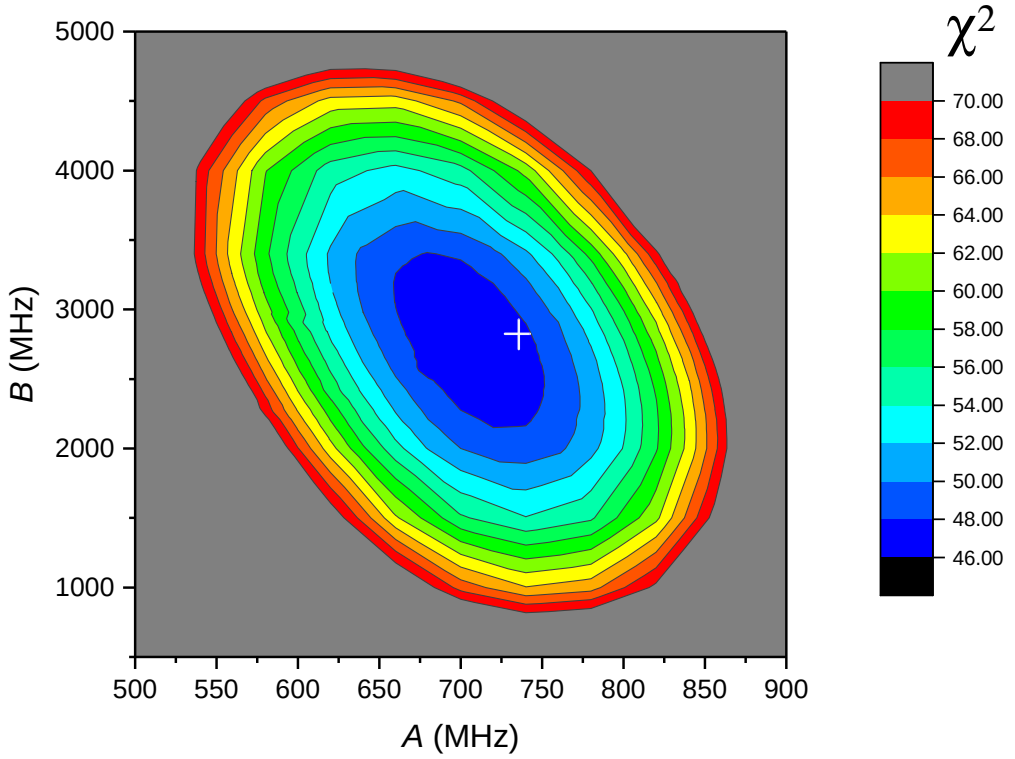

Figure 6.3: χ^2 map of the fit showing the correlation of the A and B hyperfine structure parameters. The white cross marks the value of A and B HFS parameters with the lowest χ^2 and thus the values taken for analysis purpose.

The frequencies for atomic transitions between the lower and the upper states are given by equation 2.39. The HFS constants A and B are related to the nuclear ground state properties- of the magnetic moment μ and spectroscopic quadrupole moment Q_s by the relation $A = \frac{\mu_I B_e(0)}{IJ}$ and $B = eQ_s \left\langle \frac{\partial^2 V_e}{\partial z^2} \right\rangle$ (see chapter 2.1.6). We derived the hyperfine coupling constants $A = 0.734(46)$ GHz and $B = 2.82(67)$ GHz for ^{253}No using a χ^2 minimization fit of the rate equation model, equation 6.1 to the experimental data. A significant correlation was observed between the hyperfine structure A and B-parameters when the rate equation model was fitted to the spectrum shown in figure 6.2 with different values of A and B. The resulting χ^2 map is shown in figure 6.3.

In order to extract the nuclear properties from the experimental observables, atomic calculations of the A and B-parameters are essential as no previous information and no stable (or long-live) reference isotopes are available. The atomic parameters $B_e(0)$ and $\left\langle \frac{\partial^2 V_e}{\partial z^2} \right\rangle$,

Table 6.1: The calculated and experimental values of the hyperfine structure constants A and B and the extracted nuclear moments μ and Q_s.

Atomic calculations Units	$A.I/\mu_N$ (GHz.I/μ_N)	B (Ghz)
CI+All orders	-6.27(90)	0.486(70)
CI+MBPT	-7.10(100)	0.503(75)
CIPT	-7.39(120)	0.624(90)
RCC		0.465(70)
MCDF	-4.09(180)	0.444(75)

	A (GHz)	B (GHz)
This work [29]	0.734(46)	2.82(69)

	μ (μ_N)	Q_s (eb)
This work [29]	-0.527(33)(75)	5.9(14)(9)

which are isotope-independent and connect atomic observables to nuclear properties were extracted from state-of-the-art atomic calculations. Different theoretical approaches were applied to calculate these parameters for nobelium: configuration interaction (CI) with the single-double coupled cluster method (CI+All-order), CI combined with many-body perturbation theory (MBPT) and relativistic Fock space coupled cluster (FSCC) techniques in different combinations [45, 44, 119, 20] as well as multi configuration Dirac-Fock (MCDF) calculations [120, 121]. The results of these individual calculations are given in table 6.1. All, the different methods in general agree within 20% with each other for these calculations. Using another method, which is based on the CI technique but additionally treats high-energy states perturbatively (CIPT method) [119], the influence of configuration mixing on the investigated $^1P_1$ level was evaluated. This allowed the exclusion of a strong mixing with core excitations, albeit with an increased uncertainty in the calculated value. From the investigation of chemical elements featuring a similar electronic configurations as nobelium, the most accurate values for the hyperfine A parameter is expected for CI+All order calculations. Thus, this value was taken for extracting the nuclear magnetic moment. For the case of the hyperfine parameter B, CI+All order and FSCC calculations provided a similar uncertainty and an average value of 0.476(70) GHz/eb was used in the evaluation procedure. More about the theoretical calculations can be found in Appendix 8.4.

Using these atomic calculations and the experimental value of the hyperfine $A-$parameter, the magnetic moment extracted amounts to $\mu(^{253}\text{No}) = -0.527(33)(75)\mu_\text{N}$. Here, μ_N denotes the nuclear magneton. The value in the first bracket represents the statistical uncertainty (1σ) and the value in the second bracket represents the uncertainty arising from the

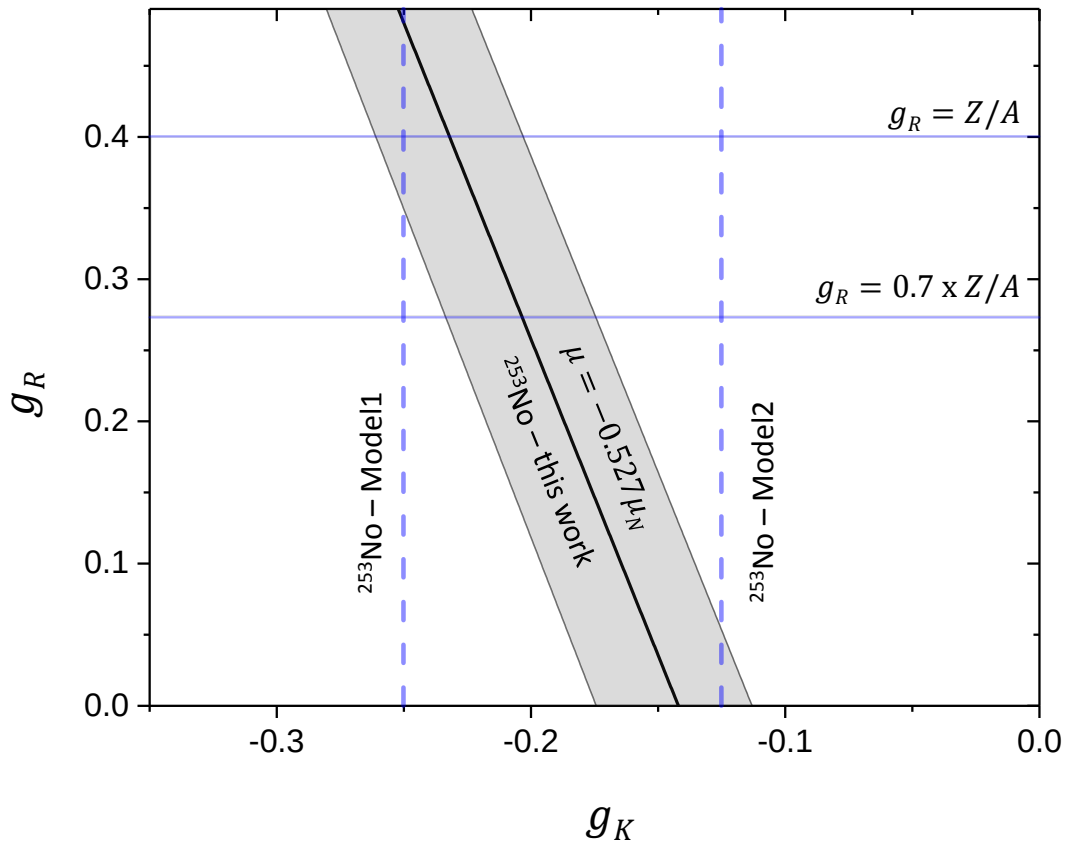

Figure 6.4: Relation between the g-factors g_R and g_K from the measured magnetic moment $\mu(^{253}\mathrm{No})$. Model 1 and 2 refers to results from [123] and [124], respectively. The grey shaded area is the uncertainty in the extracted magnetic moment μ in our experiment. The solid blue lines are the different values of g_R used to extract the g_K and blue dashed lines are the g_K values taken from Model 1 and 2.

theoretical calculations (1σ). For ^{253}No, which features an even number of protons and an odd number of neutrons, the nuclear magnetic properties arise mainly from the unpaired neutron. The determination of the magnetic dipole moment μ therefore enables probing nuclear shell model predictions of the underlying nuclear single-neutron wave function. For the band-head of a rotational band the magnetic nuclear moment is linked to the μ_N by

$$\mu/\mu_\mathrm{N} = g_R I + (g_K - g_R)\frac{K^2}{I+1}. \tag{6.3}$$

K is the projection of I onto the symmetry axis. The rotational g-factor is approximated as $g_R \approx \frac{Z}{A}$ and $g_R \approx 0.7 \cdot \frac{Z}{A}$ for an unquenched and quenched system, respectively [125]. The single-particle $g-$factor g_K can be predicted by nuclear models. For ^{253}No there have been two distinct values reported where Model 1 gives $g_K = -0.25$ [123, 125] while Model 2

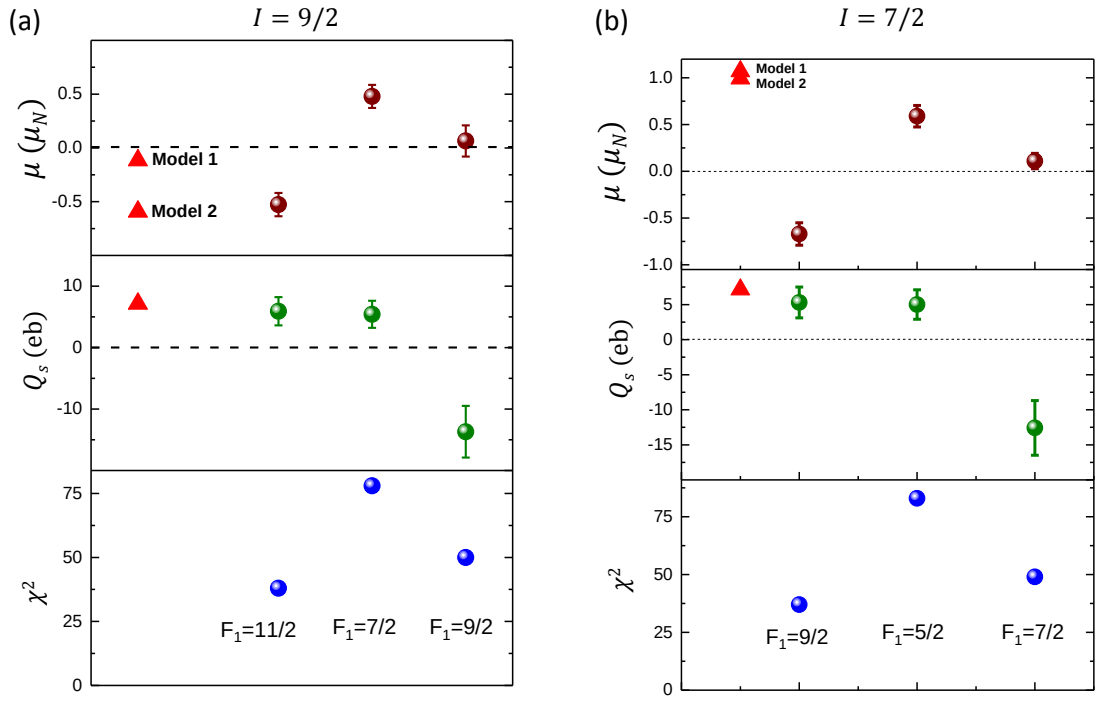

Figure 6.5: Extracted nuclear magnetic dipole (brown bullets) and electric quadrupole (green bullets) moments and χ^2 values expressing the fit quality (blue bullets) for different assignments of the HFS peaks (marked by $F_{1,2,3}$ values) and for nuclear spins $I(^{253}\mathrm{No})$=9/2 (a), and $I(^{253}\mathrm{No})$=7/2 (b), together with corresponding literature values (triangles) according to ref. [123] (Model 1) and ref. [124] (Model 2).

reports $g_K = -0.12$ [124] for the $9/2^-[734]$ neutron configuration. Using equation 6.3 in combination of our experimental results on the magnetic moments these predictions can be evaluated as graphically represented in figure 6.4. From the magnetic moment of $\mu(^{253}\mathrm{No}) = -0.527(33)(75)\mu_\mathrm{N}$ obtained in our experiment, a g-factor of $g_K^{\mathrm{exp}} = -0.22(5)$ was extracted, which agrees well with the results from Model 1 but disagrees with Model 2.

The spectroscopic quadrupole moment $Q_s^{\mathrm{exp}} = 5.8(14)(9)$ eb is extracted from the HFS $B-$parameter. This indicates a strong prolate deformation for ^{253}No nucleus. A value of the deformation parameter $\beta_2 = 0.27 \pm 0.03$ has been reported from the in-beam spectroscopy of ^{254}No [126]. Using this value of the deformation parameter, the intrinsic quadrupole moment of $Q_0 = 13.1$ eb [123, 124] was calculated according to [57, 58]

$$Q_0 = \frac{3}{\sqrt{5\pi}} ZeR^2\beta_2(1+0.36\beta_2), \tag{6.4}$$

where R is the radius of a homogeneous sphere of mass A [58]. The experimental spectroscopic quadrupole moment (Q_s) is related to the intrinsic quadrupole moment (Q_0) with the assumption of a well-defined deformation axis by

$$Q_s = \frac{3K^2 - I(I+1)}{(I+1)(2I+3)} Q_0 \tag{6.5}$$

where K is the projection of I on the deformation axis. This leads to a quadrupole moment value of $Q_s = 7.1$ eb. Comparing our experiment results to this shell model-dependent value, obtained from the moment of inertia in the rotational band of ^{254}No [124, 127, 128], indicates a stable deformation in the isotope chain of nobelium.

The HFS splitting for ^{253}No is not fully resolved and in general the three expected hyperfine peaks can be assigned in different arrangements to the $F(I) \rightarrow F'(I-1, I, I+1)$ transitions. Figure 6.5 shows the three possible assignments for two different spins ($I = 9/2; 7/2$) which have been suggested for the nuclear ground state configuration in ^{253}No [123, 125]. The extracted nuclear parameters and the χ^2 value of the best fit are given for each case. The peak assignment of $F_1' = I$ (see figure 6.2) can be excluded for both cases as the spectroscopic quadrupole deformation Q_s results in an oblate deformation, which contradicts a strong prolate deformation obtained from in-beam spectroscopy of the neighbouring isotope ^{254}No [123, 124]. In addition, the assignment $F_1' = I - 1$ can be excluded for both nuclear spins from the fit quality. For the assignment $F_1' = I + 1$ and spin $I = 7/2$ the sign of the deduced magnetic moment μ does not match with the expectation for a $7/2^+$ [624] configuration [123, 124]. Therefore, a spin I(^{253}No) $= 9/2$, corresponding to a ground state configuration $9/2^-$ [734], is favoured and is in full agreement with model-dependent evaluation of the coupling strength of the ground state rotational bands in ^{253}No [123, 125].

6.2 Isotope shift of nobelium isotopes

For even mass nuclei with zero nuclear spin, the information on the nuclear size and deformation is available from the isotope shift of an atomic transition $\delta\bar{\nu}^{A,A'} = \bar{\nu}^A - \bar{\nu}^{A'}$ between two isotopes of mass m_A and $m_{A'}$, as explained in chapter 2.1.7. The isotope shift of the $^1S_0 \rightarrow {}^1P_1$ ground state transition measured for the nobelium isotopes $^{252-254}$No is given in figure 6.6. Isotope shift values of $\delta\bar{\nu}^{253,254} = 6.72(18)$ GHz and $\delta\bar{\nu}^{252,254} = 10.08(69)$ GHz have been measured in this work. The isotope shift is related to the change in the mean square charge radius $\delta\langle r^2\rangle^{A,A'}$ by equation 2.47.

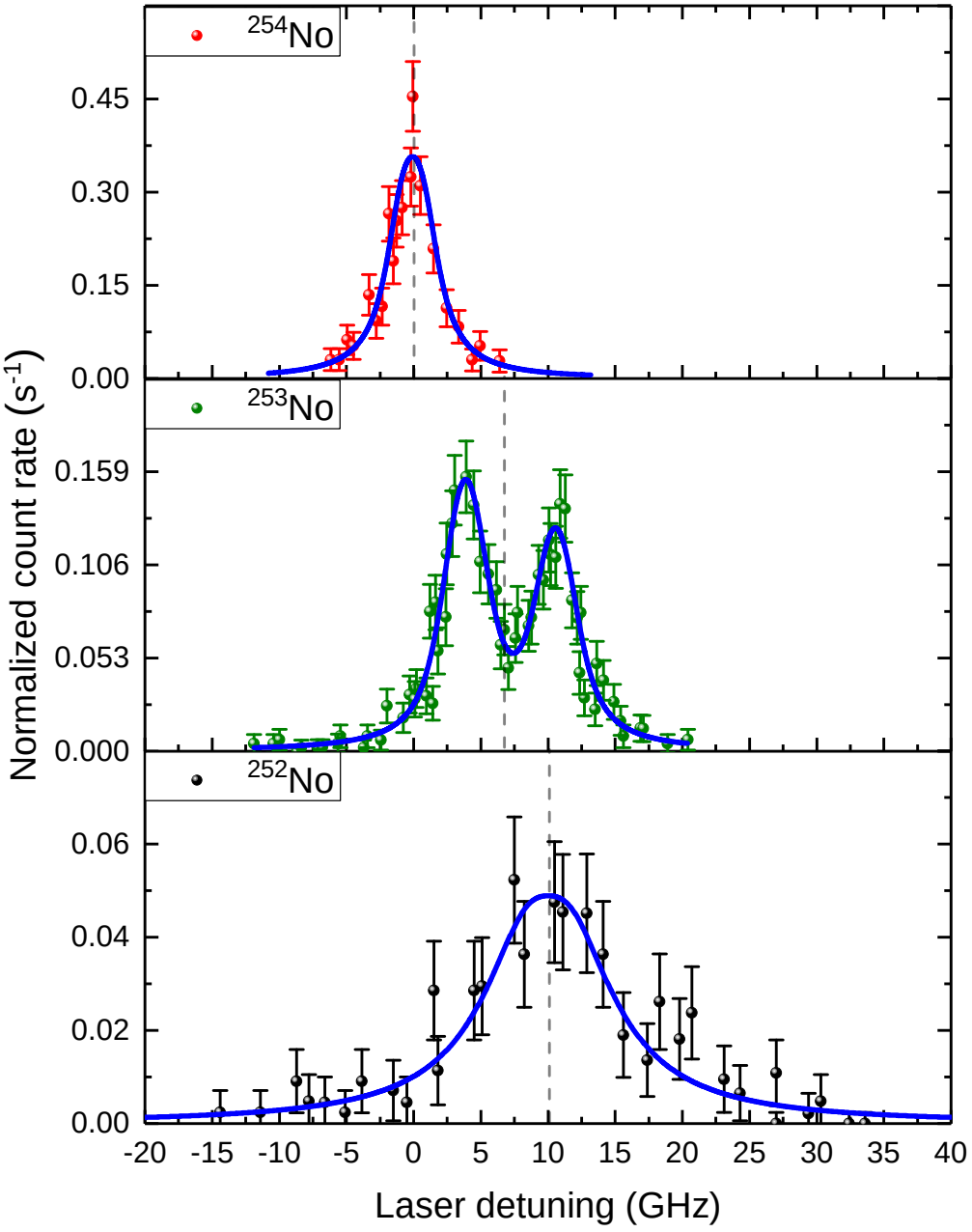

Figure 6.6: The measured resonances to the $^1P_1$ state in $^{252-254}$No with the best fit (solid line) to the data using the rate equation model described in chapter 2 and chapter 6. The vertical dashed lines are the centre of gravity of the resonance for each isotope. All the measurements were performed at 95 mbar Ar pressure. The laser frequency was 1.2 GHz for ^{253,254}No and 5.5 GHz for ^{252}No. Adapted from [29].

Table 6.2: The calculated and experiment values of the field shift F_s and mass shift M constant and the extracted changes of the mean square charge radius $\delta\langle r^2\rangle$.

Atomic calculations	F_s	M
Units	(GHz/fm^2)	(GHz·amu)
CI+All	-95.8(70)	
CI+MBPT	-104.0(100)	
CIPT	-93.6(250)	
RCC	-98.8(150)	
MCDF	-113.0(250)	1044(400)

	$\delta\bar{\nu}^{253,254}$ (GHz)	$\delta\bar{\nu}^{252,254}$ (GHz)
This work [29]	6.72(18)	10.08(69)

	$\delta\langle r^2\rangle^{253,254}$ (fm^2)	$\delta\langle r^2\rangle^{252,254}$ (fm^2)
This work [29]	-0.070(2)(5)	-0.105(7)(7)

As in the case of the HFS of ^{253}No, different theoretical methods were used for the calculation of the field shift F_s and mass shift M constants and the results are tabulated in table 6.2. Assuming a constant nuclear surface diffuseness, the mean square charge radius between two isotopes A and A' is related to the quadrupole deformation parameter $\langle\beta_2\rangle$ in the second order by [58]

$$\delta\langle r^2\rangle^{A,A'} = \delta\langle r^2\rangle_0^{A,A'} + \langle r^2\rangle_0 \cdot \frac{5}{4\pi}\delta\langle\beta_2^2\rangle^{A,A'}. \tag{6.6}$$

In order to infer the deformation of investigated nobelium isotopes, the expected change in the mean square charge radii of spherical nuclei $\delta\langle r^2\rangle_0^{A,A'}$ in equation 6.6 predicted from the droplet model (DM) is subtracted [63, 130]. This results in the change in deformation between isotopes. Figure 6.7 shows the change in the deformation of nobelium isotopes along with the even$-Z$ actinides and radium. The lighter actinides, for which charge radii information has been extracted [129], show an increase in deformation with increasing neutron number from $N = 122$ to $N = 152$. In contrast, the investigated nobelium isotopes feature a stable deformation, which is expected in the proximity to a shell closure, as can also be seen, e.g., in the case of Ra ($Z = 88$) at $N = 126$. This evidence of a stable deformation is in agreement with theoretical predictions [131, 132] and substantiates model-dependent results from in-beam spectroscopy in $^{252-254}$No [123, 125, 133].

The droplet model mentioned above is typically used for laser spectroscopic investigations up to the lead region [58] and is apparently not suitable for heavier isotopes. Another way

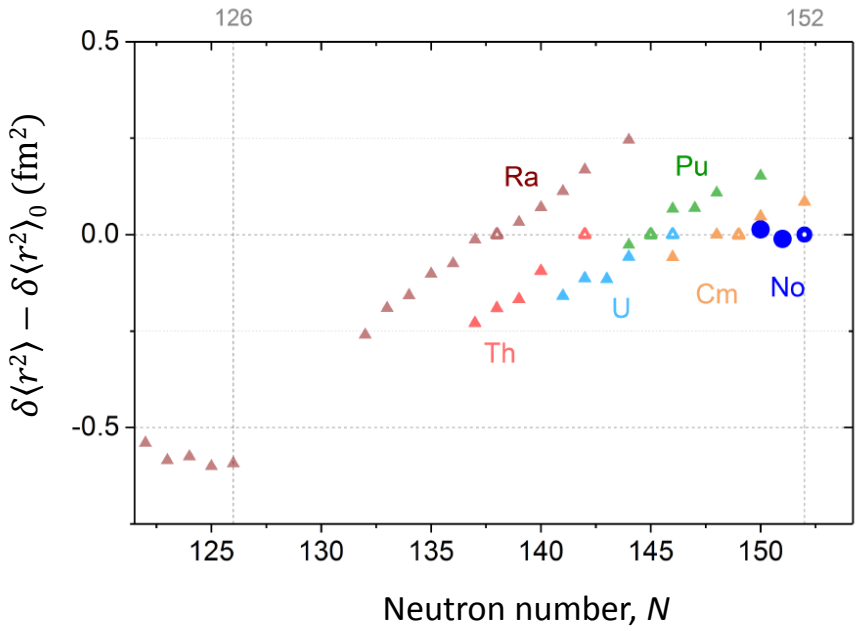

Figure 6.7: The change in deformation related changes in charge radius for $^{252-254}$No and even Z nuclei starting from radium ($Z = 88$) are plotted relative to the reference isotopes ^{226}Ra, ^{232}Th, ^{238}U, ^{239}Pu, ^{244}Cm and ^{254}No (open symbols). Data for the lighter elements taken from [129].

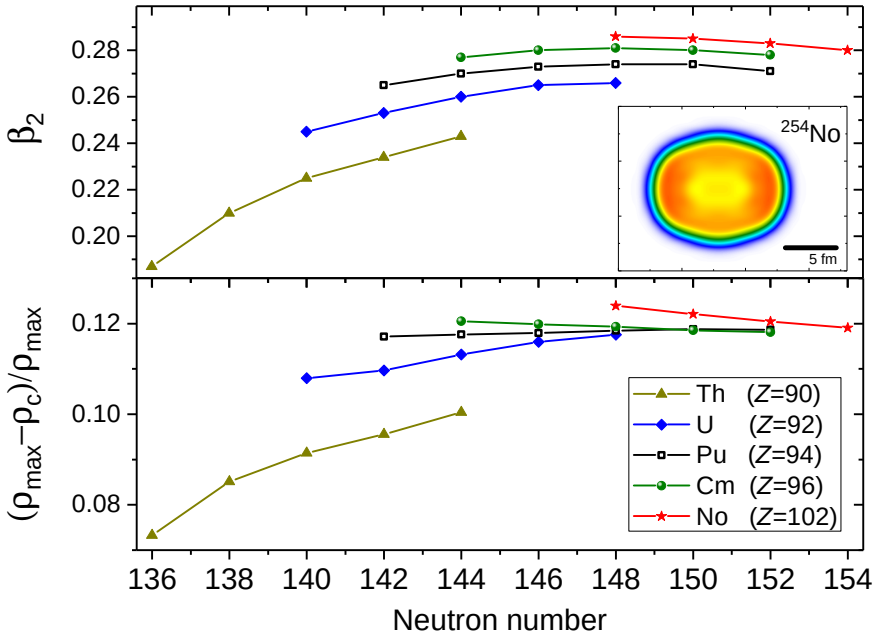

Figure 6.8: Upper panel: deformation parameter β_2 for different even-even isotopes of Th, U, Pu, Cm, and No obtained from DFT calculations with UNEDF1 functional. The inset figure shows the calculated proton distribution of ^{254}No from high density (red) to low density (blue). Lower panel: depth of the central depression. Adapted from [29].

to interpret the data is to use nuclear calculations based on self-consistent nuclear density functional theory (DFT) without any symmetry restrictions [134]. For the heavier isotopes DFT predicts a central depression of the proton density, *i.e.*, a reduction of the density in the nuclear interior [135]. This central depression in the charge distribution is a result of the strong Coulomb repulsion among the protons [131, 135, 136]. The central depression can be quantified by the depletion factor as [137, 138]

$$F = \frac{\rho_{\max} - \rho_{c}}{\rho_{\max}} \tag{6.7}$$

where ρ_c and $\rho_{\max}$ denotes the central and maximum (point-nucleon or charge) density. The central depression can be accessed by employing density functional theory with the globally optimized Skyrme energy density functionals SV-min [139], SLy6 [140] and UNEDF1 [141]. An alternative to the Skyrme functionals for the calculation of the charge radii are the Fayans functionals [142]. However, those functionals overestimate the pairing correlations especially in the actinide region, which could have a significant influence on the results.

Using the DFT calculations with UNEDF1, the quadrupole deformation parameters β_2 were extracted for even-even isotopes of some even$-Z$ actinides [143]. This is shown in the upper panel of figure 6.8. It can be seen that the deformation parameter β_2 increases with N and reaches a maximum around $N = 148$, which agrees with other DFT predictions while microscopic-macroscopic models typically predict the maximum deformation around $N = 152$ [131, 132]. Nevertheless, for the investigated nobelium isotopes β_2 values come close to a constant indicating a stable deformation around $N = 152$. The calculated proton density distribution for ^{254}No from the DFT calculations is shown in the figure 6.8 upper-panel (inset), indicating both a pronounced deformation of the nucleus as well as a central depression of more than 12% in the proton distribution.

Figure 6.9 shows the changes in the mean square charge radii of the nobelium isotopes measured in this work in comparision to the experimental values for other actinides, taken from references [129, 144]. Our measurements are in good agreement with the results from state-of-the-art nuclear density functional theory. The droplet model separates the contribution of the change in size of a spherical nucleus depending on the number of constituent nucleons, from the deformation. The grey line in figure 6.9 gives the trend for a stable deformation and an increase in the radii solely according to the droplet model. An increase is expected from the droplet model with constant deformation nonetheless, the deviation from this trend for many nuclei in the actinide region, indicates that the charge radii increases. This is potentially due to nuclear deformation and central depression of the charge distribu-

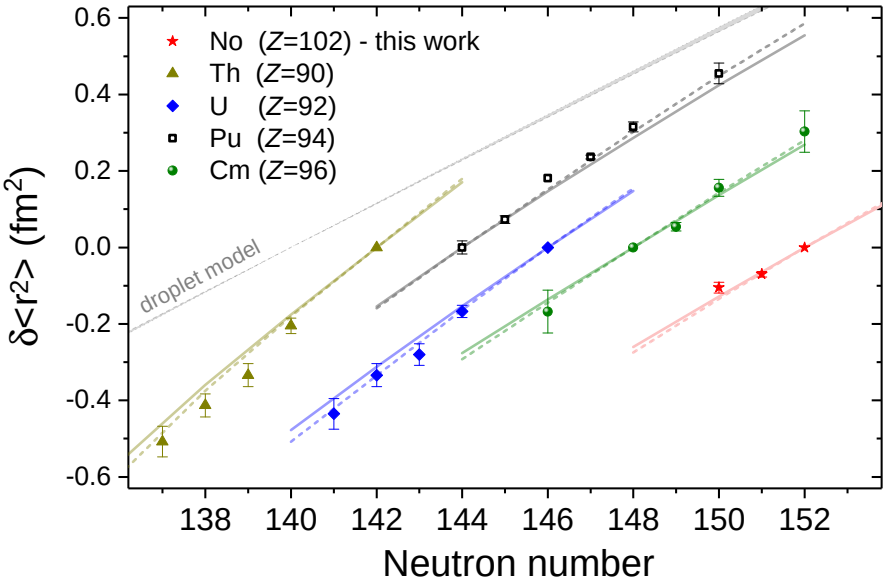

Figure 6.9: $\delta\langle r^2\rangle$ for $^{252-254}$No and even Z nuclei starting from thorium are plotted. For each element the DFT calculations with two different Skyrme energy density functionals, SV-min (solid line) [139] and UNEDF1 (dashed line) [141], are shown. The grey line indicates the behaviour of a constant deformation for elements with $Z = 90 - 102$ using a droplet model [63, 130]. Adapted from [29].

tion which is not taken into consideration in the droplet model in the region of high Z with strongly deformed nuclei. Our values for the mean square charge radii are in good agreement with the DFT calculations and supports the theoretical presiction of a stable deformation for the isotopes of nobelium.

7 Summary and outlook

This thesis presents the laser spectroscopic studies of three nobelium isotopes performed using the RADRIS technique at SHIP, GSI. 29 Rydberg states excited from two states ($^1P_1$ and $^3D_3$) were observed, which led to the extraction of the first ionization potential of nobelium. In addition, the buffer gas induced quenching of the $^1P_1$ state to the $^3D_3$ state, allowed the extraction of the energetic position of the $^3D_3$ state. The $^1S_0 \rightarrow ^1P_1$ transition was probed, and the hyperfine structure of ^{253}No was measured for the first time, leading to the extraction of the nuclear magnetic moment μ and spectroscopic quadrupole moment Q_s, thereby giving access to the single particle $g-$factor and nuclear deformation. Isotope shifts were measured for $^{252-254}$No, and the changes in the mean square charge radii were extracted. These measurements will now pave the road for laser spectroscopic investigation of other nobelium isotopes and heavier elements in the future.

Spectroscopy of nobelium

As shown in the work the RADRIS technique is well suited for the experiment of nobelium isotopes. Following are a few suggestions for further measurement campaigns on nobelium.

Search for further atomic states

In addition to the transitions observed in nobelium, atomic energy states can be excited in nobelium, for example the [Rn] $5f^{14}$ $7s7p$ $^3P_1$ triplet state in ^{254}No, for which accurate predictions are available [39, 43]. This can then be used to extract the hyperfine A and B parameters for odd-mass isotopes. To date, the hyperfine spectroscopy can be performed solely on the $^1P_1$ state in No. The A obtained for this state has only a moderate accuracy due to the uncertainty of more than 15% in theoretical calculations [162]. In contrast to this, the A factor for $^3P_1$ state is predicted with higher accuracy of about 5%. This state would also enable the extraction of the B parameter with a higher precision.

Extend the isotope chain in nobelium.

Further laser spectroscopic investigation on other nobelium isotopes, namely ^{251,255}No will give insight into the evolution of the mean square charge radii while crossing the $N = 152$ deformed shell closure. The isotope ^{251}No ($T_{1/2} = 0.8$ s, $I = 7/2^+$) can be produced in the 3n-channel of the reaction ^{48}Ca+^{206}Pb with a cross-section of about 30 nb [163]. With the efficiency of the RADRIS set-up, about 2% expected for this isotope of nobelium, a RIS rate of 0.06 counts/min can be achieved at a beam current of 1 particle microampere (μA_p).

The isotope ^{255}No ($T_{1/2} = 3.1$ min, $I = 1/2^+$) can be produced in the 1n-channel of the reaction ^{48}Ca+^{208}Pb with a cross-section of 140 nb [164]. The $\alpha-$energy of this isotope is 8.096 MeV, that is very close to that of ^{254}No. The isotope ^{255}No also can be produced via the electron-capture (EC) of ^{255}Lr ($T_{1/2} = 31.1$ s) and can be successively ionized using resonance ionization. A proof-of-principle experiment has already been performed during the last beamtime. Figure 7.1 shows the observed $\alpha-$decay spectrum.

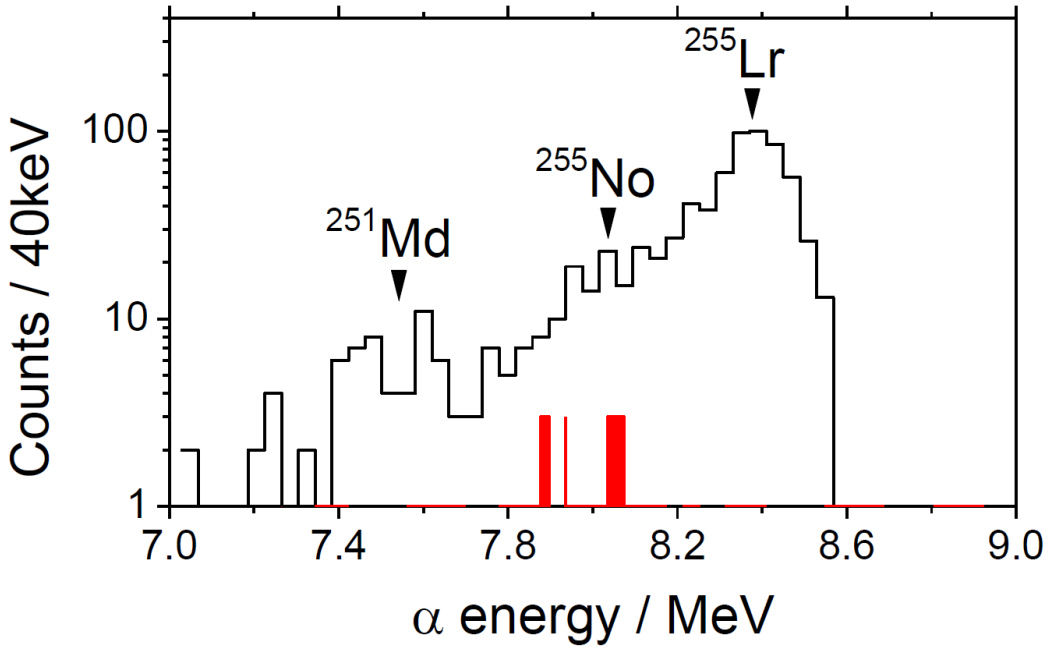

Figure 7.1: $\alpha-$decay spectrum of (solid lines) of Lr registered over a period of about 4 hrs by the PIPS detector at an average beam current of 0.5 μA_p. The red filled are is the $\alpha-$decay spectrum of ^{255}No, ionized using laser radiation and produced via the EC-of ^{255}No. Due to the lack of time the conditions were not optimized.

The RADRIS technique can also be incorporated for the search of the atomic transitions in lawrencium (Lr, $Z = 103$). The isotope ^{255}Lr can be produced in the reaction ^{209}Bi(^{48}Ca,2n)^{255}Lr with a production cross-section of 400 nb [165]. After being separated from the projectiles by SHIP, the fusion products are expected to arrive at the optical cell at a rate of about 0.5 ions/s. Due to this very low production rate, the evaporation of Lr atoms from the filament needs to be optimized in order to suppress the background due to surface ionization. Thus different filaments, such as hafnium-coated tungsten or yttrium coated tungsten filaments could be used. Since hafnium exhibits a smaller work function compared to tantalum, it could be used for on-line measurements for Lr.

Many different ground state transitions have been predicted for Lr, but the most promising one would be $^2S_{1/2}$ state predicted at 20,131 cm^{-1} with a transition amplitude of 2.7×10^7 s^{-1} or the $^2D_{3/2}$ state at 28,096 cm^{-1} [166]. A two-step excitation scheme with the dye lasers used for the first step while the second step will be a non-resonant excitation into the continuum using an excimer laser. Taking into consideration a 1σ uncertainty of 600 cm^{-1} in the theoretical predictions a wavelength range of 19,700 cm^{-1} $\leq \bar{\nu}_1 \leq$21,000 cm^{-1} and 27,500 cm^{-1} $\leq \bar{\nu}_1 \leq$28,700 cm^{-1} should be covered by the dye lasers. Assuming an overall efficiency of about 3% for ^{255}Lr, a RIS rate at the detector of 0.03 events/s at 1 μA$_p$ the scan for the $^2S_{1/2}$ state can be achieved in about 15 days. The observation of a ground state transition opens up possibilities for the search of Rydberg states from which a precise value of the ionization potential of lawrencium can be extracted. These measurements would for the first time provide experimental access to the ground state configuration of lawrencium.

Appendix

Data Acquisition efficiency

In order to test the performance of the data acquisition (DAQ), a number of measurements were performed to test the acquisition speed and the reliability of the data acquisition system. For this purpose a pulse generator supplied a signal and a trigger for the DAQ to acquire the signal. As reported in chapter 3.3 the DAQ has the ability to acquire eight analog inputs simultaneously. For our experiment only three of these eight channels were activated. In order to test the DAQ a signal from the pulse generator was fed into the three input channels. The signal frequency was mapped starting from 25 Hz to 100 kHz. The dead time losses of the detection system were below 0.5% up to a signal frequency of about 8 kHz. The dead time losses increases to about 2% at a signal rate of about 10 kHz. In comparison, the $\alpha-$decay rates for nobelium is less than one event per second.

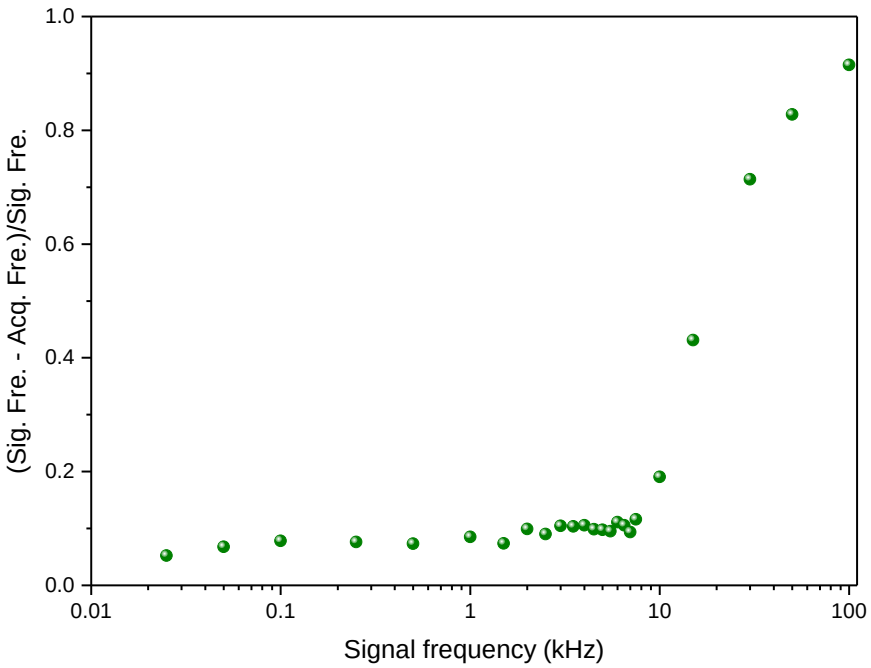

Figure 7.2: Dead time losses of the data acquisition.

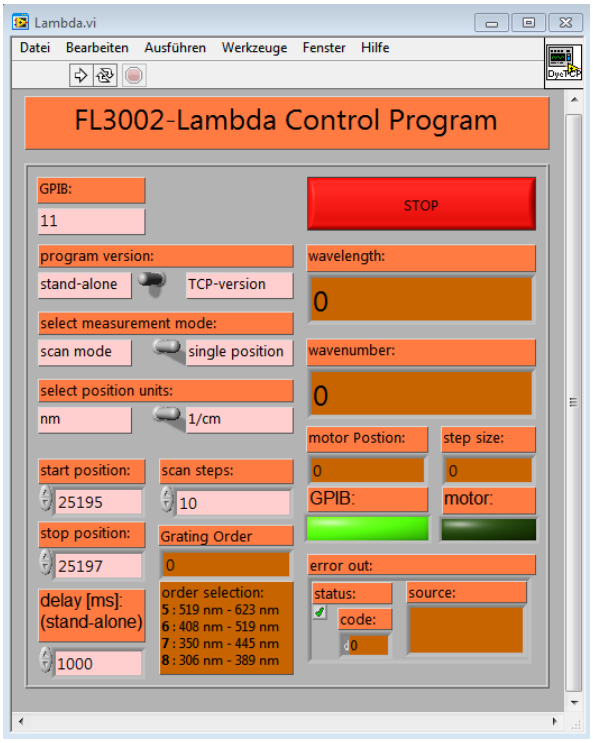

Figure 7.3: Laser control program.

As mentioned in chapter 3 the LabVIEW based data acquisition (DAQ) software has three measurement modes. The most important among them is the wavelength scan mode. The steps for starting up the scan mode are given below:

- First the wavelength scan and the step size should be fixed. Figure 7.3 shows the dye laser control program.
  - In order for the DAQ to trigger the wavelength change, the program version toggle switch should be at TCP-version.
  - To scan a given wavelength, the measurement mode toggle switch should be in scan mode.
  - Next is to determine the start position (wavenumber), the stop position (wavenumber) and the scan steps. Be aware, these positions are calculated from the motor position and may have some offset to the actual wavenumber. This program will then change the laser wavelength according to the user-defined measurement time for each step, which will be provided by the DAQ.

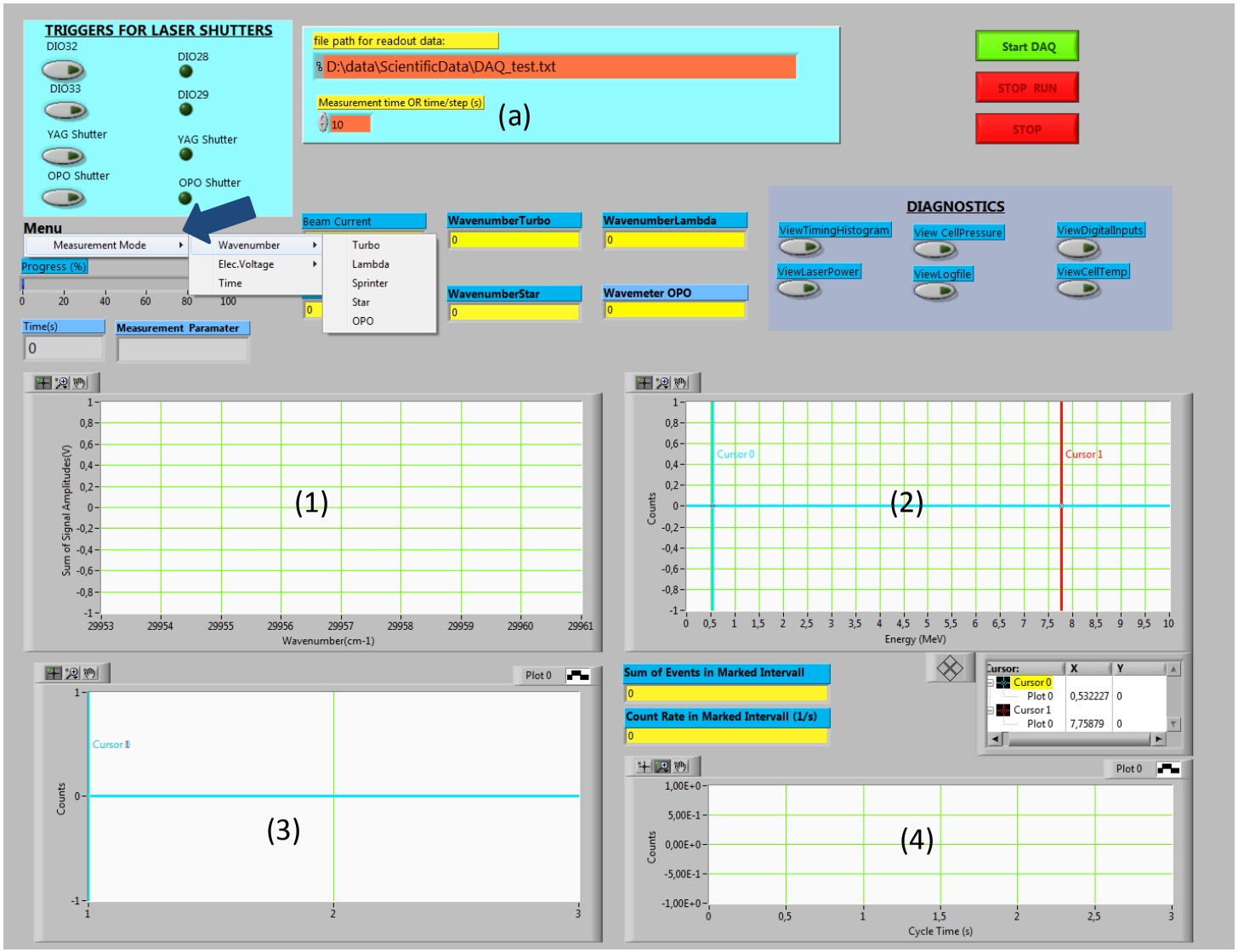

Figure 7.4: LabVIEW based DAQ software.

- The user now should provide the measurement time per step, marked as (a), in the DAQ software shown in figure 7.4.
- Once this is done, the user should run the DAQ software, and press "Start DAQ" (green button). Following this, a pop up (blue arrow) will appear where the user can select the measurement mode, which in this case would be "wavelength". Doing this will activate all the dye lasers, but the user should choose one for monitoring purpose.
- The DAQ software has four graphical windows
  - Plot (1): shows the observed spectrum with reference to the wavenumber of the selected laser. Only events in between Cursor 0 (blue) and 1 (red) are taken into consideration for this.
  - Plot (2): the $\alpha-$spectrum of the isotope of interest. In the scan mode one has to define the region of interest (ROI) by the two cursors.
  - Plot (3): plots the total ROI events registered at the detector per scan step of the laser.
  - Plot (4): is the cycle time histogram. Here, the number of ROI events are plotted with respect to the measurement cycle. If the isotope has a short half-life ($T_{1/2}$), with the help of this plot one can determine the $T_{1/2}$ of the isotope as was shown for ^{155}Yb in the reference [27].

Even though, the user chooses only one dye laser during the scan process, the corresponding wavenumber of each dye laser is written to the file, thus giving the possibility to refer the wavenumber during analysis proceduree.

Efficiency measurements for ^{252}No and ^{253}No

The overall efficiency of resonance ionization spectroscopy (RIS) measurements is defined as the ratio of the nobelium decay counts measured by the PIPS detector, A_{ion}, to the implantation rate of the nobelium ions delivered to the gas cell, A_{ion}. The A_{ion} is measured using a retractable silicon strip detector. The overall RIS efficiency of ^{254}No is about $6.4 \pm 1\%$ and has been reported in [24, 27]. Since the cycle time has to be adapted depending on the half-life of the nuclide of interest, the efficiencies for ^{254}No and ^{253}No differ from the one for ^{254}No.

Efficiency of ^{252}No

The RIS signal for ^{252}No is shown in figure 6.6. An average count rate of $A_{\text{ion}} = 0.048$ per second per particle microampere was obtained at the PIPS detector for ^{252}No. In the case of ^{254}No an average count rate of 0.39 per second per particle microampere was obtained which corresponds to an overall efficiency of $\varepsilon_{^{254}No} = 6.4 \pm 1\%$. Thus, the overall RIS efficiency for ^{252}No is extracted by scaling it to $\varepsilon_{^{254}No}$ by

$$\begin{aligned} \varepsilon_{^{252}No} &= \varepsilon_{^{254}No} \times \frac{A_{^{252}No}}{A_{^{254}No}} \times 4 \\ &= 6.4 \times \frac{0.048}{0.39} \times 4 \\ &= (3.2 \pm 1)\ \% \end{aligned} \tag{7.1}$$

The factor of 4 is to compensate for the production cross-section.

Efficiency of ^{253}No

A broadband RIS signal for ^{253}No is shown in figure 7.5. In this case the measurement time for each step is 600 s. At the resonance maximum, 124 events were recorded on the PIPS detector in 600 s at a beam current (I) of 35.3 μA. For similar measurements in ^{254}No, 62 events were recorded in 300 s at a beam current (I) of 22.67 μA. This gives an overall efficiency for ^{253}No

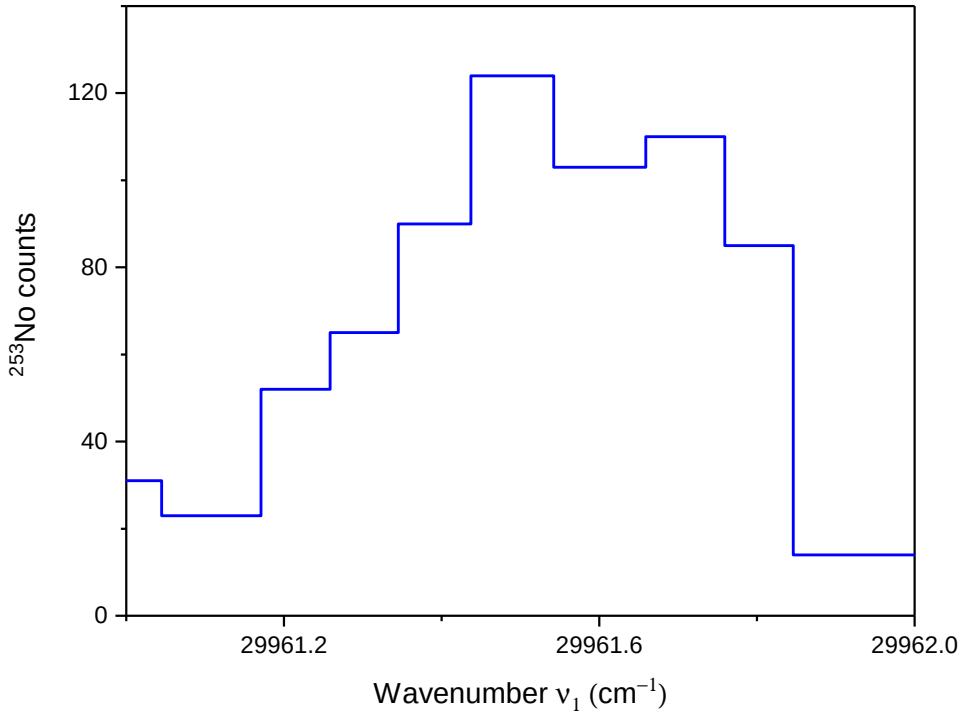

Figure 7.5: Laser scan of the $5f^{14}\ 7s7p\ ^1\mathrm{P}_1$ level in ^{253}No using an increased laser bandwidth of 5.5 GHz.

$$\begin{aligned}\varepsilon_{^{253}No} &= \varepsilon_{^{254}No} \times \frac{A_{^{253}No}}{A_{^{254}No}} \times \frac{I_{^{253}No}}{I_{^{253}No}} \\ &= 6.4 \times \frac{0.21}{0.21} \times \frac{22.67}{35.3} \\ &= (8.2 \pm 1)\ \%\end{aligned} \tag{7.2}$$

The factor of 2 is to compensate for the production cross-section.

Atomic calculations

In the heaviest elements (Z>100) no stable of long-lived reference isotopes are available. Thus, to extract nuclear properties from the experimental observables, atomic calculations are needed and have been calculated by our collaborators using different theoretical models. The calculation of the electronic structure of the heaviest elements is especially difficult due to large electron correlations as well as increasing relativistic and QED effects [20, 21]. The excitation energy of the [Rn]$5f^{14}7s7p$ ^{1}P$_1$ level in neutral nobelium was predicted by different theoretical approaches such as configuration interaction (CI), coupled cluster techniques and Multi-configuration Dirac-Fock (MCDF) calculations [24]. For this work, the wave functions extracted by different methods have been evaluated to obtain the nuclear coupling parameters.

Multi-configuration Dirac-Fock (MCDF)

The MCDF method [121] as implemented in the GRASP2K code [120] was used to compute the isotope shift parameters and the hyperfine coupling constants for the $7s^2$ (^{1}S$_0$)$\rightarrow 7s7p$ (^{1}P$_1$) transition in nobelium. The field shift constant F_s was estimated based on a series of configuration interaction calculations [145] with varying nuclear mass and radius as detailed in [146, 147]. For the computation of the mass shift constants, the expectation value of the relativistic recoil Hamiltonian in the approximate wave functions was computed as implemented in the RIS3 [148] program.

In the MCDF method, the approximate wave functions are represented as a superposition of jj-coupled configuration state functions (CSFs) with the same total angular momentum and parity. In lowest-order approximation (Layer 0), the configuration space is given by the three CSFs with $J = 0$, 1 that arise from the two reference configurations $7s^2$ and $7s7p$. Starting from these two reference configurations, the configuration space was systematically enlarged by performing virtual excitations from some core and valence orbitals into virtual orbitals to effectively capture corrections due to the electron-electron correlation. In this manner, the next layer (Layer 1) adds single, double and triple excitations from the $5f$, $7s$ and $7p$ orbitals to the $5f$, $6d$, $7s$ and $7p$ orbitals. Successively, five more correlation layers are added by including single and double excitations from the $5f$, $6p$, $7s$, $7p$ orbitals into nl orbitals, where $nl = s...g$ and $n = 8-12$.

Table 7.1 presents results for six correlation layers on top of the Dirac-Fock calculation are shown. It shows the transition energy, the mass shift constants and the field shift constant of the ^{1}S$_0 \rightarrow ^1$P$_1$ transition for each correlation layer. In case of the mass shift,the values for

Table 7.1: Transition energy, mass shift and field shift constants for the $^1S_0 \rightarrow ^1P_1$ transition in nobelium from the MCDF calculations. The results for different sizes of the configuration space (layers) are shown, as described in the text.

Layer	ΔE (cm^{-1})	M_{NMS} (GHz u)	M_{SMS} (GHz u)	M (GHz u)	F_s (GHz/fm^2)
0	26,215	-3567	3720	153	-123.6
1	28,311	-3242	3300	58	-117.8
2	28,694	-1094	2242	1148	-112.7
3	29,605	-1897	2765	868	-118.9
4	29,764	-1264	2379	1114	-111.2
5	29,787	-1612	2653	1041	-115.8
6	29,776	-1380	2424	1044	-113.2

the normal and specific mass shift (M_{NMS}, M_{SMS}) as well as the sum of both, denoted by (M) are separately tabulated. When the basis set is extended, large discrepancies for both M_{NMS} and M_{SMS} arise. This leads to the total mass shift constant to oscillate for the first few layers and then to converge to a consistent value for the last three layers. Similarly, the field shift constant F_s shows significant oscillations, that damp down rather slowly with an extended configuration space. Due to computational restrictions it was not possible to obtain a fully converged value for F_s.

Calculation of the hyperfine constants from the magnetic field and electric field gradient of the $^1P_1$ level in neutral nobelium, core-polarization (CP) effects were targeted by including single excitations from core orbitals into the wave function expansion, in addition to the above mentioned double and triple excitations.

Relativistic Fock space coupled cluster

The Fock space coupled cluster (FSCC) calculations of the hyperfine structure constants B and the field shifts F_s of the lowest excited states of No and of its lighter homologue Yb were carried out in the framework of the relativistic Dirac-Coulomb Hamiltonian [149]. The finite size of the nucleus was taken into account by implementing a Gaussian charge distribution [150]. Current implementation of the relativistic FSCC method [20] is limited to single and double electron excitations, which in practice means that we are able to treat systems with up to two valence electrons or holes (or a single hole and a single electron).

Yb and No have [Xe]$4f^{14}6s^2$ and [Rn]$5f^{14}7s^2$ ground state configurations respectively; we thus start our calculations from the [Xe]$4f^{14}$ and [Rn]$5f^{14}$ closed shell reference states, corresponding to the double charged ions of these elements. After solving the relativistic Dirac-Fock equations and correlating the closed shell reference state, two electrons are added

one at a time to reach the neutral atoms. At each stage the coupled cluster equations are solved to obtain the correlated ground and excited state energies. The model space for Yb consisted of $5d5f6s - f7s - d8s - d9sp$, and for No of $5g6d6f7s - d8s - d9sp10s11s$. Due to the use of the large model spaces, the convergence of the coupled cluster iterations became problematic, and we thus employed the intermediate Hamiltonian (IH) scheme in order to facilitate convergence [151]. For both elements the relativistic Faegri basis set was used [152], consisting of $25s23p16d12f6g2h$ function for Yb and $27s25p18d13f6g3h2i$ for No. The number of correlated electrons was 38 in Yb and 42 in No. We calculated the B constants using the finite field approach, as described in [153, 154]. The field shifts were also obtained by the finite field approach, by performing a number of calculations with different nuclear radii and extracting the derivatives of the transition energies with respect to the radii. Table 7.2 contains the calculated transition energies and the B and F_s parameters for Yb and No. For Yb, the transition energies are in excellent agreement with the experiment, as is the energy of the recently measured $4f^{14}7s7p\ ^1\mathrm{P}_1$ level in No. The successful performance for the FSCC approach also extends to the hyperfine structure applications: the average error of the calculated b constants of Yb is about 8% and we expect similar accuracy for our predictions for No.

Configuration interaction (CI)

Different combinations of the configuration interaction (CI), many-body perturbation theory (MBPT) and coupled-cluster techniques [45, 44, 119] provide accurate and reliable results from group II and group XII atoms and similar ions. They work very well when mixing with states involving citations from the core can be neglected or treated perturbatively. However, this has to be carefully examined in the case of the $5f^{14}7s7p\ ^1\mathrm{P}_1$ state of nobelium. A similar state of ytterbium ($4f^{14}6s6p\ ^1\mathrm{P}_1$), the iso-electronic homologue nobelium, is strongly mixed with the $4f^{13}6s^25d\ ^1\mathrm{P}_1$ state [159]. This leads to very poor accuracy when Yb is treated as a two-valence-electrons system. To check whether this is also the case for nobelium we performed calculations with two different methods. First we use the combination of the CI technique and the single-double coupled cluster method (CI+All-order method [45, 44]) which gives very accurate results for two to four valence electrons systems. Second, we employed the recently developed method [122] which is based on the CI technique but treats high-energy states perturbatively (the CIPT method). CIPT is not as accurate as the CI+All-order method for simple systems, but it can deal with complicated systems. The results of the calculations of the energy levels and hyperfine structure of Yb, Hg, and No by both methods are presented in Table 3. Yb is a chemical homologue of No and Hg has more

Table 7.2: Calculated energy levels, hyperfine structure constants B, and F_s for different atomic levels in neutral Yb and No, compared to experimental values where available. The electric quadrupole moment Q_s is taken to be 2.8 eb for ^{173}Yb [155], and 1 eb for No isotopes. The experimental data for Yb are taken from references [156, 157, 158].

	Level	Transition energies (cm^{-1})		HFS constant B (GHz/eb)		F_s∼(GHz/fm^2)
		FSCC	Exp.	FSCC	Exp	FSCC
Yb	$4f^{14}6s6p\ ^3P_0$	17,089	17,288			-9.59
	$4f^{14}6s6p\ ^3P_1$	17,806	17,992	-0.838	-0.827	-9.66
	$4f^{14}6s6p\ ^3P_2$	19,541	19,710	1.347	1.312	-9.84
	$4f^{14}6s6p\ ^1P_1$	26,118	25,068	0.744	0.609	-8.67
	$4f^{14}6s5d\ ^3D_1$	25,132	24,489	0.303	0.335	-11.14
	$4f^{14}6s5d\ ^3D_2$	25,342	24,751	0.436	0.482	-11.08
	$4f^{14}6s5d\ ^3D_3$	25,784	25,271	0.771	0.909	-10.82
	$4f^{14}6s5d\ ^1D_2$	27,932	27,678	1.153	1.115	-12.87
No	$4f^{14}6s6p\ ^3P_0$	19,046				-105.5
	$4f^{14}6s6p\ ^3P_1$	20,636		-0.708		-107.8
	$4f^{14}6s6p\ ^3P_2$	25,667		0.878		-114.6
	$4f^{14}6s6p\ ^1P_1$	30,365	29,961	0.465		-98.79
	$4f^{14}6s5d\ ^3D_1$	28,568		0.246		-12.46
	$4f^{14}6s5d\ ^3D_2$	29,019		0.374		-12.38
	$4f^{14}6s5d\ ^3D_3$	30,203		0.546		-11.85
	$4f^{14}6s5d\ ^1D_2$	33,233		0.679		-13.55

similarity with No than Yb in terms of mixing with core-excited states. The comparison of the Yb, Hg and No energy level spacings illustrate that the mixing of the $5f^{14}7s7p\ ^1P_1$ and $5f^{13}7s^26d\ ^1P_1$ states of nobelium is small and can be neglected. With the CIPT method the energy interval between states $4f^{14}6s6p\ ^1P_1$ and $4f^{13}6^s25d\ ^1P_1$ in Yb is around 4,000 cm^{-1} in both, calculations and experiment. The energy interval between similar states in No is much larger, around 18,000 cm^{-1}, indicating a small mixing. This is supported by the CI calculations with full matrix diagonalization but limited basis.

The HFS structure constant a is calculated in different steps to evaluate the accuracy of theory values. Initially, two-particle CI is considered, which does not include any core corrections to the wave function. The next stage is CI+MBPT, which includes core correlations in second order, which are very large, over 50% for the $^1P_1$ states. The CI+All-order results include third and higher-order correlations of the valence electrons with the core as well as corrections to the HFS expectation values beyond the correlation corrections to wave functions, including random-phase-approximation (RPA), core Brueckner, structure radiation, and normalization. The result of the CI+All-order calculations for the singlet state of Yb is

Table 7.3: Energy levels and magnetic dipole HFS constant a for low lying odd states of Yb, Hg and No. Hyperfine structure constants for Yb and Hg are presented for the isotopes ^{171}Yb ($I = 1/2$, $\mu = 0.4937\ \ \mu_N$) and 201Hg ($I = 3/2$, $\mu = -0.5602\ \mu_N$). For nobelium we assume $\mu/I = 1$. The experiment values are taken from references [24, 160, 161].

	State		Energies (cm^{-1})			Hyperfine structure constant $A\sim$(GHz)			
			CI+All	CIPT	Expt.	CI	CI+All	CIPT	Expt.
Yb	$4f^{14}6s6p$	^{3}P$_1$	18,261	17,8305	17,992	2.59	4.13	4.29	3.95797(47)
	$4f^{14}6s6p$	^{1}P$_1$	25,816	25,597	25,068	-0.34	-0.75	-0.27	-0.214173(53)
	$4f^{13}6s^25d$	^{1}P$_1$	34,946	30,071	28,857			1.46	
Hg	$5d^{10}6s6p$	^{3}P$_1$	40,029	43,822	39,412	-3.92	-5.54	-6.09	-5.454569(3)
	$5d^{10}6s6p$	^{1}P$_1$	54,478	55,975	54,069	0.77	1.45	1.64	1.316
	$5d^96s^26p$	^{1}P$_1$		86,035	78,813			-0.03	
No	$5f^{14}7s7p$	^{3}P$_1$	21,042	21,454		11.97	17.69	20.66	
	$5f^{14}7s7p$	^{1}P$_1$	30,203	29,864	29,961	-3.69	-6.27	-7.38	
	$5f^{13}7s^27p$	^{1}P$_1$	55,763	47,781				1.76	

almost four times larger than the experimental value. On the other hand, the CIPT method gives a value which is very close to the experiment. This is due to the mixing of the singlet state with the $4f^{13}6s^25d$ ^{1}P$_1$ state which is not included in the CI+All-order calculations but included in the CIPT calculations. In contrast, the calculations of both methods for the singlet state in No and Hg give very close results. This is another indication of small mixing. For simple two-electron states (including the $5f^{14}7s7p$ ^{1}P$_1$ state in No) the CI+All-order calculations gives the most accurate results. In Hg, CI+all-order value agrees with experiment to 10%. Assuming additional uncertainty in the values for nobelium in comparison to Hg due to larger core-Brueckner correction, we estimate an accuracy of the a($7s7p$ ^{1}P$_1$) to be on the order of 15%. We note that the accuracy of the ^{3}P$_1$ hyperfine a-constant is much better, 1.5% in Hg. Correspondingly, we estimate the accuracy in the case of nobelium to about 5%, making the ^{3}P$_1$ level a good case for benchmark comparison. The calculation of the isotope shift has many similarities with the HFS calculations and, in particular, the shift is strongly affected by mixing. We calculated the IS for Hg using the CI+All-order method as a test of the method accuracy. As discussed above, Hg is a good testing case for No due to similar mixing of the core-excited states of the odd configurations with $J = 1$. Comparing the Hg isotope shift with experiment for eight low odd states, the difference between theory and experiment is smaller than 4% for most of the states. Two last studied states $5d^{10}6s7p$ ^{3}P$_2$ and $5d^{10}6s7p$ ^{1}P$_1$ are strongly mixed with the states of the$5d^96s^26p$ configuration and the accuracy for them is poor. In the case of the isotope shift, the main uncertainty originates from the correlation corrections to the wave functions, so the difference of the CI+All-order

and CI+MBPT results, 7%, gives an estimate of the uncertainty, as omitted higher-order corrections are expected to be smaller than the dominant corrections that are already included in the CI+All-order calculations.

In general, the most accurate results are given by CI+All-order due to the most complete inclusion of correlations. The CI+MBPT results help to understand the role of higher-order correlations and the CIPT calculations are useful to reveal (or dismiss) the role of mixing with states which contain excitations from the $5f$ subshell.

Bibliography

[1] H. Backe *et al.*, *Prospectives for laser spectroscopy, ion chemistry and mobility measurements of superheavy elements in buffer-gas traps.* Nucl. Phys. A **944**, 492 (2015).

[2] M. Block, *Direct mass measurements of the heaviest elements with Penning traps.* Nucl. Phys. A **944**, 471 (2015).

[3] D. Ackermann and Ch. Theisen, *Nuclear structure features of very heavy and superheavy nuclei-tracing quantum mechanics towards the 'island of stability'.* Phys. Scr. **92**, 083002 (2017).

[4] A. Türler and V. Pershina, *Advances in the Production and Chemistrz of the Heaviest Elements.* Chem. Rev. **113**, 1237 (2013).

[5] Yu. Ts. Oganessian *et al., Synthesis of the isotopes of elements 118 and 116 in the* ^{249}Cf *and* ^{245}Cm+^{48}Ca *fusion reactions.* Phys. Rev. C **74**, 044602 (2006)

[6] M. Asai *et al., Nuclear structure of elements with* $100 \leq Z \geq 109$ *from alpha spectroscopy.* Nucl. Phys. A **944**, 308 (2015).

[7] R.D. Herzberg and P.T. Greenlees, *In-beam and decay spectroscopy of transfermium nuclei.* Prog. Part. Nucl. Phys. **61**, 674 (2008).

[8] M. Block *et al., Direct mass measurements above uranium bridge the gap to the island of stability.* Nature **463**, 785 (2010).

[9] M. Dworschak *et al., Penning trap measurements on nobelium isotopes.* Phys. Rev. C **81**,064312 (2010).

[10] E. Minaya Ramirez *et al., Direct mapping of nuclear shell effects in the heaviest elements.* Science **337**, 1207 (2012).

[11] Y. Ito *et al., First Direct Mass Measurements of Nuclides around Z=100 with a Multireflection Time-of-Flight Mass Spectrograph*. Phys. Rev. Lett. **120**, 152501 (2018)

[12] A. Türler, E. Eichler and A. Yakushev, *Chemistry studies of elements with* $Z \geq 104$ *in gas phase.* **944**, 640 (2015).

[13] Y. Nagame, J.V. Kratz and M. Schädel, *Chemistry studies of elements with $Z \geq 104$ in liquid phase.* **944**, 614 (2015).

[14] J.V. Kratz *et al., Chemical Properties of Element 105 in Aqueous Solution: Halide Complex Formation and Anion Exchange into Triisoctyl Amine.* Radiochim. Acta **48**, 121 (1989).

[15] M. Schädel *et al., Chemical Properties of Element 106 (Seaborgium).* Nature *388*, 55 (1997).

[16] R. Eichler *et al., Chemical Characterization of Bohrium (Element 107).* Nature **407**, 63 (2000).

[17] Ch.E. Düllmann *et al., Chemical Investigation of Hassium (Element 108).* Nature **418**, 859 (2002).

[18] R. Eichler *et al., Attempts to chemically investigate element 112.* Radiochim. Acta **94**, 181 (2009).

[19] A. Yakushev and R. Eichler *Gas-phase chemistry of element 114, flerovium.* EPJ Web of Conferences **131**, 07003 (2016).

[20] E. Eliav, S. Fritzsche, and U. Kaldor, *Electronic structure theory of the superheavy elements*. Nucl. Phys. A **944**, 518 (2015).

[21] P. Schwerdtfeger, L. F. Pateka, A. Punnett and P. O. Bowman, *Relativistic and quantum electrodynamic effects in superheavy elements*. Nucl. Phys. A **944**, 551 (2015).

[22] M. Sewtz *et al. First Observation of Atomic Levels for Element Fermium (Z=100).* Phys. Rev. Lett. **90**, 163002 (2003).

[23] H. Backe, *et al., Laser Spectroscopic Investigation of the Element Fermium ($Z = 100$)* Hyperfine Interactions **162**, 3 (2005).

[24] M. Laatiaoui *et al.*, *Atom-at-a-time laser resonance ionization spectroscopy of nobelium.* Nature **538**, 495 (2016).

[25] F. Lautenschläger, Ph.D. thesis, *Laserspektroskopie an Nobelium ($Z = 102$) in einer Puffergaszelle.*, Technische Universität Darmstadt, (2016).

[26] W. Lauth *et al.*, *Resonance ionization spectroscopy in a buffer gas cell with radioactive decay detection, demonstrated using ^{208}Tl.* Phys. Rev. Lett. **68**, 1675 (1992).

[27] F. Lautenschläger *et al.*, *Developments for resonance ionization laser spectroscopy of the heaviest elements at SHIP*. Nucl. Instrum. Methods B **383**, 115 (2016).

[28] P. Chhetri *et al., Impact of buffer gas quenching on the* $^1S_0 \rightarrow {}^1P_1$ *ground-state atomic transition in nobelium*. Eur. Phys. J. D **71**, 195 (2017).

[29] S. Raeder *et al.*,*Probing Sizes and Shapes of Nobelium Isotopes by Laser Spectroscopy.* Phys. Rev. Lett **120**, 232503 (2018).

[30] P. Chhetri *et al., Precision Measurement of the First Ionization Potential of Nobelium.* Phys. Rev. Lett **120**, 263003 (2018).

[31] W. Demtröder, *Atoms, Molecules and Photons.* Springer Berlin, Heidelberg (2010).

[32] B. H. Bransden and C. J. Joachim, *Physics of Atoms and Molecules.* Pearson (2003).

[33] B. H. Bransden and C. J. Joachim, *Quantum Mechanics.* Pearson (2000).

[34] J.P. Connerade, *Highly Excited Atoms.* Cambridge University Press, Cambridge (1998).

[35] P. Indelicato, *Projection operators in multiconfiguration Dirac-Fock calculations: Application to the ground state of helium like ions*. Phys Rev. A **51**, 1132 (1995).

[36] P. Indelicato, J.P. Santos, S. Boucard and J.-P. Desclaux, *QED and relativistic corrections in superheavy elements*. Eur. Phys. J. D **45**, 155 (2007).

[37] E. Eliav, U. Kaldor, and Y. Ishikawa, *Transition energies of ytterbium, lutetium, and lawrencium by the relativistic coupled-cluster method.* Phys. Rev. A **52**, 291 (1995)

[38] E. Eliav *et al.*, *Ground State Electron Configuration of Element 111*. Phys. Rev. Lett. **73**, 24 (1994).

[39] A. Borschevsky *et al.*, *Predicted spectrum of atomic nobelium.* Phys. Rev. A **75**, 042514 (2007).

[40] A. Borschevsky, *Extension of the intermediate Hamiltonian Fock space coupled cluster method and applications to problems of heavy and superheavy elements.* Ph.D. thesis (2009).

[41] J. P. Malrieu, Ph. Durand and J. P. Daudey, *Intermediate Hamiltonians as a new class of effective Hamiltonians* J. Phys. A **18**, 809 (1985).

[42] V. A. Dzuba, V^{N-M} *approximation for atomic calculations.* Phys. Rev. A **71**, 032512 (2005).

[43] V.A. Dzuba, M. S. Safronova, and U. I. Safronova, *Atomic properties of superheavy elements No, Lr, and Rf.* Phys. Rev. A **90**, 012504 (2014).

[44] V. A. Dzuba, *Combination of the single-double-coupled-cluster and the configuration-interaction methods: Application to barium, lutetium, and their ions*. Phys. Rev. A **90**, 012517 (2014).

[45] M. S. Safronova, M. G. Kozlov, W. R. Johnson, and Dansha Jiang, *Development of a configuration-interaction plus all-order method for atomic calculations*. Phys. Rev. A **80**, 012516 (2009).

[46] W. R. Johnson and J. Sapirstein, *Computation of Second-Order Many-Body Corrections in Relativistic Atomic Systems* Phys. Rev. Lett. **57**, 1126 (1986).

[47] R. Loudon, *The Quantum Theory of Light.* Oxford University Press, Oxford, (2000).

[48] M. Orszag, *Quantum Optics.* Springer, Berlin Heidelberg (2008).

[49] T. F. Gallagher, *Rydberg atoms*. Cambridge University Press (1994).

[50] T. F. Gallagher, *Rydberg atoms*. Rep. Prog. Phys **51**, 143 (1988).

[51] J. Murray-Krezan, *The classical dynamics of Rydberg Stark atoms in momentum space*. Am. J. Phys. **76**, 1007 (2008).

[52] M. J. Seaton, *Quantum defect theory*. Rep. Prog. Phys. **46**, 167 (1983).

[53] G. W. F. Drake and R. A. Swainson, *Quantum defects and the 1/n dependence of Rydberg energies: Second-order polarization effects.* Phys. Rev. A **44**, 5448 (1991).

[54] C. J. Foot, *Atomic physics.* Oxford University Press (2005).

[55] I. I. Sobelman, *Atomic Spectra and Radiative Transitions.* Springer, Berlin Heidelberg New York, 1992.

[56] H.B.G. Casimir, *On the Interaction between Atomic Nuclei and Electrons.* Freeman, San Francisco, CA, (1963).

[57] B Cheal and K T Flanagan, *Progress in laser spectroscopy at radioactive ion beam facilities*. J. Phys. G: Nucl. Part. Phys. **37** 113101 (2010).

[58] P. Campbell, I.D. Moore and M.R. Pearson, *Laser spectroscopy for nuclear structure physics*. Prog. Part. Nucl. Phys. **86**, 127 (2016).

[59] W.H. King, *Isotope Shifts in Atomic Spectra*. Plenum, New York, NY, (1984).

[60] A. R. Bodmer, *Spectroscopic Isotope Shift and Nuclear Deformations*. Proc. Phys. Soc. A **66**, 1041 (1954).

[61] S.A. Blundell *et al.*, *A Re-Evaluation of Isotope Shift Constants.* Z. Phys. A **321**, 31 (1985).

[62] C. F. von Weizsäcker, *Zur Theorie der Kernmassen.* Zeitschrift für Physik **96**, 431 (1935).

[63] W. D. Myers and Karl-Heinz Schmidt, *An update on droplet-model charge distributions*. Nucl. Phys. A **410**, 61 (1983).

[64] K.L.G. Heyde, *The nuclear shell model*. Springer, Berlin (1994).

[65] K.S. Krane, *Introductory nuclear physics*. Wiley, New York (1988).

[66] J. Lilley, *Nuclear Physics.* Wiley, New York (2008).

[67] M.G. Mayer and J.H.D. Jensen, *Elementary theory of nuclear shell structure*. Wiley, New York (1955).

[68] B. R. Mottelson and S. G. Nilsson, *Classification of the Nucleonic States in Deformed Nuclei.* Phys. Rev. **99**, 1615 (1955).

[69] R. F. Casten, *Nuclear Structure form a Simple Prespective*. Oxford Science Publications (2000).

[70] R. B. Firestone, *Table of Isotopes 8th Ed*. Wiley (1996).

[71] H. Backe *et al.*, *First observation of a resonance ionization signal on ^{242m}Am fission isomers*. Hyperfine Interactions **74**, 47 (1992).

[72] H. Backe *et al.*, *Isotope Shift Measurements for Superdeformed Fission Isomeric States*. Phys. Rev. Lett. **80**, 920 (1998).

[73] M. Laatiaoui *et al.*, *Perspectives for laser spectroscopy of the element nobelium*. Hyperfine Interact. **227**, 69 (2014).

[74] G. Münzenberg *et al.*, *The velocity filter SHIP, a separator of unslowed heavy ion fusion products.* Nucl. Instrum. Methods **161**, 65 (1979).

[75] G. Münzenberg, *From bohrium to copernicium and beyond SHE research at SHIP.* Nucl. Phys. A **944**, 5 (2015).

[76] S. Hofmann and G. Münzenberg, *The discovery of the heaviest elements.* Rev. Mod. Phys. **72**, 733 (2000).

[77] Yu. Ts. Oganessian *et al.*, *Measurements of cross sections for the fusion-evaporation reactions* $^{204,206,207,208}Pb$ + ^{48}Ca *and* ^{207}Pb + ^{34}S*: decay properties of the even-even nuclides* ^{238}Cf *and* ^{250}No*.* Phys. Rev. C **64**, 054606 (2001).

[78] M. Laatiaoui, *On the way to unveiling the atomic structure of superheavy elements*. EPJ Web of Conferences **131**, 05002 (2016).

[79] Elektro-Automatik GmbH & Co.KG http://shop.elektroautomatik.de/shop/shop__Laboratory%20Power%20Supply%200..32V0..10A__1::4::14::56::a09200411__en_GB;jsessionid=A3712E069A4B46A587F40D2F6A478D9B.

[80] P. Chhetri *et al., Investigation of the first ionization potential of ytterbium in argon buffer gas*. Acta Physica Polonica B (2018).

[81] National Instruments, http://sine.ni.com/nips/cds/view/p/lang/de/nid/202009.

[82] National Instrument LabVIEW, http://www.ni.com/de-de/shop/labview.html.

[83] Canberra Industries Inc, http://www.canberra.com/products/radiochemistrylab/pdf/Model-2004-SS.pdf.

[84] Ortec GmbH, http://web.mit.edu/8.13/8.13d/manuals/egg-par-ortec/ortec-471-spectroscopy-amplifier.pdf.

[85] Pfeiffer Vacuum GmbH, https://www.pfeiffer-vacuum.com/en/products/measurement/activeline/controllers/?detailPdoId=3526.

[86] Pfeiffer Vacuum GmbH, https://www.pfeiffer-vacuum.com/en/products/valves/gas-regulating-valves/?detailPdoId=4363.

[87] FuG-Electronik GmbH, http://www.fug-elektronik.de/de/produkte/kassetten/hce.html#techdata.

[88] National Instrument DAQ, http://sine.ni.com/nips/cds/view/p/lang/de/nid/11442.

[89] Y. Liu, R. Hutton and Y. Zou, *Atomic structure of the super-heavy element No I (Z = 102)*. Phys. Rev. A **76**, 062503 (2007).

[90] A. Kramida *et al.*, NIST Atomic Spectra Database (ver. 5.3), [Online]. Available: http://physics.nist.gov/asd [05 September 2017], National Institute of Standards and Technology, Gaithersburg, MD (2015).

[91] W. Meggers and J. Tech, *The First Spectrum of Ytterbium (Yb I).* J. Res. Nat. Bureau Stand. **83**, 13 (1978).

[92] K. B. Blagoev *et al.*, *Lifetimes of Levels of Neutral and Singly Ionized Lanthanide Atoms.* At. Data Nucl. Data Tables **56**, 33 (1994).

[93] C. J. Bowers *et al.*, *Experimental investigation of excited-state lifetimes in atomic ytterbium.* Phys. Rev. A **5**, 533103 (1996).

[94] S. G. Porsev *et al.*, *Electric-dipole amplitudes, lifetimes, and polarizabilities of the low-lying levels of atomic ytterbium.* Phys. Rev. A **4**, 602781 (1999).

[95] J. Brust and A. C. Gallagher, *Excitation transfer in barium by collisions with noble gases.* Phys. Rev. A **52**, 2120 (1995).

[96] W. H. Pence and S. R. Leone, *Laser studies of electronic excitation transfer in atomic calcium: Ca(*$4s5p\ ^1P_1$*)+Ar* $\rightleftarrows$ *Ca(*$4s5p\ ^3P_{2,1,0}$*)+Ar.* J. Chem. Phys. **74**, 5707 (1981).

[97] L. Krause, *Collisional transfer between fine-structure levels (Progress Report).* Phys. El. Atomic Coll.l., VlII ICPEAC (Amsterdam: North Holland), 65 (1972).

[98] P. Camus, A. Debarre and C. Morillon, *Highly excited levels of neutral ytterbium I. Two-photon and two-step spectroscopy of even spectra.* Phys. B: Atom. Molec. Phys. **13**, 1073 (1980).

[99] V. S. Letokhov, *Laser Photoionization Spectroscopy.* Academic Press, (1987).

[100] F. James, MINUIT–Function Minimization and Error Analysis, Reference Manual Version 94.1, CERN Program Library Long Writeup D506

[101] A. Corney, *Atomic and Laser Spectroscopy.*, Clarendon Press, Oxford, (1977).

[102] M. Sewtz, Ph.D. thesis, *Optische Spektroskopie an Fermium (*$Z = 100$*).*, Johannes Gutenberg-Universität, Mainz, (2003).

[103] G. T. Seaborg, T*he Transuranium Elements.* Science **104**, 379 (1946).

[104] T. K. Sato *et al.*, *Measurement of the first ionization potential of lawrencium, element 103.* Nature **520**, 209 (2015).

[105] S. Johnson *et al.*, *Resonance ionization mass spectrometry of thorium: determination of the autoionization level structure and a re-determination of the ionization potential.* Spectrochim. Acta, Part B **47**, 633 (1992).

[106] E. Worden *et al.*, I*onization potential of neutral atomic plutonium determined by laser spectroscopy.* Opt. Soc. Am. B **10**, 1998 (1993).

[107] E. Worden and J. Conway *Laser spectroscopy of neptunium; first ionization potential, lifetimes and new high-lying energy levels of Np i.* J. Opt. Soc. Am. **69**, 733 (1979).

[108] A. Coste *et al. New spectroscopic data on high-lying excited levels of atomic uranium.* J. Opt. Soc. Am. **72**, 103 (1982).

[109] N. Erdmann *et al. Determination of the first ionization potential of nine actinide elements by resonance ionization mass spectroscopy (RIMS).* J. Alloys Compd. **271**, 837 (1998).

[110] J. Roßnagel *et al. Determination of the first ionization potential of actinium.* Phys. Rev. A **85**, 012525 (2012).

[111] S. Rothe *et al.*, *Measurement of the first ionization potential of astatine by laser ionisation spectroscopy.* Nature Commun. **4**, 1835 (2013).

[112] Radiant Dyes, http://www.radiant-dyes.com/index.php/products/laser-dyes.

[113] Sirah Lasertechnik GMBH, http://www.sirah.com/dyes-accessories/laser-dyes-355-nm/coumarin-120.

[114] V. A. Dzuba *et al.*, *Ionization potentials of superheavy elements No, Lr, and Rf and their ions.*, Phys.Rev. A **94**, 042503 (2016).

[115] J. Sugar, *Revised ionization energies of the neutral actinides.* J. Chem. Phys. **60**, 4103 (1974).

[116] M. J. Seaton, *Quantum defect theory.* Proc. Phys. Soc. (London) **88**, 801 (1966).

[117] M. Aymar, R. J. Champeau, C. Delsart and O. Robaux *Three-step laser spectroscopy and multichannel quantum defect analysis of odd-parity Rydberg states of neutral ytterbium.* J. Phys. B: Atom. Molec. Phys **17**, 3645 (1984).

[118] NNDC Chart of Nuclides, https://www.nndc.bnl.gov/chart/reCenter.jsp?z=102&n=151.

[119] V. A. Dzuba, V. V. Flambaum, and M. G. Kozlov, *Combination of the many-body perturbation theory with the configuration-interaction method*. Phys. Rev. A **54**, 3948 (1996).

[120] P. Jöhnsson, X. He, C. F. Fischer, and I. Grant, *The grasp2K relativistic atomic structure package*. Comput. Phys. Commun. **177**, 597 (2007).

[121] I. P. Grant, *Relativistic quantum theory of atoms and molecules: theory and computation*, Vol. 40 (Springer Science & Business Media, 2007).

[122] V. A. Dzuba, J. C. Berengut, C. Harabati, and V. V. Flambaum, *Combining configuration interaction with perturbation theory for atoms with a large number of valence electrons*. Phys. Rev. A **95**, 012503 (2017).

[123] R.-D. Herzberg, *et al., Structure of rotational bands in* ^{253}*No*. Eur. Phys. J. A **42**, 333 (2009).

[124] P. Reiter, *et al., Structure of the Odd-A, Shell-Stabilized Nucleus* $^{253}_{102}$*No*. Phys. Rev. Lett. **95**, 032501 (2005).

[125] A. K. Mistry, *et al.,* In-beam study of ^{253}No using the SAGE spectrometer. Eur. Phys. J. A **53**, 24 (2017).

[126] M. Leino, *et al., In-beam study of* ^{254}*No.* Eur. Phys. J. A **6**, 63 (1999).

[127] R.-D. Herzberg, *et al., Nuclear isomers in superheavy elements as stepping stones towards the island of stability.* Nature **442**, 896 (2006).

[128] P. Reiter, *et al., Ground-State Band and Deformation of the Z=102 Isotope* ^{254}*No.* Phys. Rev. Lett. **82**, 509 (1999).

[129] I. Angeli and K. Marinova, *Table of experimental nuclear ground state charge radii: An update.* Atom. Data Nucl. Data Tab. **99**, 69 (2013).

[130] D. Berdichevsky and F. Tondeur, *Nuclear Core Densities, Isotope Shifts, and the Parametrization of the Droplet Model.* Z. Phys. A-Atoms and Nuclei **322**, 141 (1985).

[131] P. Möller, J. Nix, W. Myers and W. Swiatecki, *Nuclear Ground-State Masses and Deformations.* Atomic data and nuclear data tables **59**, 185 (1995).

[132] P.-H. Heenen, J. Skalski, A. Staszczak and D. Vretenar, *Shapes and $\alpha-$ and $\beta-$decays of superheavy nuclei.* Nucl. Phys. A **944**, 415 (2015).

[133] R.-D. Herzberg, *et al., Spectroscopy of transfermium nuclei:* $^{252}_{102}No$ Phys. Rev. C **65**, 014303 (2001).

[134] J. A. Maruhn, P.-G. Reinhard, P. D. Stevenson, and A. S. Umar, *The TDHF code Sky3D*. Comput. Phys. Commun. **185**, 2195 (2014).

[135] B. Schuetrumpf, W. Nazarewicz and P.-G. Reinhard, *Central depression nucleonic densities: Trend analysis in the nuclear density functional theory approach.* Phys. Rev. C **96**, 024306 (2017).

[136] P. Möller, J. Nix, W. D. Myers and W. Swiatecki, *The coulomb redistribution energy as revealed by a refined study of nuclear masses.* Nucl. Phys. A **536**, 61 (1992).

[137] J.-M. Yao, S. Baroni, M. Bender and P.-H. Heenen, *Beyond-mean-field study of the possible "bubble" structure of* ^{34}Si. Phys. Rev. C **86**, 014310 (2012).

[138] T. Duguet, V. Somà, S. Lecluse, C. Barbieri and P. Navrátil, *Ab initio calculation of the potential bubble nucleus* ^{34}Si. Phys. Rev. C **95**, 034319 (2017).

[139] P. Klüpfel, P.-G. Reinhard, T. J. BÃ¼rvenich, and J. A. Maruhn, *Variations on a theme by Skyrme: A systematic study of adjustments of model parameters*. Phys. Rev. C **79**, 034310 (2009).

[140] E.Chabanat, P.Bonche, P.Haensel, J.Meyer and R.Schaeffer, *A Skyrme parametrization from subnuclear to neutron star densities Part II. Nuclei far from stabilities*. Nucl. Phys. A **635**, 231 (1998).

[141] M. Kortelainen, J. McDonnell, W. Nazarewicz, P.-G. Reinhard, J. Sarich, N. Schunck, M. V. Stoitsov, and S. M. Wild, *Nuclear energy density optimization: Large deformations*. Phys. Rev. C **85**, 024304 (2012).

[142] P.-G. Reinhard and W. Nazarewicz, *Toward a global description of nuclear charge radii: Exploring the Fayans energy density functional.* Phys. Rev. C **95**, 064328 (2017).

[143] B. Schuetrumpf, *private communication.* (2017)

[144] A. Voss, V. Sonnenschein, P. Campbell, B. Cheal, T. Kron, I. D. Moore, I. Pohjalainen, S. Raeder, N. Trautmann, and K. Wendt, *High-resolution laser spectroscopy of long-lived plutonium isotopes*. Phys. Rev. A **95**, 032506 (2017).

[145] S. Fritzsche, C. F. Fischer, G. Gaigalas, *RELCI: A program for relativistic configuration interaction calculations.* Comput. Phys. Commun. **148**, 103 (2002).

[146] B. Cheal, T. E. Cocolios and S. Fritzsche, *Laser spectroscopy of radioactive isotopes: Role and limitations of accurate isotope-shift calculations.* Phys. Rev. A **86**, 042501 (2012).

[147] L. Filippin, *et al., Multiconfiguration calculations of electronic isotope shift factors in Al I.* Phys. Rev. A **94**, 062508 (2016).

[148] C. Nazè, E. Gaidamauskas, G. Gaigalas, M. Godefroid and P. Jönsson, *RIS3: A program for relativistic isotope shift calculations*. Comput. Phys. Commun. **184**, 2187 (2013).

[149] J. Sucher, *Foundations of the relativistic theory of many-electron atoms.* Phys. Rev. A **22**, 348 (1980).

[150] L. Visscher and K. Dyall, *Dirac-Fock atomic electronic structure calculations using different nuclear charge distributions.* Atomic Data and Nuclear Data Tables **67**, 207 (1997).

[151] A. Landau, E. Eliav, U. Kaldor, *Intermediate Hamiltonian Fock-space coupled-cluster method*. Advances in Quantum Chemistry **39**, 171 (2001).

[152] K. Faegri Jr, *Relativistic Gaussian basis sets for the elements K-Uuo.* Theoretical Chemistry Accounts **105**, 252 (2001).

[153] H. Yakobi, E. Eliav and U. Kaldor, *Nuclear quadrupole moment of 197Au from high-accuracy atomic calculations.* J. Chem. Phys. **126**, 184305 (2007).

[154] H. Yakobi, E. Eliav, L. Visscher and U. Kaldor, *High-accuracy calculation of nuclear quadrupole moments of atomic halogens.* J. Chem. Phys. **126**, 054301 (2007).

[155] N. Stone, J. Stone, P. Walker and C. Bingham, *Quasi-particle and collective magnetism: Rotation, pairing and blocking in high-K isomers.* Phys. Lett. B **726**, 675 (2013).

[156] D. Das and V. Natarajan, *Laser cooling of ^{173}Yb for isotope separation and precision hyperfine spectroscopy*.Phys. Rev. A **76**, 062505 (2007).

[157] S. G. Porsev, Yu. G. Rakhlina and M. G. Kozlov, *Calculation of hyperfine structure constants for ytterbium.* J. Phys. B **32**, 1113 (1999).

[158] W.-G. Jin, T. Horiguchi, M. Wakasugi, T. Hasegawa and W. Yang, *Systematic Study of Isotope Shiftsand Hyperfine Structures in Yb I by Atomic-Beam Laser Spectroscopy.* J. Phys. Soc. Jpn **60**, 2896 (1991).

[159] V. A. Dzuba, A. Derevianko, *Dynamic polarizabilities and related properties of clock states of the ytterbium atom.* J. Phys. B **43**, 074011 (2010).

[160] Handbook of Basic Atomic Spectroscopic Data, http://physics.nist.gov/PhysRefData/Handbook/index.html.

[161] N. J. Stone, *Table of nuclear magnetic dipole and electric quadrupole moments.* Atomic Data and Nuclear Data Tables **90**, 75 (2005).

[162] M. Laatiaoui *at al., Laser spectroscopy of nobelium and lawrencium.* GSI beamtime proposal (2017).

[163] F.P. Heßberger *et al.*, *Alpha-gamma decay studies of* ^{255}*Rf,* ^{251}*No and* ^{247}*Fm.* Eur. Phys. J. A **30**, 561 (2006).

[164] F.P. Heßberger *et al.*, *Alpha-gamma decay studies of* ^{255}*No.* Eur. Phys. J. A **29**, 165 (2006).

[165] F. P. Heßberger, *GSI experiments on synthesis and nuclear structure investigations of the heaviest nuclei.* Eur. Phys. J. D **45**, 33 (2007).

[166] A. Borschevsky *et al.*, *Transition energies of atomic lawrencium.* Eur. Phys. J. D **45**, 115 (2007).

List of publications

The results detailed in this thesis have been published in the following papers:

- M. Laatiaoui, H. Backe, M. Block, P. Chhetri, F. Lautenschläger, W. Lauth and Th. Walther
  Perspectives for laser spectroscopy of the element nobelium, Hyperfine Interact **227**, 69-75 (2014).

- F. Lautenschläger, P. Chhetri, D. Ackermann, H. Backe, M. Block, B. Cheal, A. Clark, C. Droese, R. Ferrer, F. Giacoppo, S. Götz, F.P. Heßberger, O. Kaleja, J. Khuyagbaatar, P. Kunz, A. K. Mistry, M. Laatiaoui, W. Lauth, S. Raeder, Th. Walther and C. Wraith
  Developments for resonance ionization laser spectroscopy of the heaviest elements at SHIP, Nucl. Instrum. Methods B **383**, 115-122 (2016).

- M. Laatiaoui, W. Lauth, H. Backe, M. Block, D. Ackermann, B. Cheal, P. Chhetri, C. E. Düllmann, P. Van Duppen, J. Even, R. Ferrer, F. Giacoppo, S. Götz, F. P. Heßberger, M. Huyse, O. Kaleja, J. Khuyagbaatar, P. Kunz, F. Lautenschläger, A. K. Mistry, S. Raeder, E. Minaya Ramirez, Th. Walther, C. Wraith and A. Yakushev
  Atom-at-a-time laser resonance ionization spectroscopy of nobelium, Nature **538**, 495-498 (2016).

- P. Chhetri, D. Ackermann, H. Backe, M. Block, B. Cheal, C. E. Düllmann, J. Even, R. Ferrer, F. Giacoppo, S. Götz, F. P. Heßberger, O. Kaleja, J. Khuyagbaatar, P. Kunz, M. Laatiaoui, F. Lautenschlöger, W. Lauth, E. Minaya Ramirez, A. K. Mistry, S. Raeder, C. Wraith, Th. Walther and A. Yakushev
  Impact of buffer gas quenching on the $^1S_0 \rightarrow {}^1P_1$ *ground-state atomic transition in nobelium*, Eur. Phys. J. D **71**, 195 (2017).

- P. Chhetri, C. S. Moodley, S. Raeder, M. Block, F. Giacoppo, S. Götz, F. P. Heßberger, M. Eibach, O. Kaleja, M. Laatiaoui, A. K. Mistry, T. Murböck and Th. Walther
  Investigation of the first ionization potential of ytterbium in argon buffer gas, Acta Phys. Polon. B **49**, 599 (2018).

- S. Raeder, D. Ackermann, H. Backe, R. Beerwerth, J. C. Berengut, M. Block, A. Borschevsky, B. Cheal, P. Chhetri, Ch. E. Düllmann, V. A. Dzuba, E. Eliav, J.

Even, R. Ferrer, V. V. Flambaum, S. Fritzsche, F. Giacoppo, S. Götz, F. P. Heßberger, M. Huyse, U. Kaldor, O. Kaleja, J. Khuyagbaatar, P. Kunz, M. Laatiaoui, F. Lautenschläger, W. Lauth, A. K. Mistry, E. Minaya Ramirez, W. Nazarewicz, S. G. Porsev, M. S. Safronova, U. I. Safronova, B. Schuetrumpf, P. Van Duppen, T. Walther, C. Wraith, and A. Yakushev.
Probing Sizes and Shapes of Nobelium Isotopes by Laser Spectroscopy, Phys. Rev. Lett. **120**, 232503 (2018).

- P. Chhetri, D. Ackermann, H. Backe, M. Block, B. Cheal, C. Droese, Ch. E. Düllmann, J. Even, R. Ferrer, F. Giacoppo, S. Götz, F.P. Heßberger, M. Huyse, O. Kaleja, J. Khuyagbaatar, P. Kunz, M. Laatiaoui, F. Lautenschläger, W. Lauth, N. Lecesne, L. Lens, E. Minaya Ramirez, A. K. Mistry, S. Raeder, P. Van Duppen, Th. Walther, A. Yakushev, and Z. Zhang
Precision Measurement of the First Ionization Potential of Nobelium. Phys. Rev. Lett. **120**, 263003 (2018).

The Author also participated on several other experiments during his Ph.D., leading to the publications listed below:

- F. Giacoppo, *et al., Recent upgrades of the SHIPTRAP setup: On the finish line towards direct mass spectroscopy of superheavy elements*. Acta Physica Polonica B **48** (3), 423 (2017).

- D. Ackermann, *et al., COMPASS−a COMPAct decay Spectroscopy Set*. Nucl. Instrum. Methods Phys. Res. B (2018), https://doi.org/10.1016/j.nima.2018.01.096.

Curriculum Vitae

Personal data Premaditya Chhetri

born 17 March 1989,
Kalimpong

Graduation

04/2013–present Ph.D. student in the group Prof. Dr. Thomas Walther, Institut für Angewandte Physik, Technische Universität Darmstadt
Thesis title: *Laser spectroscopy of nobelium isotopes*

University education

05/2007–03/2012 Studies of physics, Sri Satya Sai Institute of Higher Learning, Prasanthi Nilayam, India

06/2011–03/2012 Graduation in the Physics group, Sri Satya Sai Institute of Higher Learning, Prasanthi Nilayam, India
Thesis title: *Electron and gamma studies in* ^{122}*Te from the beta decay of* ^{122}*Sb*

03/2012 Master

School education

05/2005 School at St. Augustine's School, Kalimpong, India

05/2007 High school at The Scottish Universities' Mission Institution

Erklärung zur Dissertation

Hiermit versichere ich, die vorliegende Dissertation ohne Hilfe Dritter nur mit den angegebenen Quellen und Hilfsmitteln angefertigt zu haben. Alle Stellen, die aus Quellen entnommen wurden, sind als solche kenntlich gemacht. Diese Arbeit hat in gleicher oder ähnlicher Form noch keiner Prüfungsbehörde vorgelegen.

Darmstadt, den

(Premaditya Chhetri)